2019

Retrospective and real-time semiconductor dosimetry: applications to geological dating and brachytherapy quality assurance

Anna A. Romanyukha
University of Wollongong

RETROSPECTIVE AND REAL-TIME SEMICONDUCTOR DOSIMETRY: APPLICATIONS TO GEOLOGICAL DATING AND BRACHYTHERAPY QUALITY ASSURANCE

A dissertation submitted in fulfilment of

the requirements for the award of the degree of

Doctor of Philosophy

from

UNIVERSITY OF WOLLONGONG

by

Anna A. Romanyukha

M.Sc. Health Physics

School of Physics

Faculty of Engineering

2019

Dedicated to

Papa.

Table of Contents

List of Tables

List of Figures

List of Abbreviations

2D	Two-dimensional
AAPM	American Association of Physicists in Medicine
AFE	Analog Front End
BT	Brachytherapy
CMRP	Centre for Medical Radiation Physics (UOW)
CT	Computed Tomography
DRP	Dosimetric Rectal Probe
DVH	Dose Value Histogram
EBRT	External Beam Radiation Therapy
epi	epitaxial
EPID	Electronic Portal Imaging Device
ESTRO	European Society for Radiotherapy and Oncology
FPGA	Field Programmable Gate Array
GaN	Gallium Nitride
GM	Geiger-Mueller
GTV	Gross Tumor Volume

IAEA International Atomic Energy Agency

ICP-MS Inductively Coupled Plasma Mass Spectrometry

ICRP International Commission on Radiological Protection

INT Istituto Nazionale dei Tumori

IRSL Infrared Stimulated Luminescence

IVD *In Vivo* Dosimetry

HDR High Dose Rate

HR-CTV High-risk Clinical Target Volume

ka one thousand years

LA-ICP-MS Laser Ablation Inductively-Coupled Plasma Mass Spectrometry

LDR Low Dose Rate

LET Linear Energy Transfer

LINAC Linear Accelerator

MAFalda Medipix Analysis Framework

MC Monte Carlo

MCNP Monte Carlo N-Particle

MOSFET Metal Oxide Semiconductor Field Effect Transistor

MR Magnetic Resonance

MVC Multichannel Vaginal Cylinder

OAR Organ at Risk

OES Optical Emission Spectroscopy

OSL Optically Stimulated Luminescence

ppm Parts Per Million

PSD	Plastic Scintillation Detector
PTV	Planned Target Volume
QA	Quality Assurance
QC	Quality Control
RT	Radiotherapy
SAR	Single-aliquot Regenerative-dose
SDD	Source-to-detector Distance
SNR	Signal-to-noise Ratio
TCC	Treatment Communication Console
TL	Thermoluminescence
TLD	Thermoluminescence Dosimetry
TOT	Time-over-threshold
TPS	Treatment Planning System
TRUS	Transrectal Ultrasound
TT	Thermally-transferred
VSL	Violet Stimulated Luminescence
WHO	World Health Organization

Acknowledgements

I am grateful for the exceptional supervision I received from Anatoly Rosenfeld and Bert Roberts at UOW, and Mauro Carrara at INT. I thank them for sharing their passion for radiation dosimetry with me, and for their patience and time. I am privileged to have learned from such accomplished researchers in the early stages of my career. Anatoly and Mauro, I immensely appreciate the knowledge and tolerance that you have invested in me. It has been a pleasure to spend the past years of my life in your company.

I thank Stuart George for introducing me to the Timepix detector, and setting the "ancient" dosimetry project off on the right foot. I thank Chiara Tenconi and Dean Cutajar for teaching me to assemble and operate MO*Skin* dosimeters, and remain grateful for their continuous advice and encouragement. I thank Iolanda Fuduli for her support with the diode detectors, and Jose Abrantes, Terry Lachlan and Yasaman Jafari for their support with the geology sample production. Thank you to all the wonderful people of the Fisica Medica Unit at INT for the kind reception.

I am grateful to Diane van den Broek and Mariana Sontag Gonzalez for proofreading the first chapter of this thesis, and of course for their friendship.

Thank you to my partner Rafael Tucci for his infinite support in everything that I do. I am forever grateful to Papa for introducing me to the world of radiation, and for all he has invested in me, as well as to Mama and Marina for their care, love, and support.

I thank the Australian Research Council for scholarship support through Laureate Fellowship grant FL130100116. This work was partially supported by the Italian Ministry of Health (5 x 1000 Funds – year 2014).

List of Publications

Romanyukha A, Cunningham A, George S, Guatelli S, Petasecca M, Rosenfeld A, Roberts R, 2017. Deriving spatially resolved beta dose rates in sediment using the Timepix pixelated detector. Rad. Meas. 1-8.

Romanyukha A, Carrara M, Tenconi C, Mazzeo D, Rossi G, Borroni M, Pignoli E, Cerrotta A, Cutajar D, Petasecca M, Lerch M, Bucci J, Rosenfeld AB, 2017. Applications of MO*Skin* dosimeters for quality assurance in gynecological HDR brachytherapy: An in-phantom feasibility study. Rad. Meas. 1-6.

Giandini T, Panaino C, Avuzzi B, Morlino S,Villa S, Bedini N, Carabelli G, Frasca S, **Romanyukha A**, Rosenfeld A, Pignoli E, Carrara M, 2017. An accurate method to quantify breathing-induced prostate motion for patients implanted with electromagnetic transponders. Tumori. 103-2,136-142.

Carrara M, Tenconi C, Mazzeo D, **Romanyukha A**, Borroni M, Pignoli E, Cutajar D, Petasecca M, Lerch M, Bucci J, Gambarini G, Cerrotta A, Fallai C, Rosenfeld AB, 2017. Study of the correlation between rectal wall in vivo dosimetry performed with MO*Skins* and implant modification during TRUS-guided HDR prostate brachytherapy. Rad. Meas. 106, 385-390.

Carrara M, **Romanyukha A**, Tenconi C, Mazzeo D, Cerrotta A, Borroni M, Cutajar D, Petasecca M, Lerch M, Bucci J, Richetti A, Presilla S, Fallai C, Gambarini G, Pignoli E, Rosenfeld AB, 2017. Clinical application of MO*Skin* dosimeters to rectal wall in vivo dosimetry in gynecological HDR brachytherapy. Phys. Med. 41, 5-12.

Carrara M, Cutajar D, Alnaghy S, Espinoza A, **Romanyukha A**, Presilla S, Tenconi C, Cerrotta A, Fallai C, Safavi-Naeini M, Petasecca M, Kejda A, Lerch M, Corde S, Jackson M, Howie A, Bucci J, Rosenfeld AB, 2018. Semiconductor real-time quality assurance dosimetry in brachytherapy. Brachytherapy. 17:133–145.

Romanyukha A, Carrara M, Cutajar D, Petasecca M, Fuduli I, Al-Salmani T, Lerch M, Perevertaylo V, Mazzeo D, Cerrotta A, Fallai C, Pignoli E, Rosenfeld AB, 2019. Preliminary epi-diode characterization for HDR brachytherapy quality assurance. J. Phys. Conf. Ser. 1154, 012026.

Romanyukha A, Carrara M, Mazzeo D, Tenconi C, Al-Salmani T, Poder J, Cutajar D, Fuduli I, Petasecca M, Bucci J, Cerrotta A, Pappalardi B, Pignoli E, Rosenfeld AB, 2019. An innovative gynecological HDR brachytherapy applicator system for treatment delivery and real-time verification. Phys. Med. 59, 151-157.

Other Publications

Romanyukha A, Folio L, Lamart S, Simon S, Lee C, 2016. Body-size specific effective dose conversion coefficients for CT scans. Radiat. Prot. Dosim. 172-4,428-437.

Dabin J, Mencarelli A, McMillan D, **Romanyukha A**, Struelens L, Lee C, 2016. Validation of calculation algorithms for organ doses in CT by measurements on a 5 year old paediatric phantom. Phys. Med. Biol. 61-11,4168-82.

Publication titled "Defining a simplified method of MO*Skin* calibration for *in vivo* dosimetry in a clinical setting" on the content of chapter 8 (section 8.4) will be submitted in the upcoming months.

List of Conference Presentations

Romanyukha A, Cunningham A, George S, Guatelli S, Petasecca M, Rosenfeld A, Roberts R. Measuring beta-source heterogeneity in sediment using the Medipix2 pixelated semiconductor detector. 4th Asia Pacific Luminescence and Electron Spin Resonance Dating Conference. Adelaide, Australia. November 2015.

Romanyukha A, Carrara M, Mazzeo D, Tenconi C, Borroni M, Cerrotta A, Pignoli E, Cutajar D, Petasecca M, Bucci J, Rosenfeld A. In-phantom and *in-vivo* applications of MO*Skin*™ dosimeters for Quality Assurance in HDR Brachytherapy. Micro-Mini & Nano-Dosimetry Conference. Hobart, Australia. January 2016.

Romanyukha A, Carrara M, Mazzeo D, Tenconi C, Borroni M, Cerrotta A, Pignoli E, Cutajar D, Petasecca M, Bucci J, Rosenfeld A. In vivo dosimetry of the rectal wall in HDR brachytherapy procedures using MO*Skin* dosimeters and a new method of MO*Skin* recalibration. Australian Australasian Brachytherapy Group 25th ASM. Freemantle, Australia. March 2016.

Rossi G, Carrara M, Tenconi C, **Romanyukha A**, Borroni M, Gambarini G, Cutajar D, Petasecca M, Lerch M, Bucci J, Rosenfeld A, Pignoli E. Correction function for MO*Skin* readings in realtime in vivo dosimetry in HDR prostate brachytherapy. 35th Conference of the European Society for Therapeutic Radiology and Oncology (ESTRO 35). Turin, Italy. April 2016.

Romanyukha A, Carrara M, Rossi G, Tenconi C, Borroni M, Pignoli E, Cutajar D, Petasecca M, Lerch M, Bucci J, Gambarini G, Rosenfeld A. Post IVD verification and recalibration of MO*Skin*s using a certified low dose emitting Sr-90 source. 35th Conference of the European Society for Therapeutic Radiology and Oncology (ESTRO 35). Turin, Italy. April 2016.

Tenconi C, Carrara M, Mazzeo D, **Romanyukha A**, Cerrotta A, Rossi G, Borroni M, Cutajar D, Petasecca M, Lerch M, Bucci J, Fallai C, Gambarini G, Pignoli E, Rosenfeld A. In vivo rectal wall dosimetry in gynecological HDR brachytherapy using a semi-flexible rectal probe provided with MO*Skin* dosimeters. 2016 World Congress of Brachytherapy. San Francisco, USA. June 2016.

Romanyukha A, Carrara M, Tenconi C, Mazzeo D, Rossi G, Borroni M, Pignoli E, Cerrotta A, Cutajar D, Petasecca M, Lerch M, Bucci J, Rosenfeld A. Applications of MO*Skin* dosimeters for quality assurance in gynecological HDR brachytherapy: an in-phantom feasibility study. 18th International Conference on Solid State Dosimetry. Munich, Germany. June 2016.

Romanyukha A, Cunningham A, George S, Guatelli S, Petasecca M, Rosenfeld A, Roberts R. Visualization of radioactive hotspots in natural sediments using the Timepix detector. 18th International Conference on Solid State Dosimetry. Munich, Germany. June 2016.

Romanyukha A, Carrara M, Mazzeo D, Tenconi C, Borroni M, Cerrotta A, Pignoli E, Cutajar D, Petasecca M, Lerch M, Bucci J, Rosenfeld A. Quality assurance in gynecological HDR brachytherapy using MO*Skin* dosimeters: an in vivo study. MedPhys2016. Sydney, Australia. November 2016.

Romanyukha A, Carrara M, Mazzeo D, Tenconi C, Borroni M, Cerrotta A, Pignoli E, Petasecca M, Lerch M, Rosenfeld A. Quality assurance in gynecological high dose rate brachytherapy: an *in vivo* study. Bundeswehr Institute of Radiobiology. Munich, Germany. August 2017.

Romanyukha A, Fu X, Li B, George S, Morley M, Guatelli S, Rosenfeld A, Roberts, R. Spatially resolved sediment dose rates using the Timepix pixelated detector. German Luminescence and ESR Meeting. Bayreuth, Germany. October 2017.

Romanyukha A, Carrara M, Mazzeo D, Petasecca M, Al-Salmani T, Cutajar D, Cerrotta A, Fallai C, Pignoli E, Rosenfeld A. Gynecological HDR BT applicator for treatment delivery and online QA verification of source dwell positions and times. Micro-Mini & Nano-Dosimetry Conference. Mooloolaba, Australia. February 2018.

Romanyukha A, Carrara M, Mazzeo D, Petasecca M, Al-Salmani T, Cutajar D, Cerrotta A, Fallai C, Pignoli E, Rosenfeld A. An innovative gynecological HDR brachytherapy applicator system for treatment delivery and real-time verification. European Congress of Medical Physics. Copenhagen, Denmark. August 2018.

RETROSPECTIVE AND REAL-TIME SEMICONDUCTOR DOSIMETRY: APPLICATIONS TO GEOLOGICAL DATING AND BRACHYTHERAPY QUALITY ASSURANCE

Anna A. Romanyukha

A Thesis for Doctor of Philosophy in Physics

School of Physics
University of Wollongong

ABSTRACT

In this thesis solid state semiconductor dosimetry is applied to the improvement of luminescence dating techniques (part 1) and quality assurance in high dose rate (HDR) brachytherapy (BT) cancer treatments (part 2).

The aim of part 1 is the development, testing, and application of a novel method to measure spatially resolved dose rates in sediment samples using the Timepix pixelated detector. The Timepix contains an array of 256x256 pixels, each 55x55 μm in size and with its own preamplifier, discriminator and digital counter, and is able to provide the position and pixel-by-pixel count rate of the incident radiation. The development of a method to measure sediment samples and derive spatially resolved dose rates is described, followed by its application to sediment samples from Liang Bua and Denisova Cave archeological sites.

Part 2 focuses on the application of real time *in vivo* dosimetry for HDR BT treatment verification. MO*Skin* dosimeters were selected due to their small size and capability of measuring steep dose gradients, such as those characteristic of the HDR source. Three MO*Skin*s were placed on a rectal probe to verify doses to the rectal wall in gynecological BT treatments. A feasibility study and the *in vivo* application of the proposed method to patient treatments at the Istituto Nazionale dei Tumori (INT) are described. Furthermore, a system for real time tracking of the HDR source is proposed by embedding epitaxial diodes on the surface of a multichannel vaginal cylinder (MVC). The ability of the developed system to verify positions and dwell times of the HDR source was tested using simple dwell positions and dwell times, followed by the retrospective delivery of 10 clinical plans previously delivered to patients undergoing adjuvant vaginal cuff BT after hysterectomy at INT.

KEYWORDS: Solid state dosimetry, spatially resolved radioactivity, Timepix, sediment dating, *in vivo* dosimetry, HDR brachytherapy, MOSFET, gynecological brachytherapy, diodes, multichannel vaginal applicator.

Chapter 1

Introduction

Radiation has influenced many spheres of our lives. It is applied to chronological dating of objects and events, as well as for various medical applications that include the diagnosis and treatment of skeletal, vascular, and soft-tissue diseases. Its far-reaching potential can be exemplified by the distant places where nuclear energy is used: in our homes, on submarines and satellites.

Radioactivity is the product of the transition of an unstable nucleus to a stable, or more stable state. Radioactive elements are inherent to Earth's geological composition, where they are most abundant in the uranium, thorium, and potassium decay chains. Radioisotopes can also be produced artificially by neutron bombardment or through the interaction of charged particle accelerator beams with a target. Natural radioisotopes, such as ^{238}U, ^{232}Th and ^{40}K, are used for sediment dating; artificially produced radioisotopes, such as ^{192}Ir, ^{60}Co, ^{103}Pd, ^{125}I and ^{131}I are employed in radiotherapy cancer treatments. Thus, through the correct chronological placement of sediments, radiation can be the key to understanding the past, and, by advancing radiotherapy treatments, it can improve the quality of life of present and future populations.

Modern humans had evolved into their current anatomical structure by about 200,000 years (ka) ago in Africa. From there on we, *Homo sapiens* (Latin for "wise"), have advanced via natural selection while dispersing and adapting to habitats inherent to the various continents and regions. Ancient civilizations cultivated a culture and with it an awareness of history. However the wide belief that we were the only *Homo* species to have inhabited Earth persisted, until the discovery of the Neanderthals in the nineteenth century [1]. Further discoveries of species from the *Homo* genus have shed some light on a previously unknown world of the *Homo erectus*, *Homo heidelbergensis*, and *Homo habilis*, among others. These discoveries have only taken place in the last 120 years, with the most recent skeletons of *Homo naledi* found by cavers in South Africa in 2013 [2].

Denisovans and *Homo floresiensis* are among the most recent additions to the *Homo* genus, discovered in 2010 and 2003, respectively. Both species inhabited Earth alongside H. sapiens for hundreds of thousands of years and eventually became extinct. Denisovans were discovered in the Denisova Cave in the Altai region of Russia. The Indonesian "hobbit" species was found in the cave Liang Bua on the island of Flores. Both are thought to have existed at these sites in the period of 200 to 50 ka ago, lived, and possibly interbred, particularly in the case of the former, with modern-day humans [3]. Although bone fragments of the Denisovans were uncovered in Russia, it has been postulated that the species covered a wide geographical scope, with DNA-based evidence suggesting that these could potentially be the widest-spreading species after modern humans [4]. Both of these ancient hominins eventually became extinct, whereas we, the modern-day humans, continued to evolve into the society we comprise today.

Over thousands of years the "wise men" proved themselves to be fitter for life on Earth than the rest of the members of the *Homo* genus. Humans started dispersing out of the African niche 60 ka years ago, and at about 10 ka ago a shift in human life patterns occurred, taking us from a hunting-and-gathering society into a more settled way of life, with agriculture at its center. Our species continued to evolve,

eventually bringing about industrialization, and with it considerable changes to the structure of human life. Humans have progressed through a variety of lifestyles that appear to affect, among others, the patterns of population morbidity [5]. The major cause of death in human populations has evolved from injury/violence to infectious disease and chronic disease, respectively, and finally arrived at cancer — one of the most pervasive diseases currently known to humans. Annually cancer has led to the death of 8.8 million people [6], and has been dubbed the "Emperor of all Maladies" by one of the most prominent contemporary oncologist-writers, Siddhartha Mukherjee. 14.1 million new cancer cases were reported worldwide in 2012, and this number is expected to increase to 23.6 million by the year 2030 [7]. Approximately half of all cancer patients undergo radiotherapy treatments, sometimes as the sole treatment, or often combined with other treatment modalities, including surgery, chemotherapy, and immunotherapy. Brachytherapy is radiotherapy delivered directly into or in close proximity to the target, allowing increased doses to the target, while sparing the surrounding healthy tissues. The complexity of radiotherapy techniques is constantly rising, with sophisticated methods such as the introduction of additional accessories (i.e., multiple needles in brachytherapy) and devices (i.e., organ motion trackers) that allow better targeting, but also more room for errors to occur. The integration of radiation measurements into clinical routines is able to provide an independent mode of treatment verification, and thus ensure that the treatment has been delivered as intended by the hospital staff, making radiation measurements an integral part of optimal clinical outcomes.

Despite the fact that *H. sapiens* has overcome challenges insurmountable to our fellow hominins, effective cancer treatment remains a challenge. Cancer treatment procedures are still in need of development and improvement to achieve the highest quality of cancer care possible, and subsequently, increase the quality and longevity of life for the cancer patient. The advancement of radiation measurement techniques is imperative in order to gain a better understanding of the past and the future of our species. It is important that we apply the unique properties of

radiation in order to learn patterns of the dispersal of our predecessors on Earth, and why they came to be extinct, all the meanwhile continuing to tackle the obstacles of contemporary life. The "wise man" is one who lives consciously: aware of the past, and capable of shaping a future where our species continue to thrive on Earth.

1.1 Thesis aims

This thesis is unique because it combines two distinct areas of research through the application of solid-state semiconductor dosimetry: archeology and radiotherapy. These two interdisciplinary studies, in a sense, relate to both the ancient and the modern human race. The "ancient" dosimetry study aims to improve luminescence-based dating techniques to gain further insight into the past, while the "modern" aims to advance cancer treatment procedures for the benefit of future generations of oncology patients.

This dissertation is divided into two parts: the "ancient" i.e., retrospective dosimetry, and the "modern" i.e., real-time dosimetry. Chapters 2 and 10 stand outside the two parts, and serve as the introduction and conclusion to the respective topics. Chapter 2 outlines the basic concepts in solid-state semiconductor dosimetry and introduces the differences between its applications to luminescence dating and medical physics, respectively. Chapter 10 addresses the recommendations and conclusions of both the retrospective and real-time dosimetry research projects. The aims of this thesis are the:

1. Development, testing, and application of a novel method to measure spatially resolved dose rates in sediment samples using the Timepix pixelated detector.
2. Feasibility and application of rectal wall *in vivo* dosimetry (IVD) in gynecological brachytherapy treatment employing MO*Skin* dosimeters.

3. Development and verification of an innovative brachytherapy applicator for gynecological brachytherapy with an embedded real-time high dose rate source verification system using epitaxial diodes.

1.2 Thesis outline

Part 1 addresses the first aim, and includes chapters 3 through 6. Chapter 3 describes the main concepts in luminescence dating and how sediment age is derived, followed by a more detailed statement of the retrospective dosimetry study aims. Chapter 4 addresses the particular issue of inhomogeneity of radiation within sediment samples, and describes previous research and its existing limitations. The proposed solution — a novel method utilizing the Timepix detector, and the initial feasibility studies are described. Chapter 5 outlines the development of the proposed novel methodology: the measurement and data analysis procedure to extract spatially resolved dose rates in sediment samples using the Timepix detector. This chapter includes a description of the Geant4 simulation component, sample preparation and measurement setup, and the Timepix count rate to environmental dose rate calibration procedures. The application of the developed method to sediment samples, including an artificial stratified sample, and sediment samples from the Liang Bua and Denisova caves, is then addressed in chapter 6.

Part 2 includes chapters 7 through 9. Chapter 7 explains the rationale for real-time treatment verification and the specific dose calculation method applied in brachytherapy (i.e., the radiotherapy treatment of interest in this study). Gynecological high dose rate (HDR) brachytherapy treatments are introduced, and the requirements of an effective real-time treatment verification system are outlined. Two possible methods of real time *in vivo* dose verification are introduced: dosimetry via placement of miniature detectors in points of interest, and source tracking to match the planned dwell positions and times to the delivered treatment. Chapter 8 addresses the second thesis aim, and describes MO*Skin* dosimeters and

the proposed IVD system. Section 8.4 describes the proposed simplified method for MO*Skin* calibration adjustment for IVD dosimetry in the clinic, and sections 8.5 and 8.6 present the completed IVD patient study and conclusions, respectively. Chapter 9 addresses the third thesis aim, and is dedicated to the proposed real-time radiation tracking system employing innovative epi diodes. An overview of HDR brachytherapy source tracking as a method for treatment verification is addressed in section 9.1; section 9.2 presents a more detailed statement of the study aims. The radiation resistant epitaxial diodes and the novel multichannel vaginal cylinder (MVC) applicator system developed to address existing shortcomings in source tracking methods are described in sections 9.3 and 9.4. The application and verification studies of the MVC applicator system are discussed in section 9.5. Section 9.6 focuses on recommendations and conclusions of the MVC system's application for real-time brachytherapy treatment verification.

Chapter 10 concludes with a summary of the achievements of both the "ancient" and "modern" dosimetry projects, followed by recommendations of the potential future improvements to the proposed methodologies, and the final conclusions.

Chapter 2

Solid-state semiconductor dosimetry: the basics

Radiation can be measured using a number of techniques and materials that include gas-filled chambers, film, and scintillation and solid-state semiconductor materials. The latter is the focus of this thesis. Initial research on solid-state methods focused on thermoluminescence dosimetry (TLD), with Daniels et al. (1953) [8] applying solid-state dosimetry to both radiation protection and dating of geological material.

2.1 Solid-state semiconductors and band theory

Solids are classified according to the mobility of electrons in response to an electric field, which is further characterized by the crystal structure and band gap [9]. Solids are identified as conductors, semiconductors, or insulators. Crystalline solids have regular repeated atomic arrangements in a lattice, and are further subdivided into covalent solids, with adjacent atoms covalently bound by shared valence electrons. These are very hard and have high melting points, and since they do not have free

electrons they are poor conductors of electricity. Examples include copper (conductor), silicon (semiconductor), and diamond (insulator).

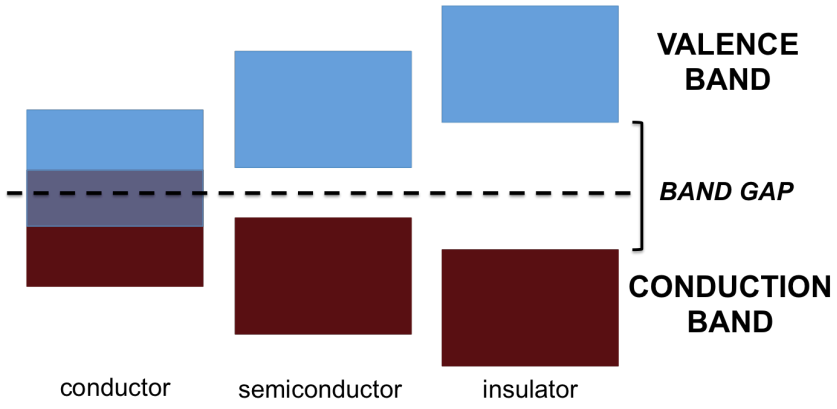

Figure 2.1 Band gap structures of crystalline solids.

A band gap exists between the valence and conduction bands, called the forbidden gap. In insulators, the forbidden gap is ≥5 eV, in semiconductors it is ~1 eV, and in conductors the bands merge together, allowing mobility of valence electrons between the gaps (Fig. 2.1). Electrons can be promoted from the valence band to the conduction band through ionizations, thermal fluctuations, and the absorption of photons. Semiconductors allow some mobility of valence electrons into the conduction band at room temperature, giving electrons conductivity. An electric field causes motion of electron-hole pairs, thus contributing to conductivity and creating further holes to be filled with electrons. Conductivity is enhanced through a process called doping: in order to add impurities and increase conductivity, electrons are injected into the conduction band (n-type semiconductor), or extra holes are added to the valence band (p-type semiconductor). In turn, removing electrons from the valence band decreases conductivity and increases resistivity.

An intrinsic semiconductor is one that has a perfect balance between electrons and holes; in reality, however, some impurities exist in materials. Silicon and germanium are considered to have optimal natural impurities. Silicon in particular has been widely used due to its ability to tolerate high electrical currents without succumbing

to the production of free electrons and holes (i.e., an avalanche breakdown). It has become available in the realm of radiation detection since the 1960s. Its forbidden gap is about 1.14 eV, and the W value (the energy required to liberate one electron-hole pair created by incident radiation) is 3.6 eV.

Solid-state semiconductor dosimetry dominates over other dosimetry methods for properties including:

- high energy resolution due to the capability of producing a high number of information carriers per radiation event;
- convenient size, as compared to bulky ionization chambers;
- possibility to vary the effective thickness of the sensor depending on the type and energy of the measured event.

2.2 Radiation dosimetry

This field of dosimetry deals with the quantification of radiation absorbed in its various forms, including photons, electrons, alpha particles, neutrons, protons, and various cosmic emissions (e.g., muons and pions). This thesis will focus on the measurement of electrons, since they are the main particle associated with natural potassium, and photons, used in radiotherapy.

Electrons are charged particles, and thus deposit their energy through direct interactions with the medium they enter, exciting and ionizing atoms, as well as emitting energy via bremsstrahlung. They often undergo multiple scatterings, and can lose their energy quickly in collisions with the electrons of the medium. Energy loss occurs at a steady pace. Photons, on the other hand, are neutral particles and deposit their energy through secondary interactions produced in the photon interactions with the medium. They can keep traveling within the medium before interaction occurs. The photoelectric effect dominates photon interactions at energies of <100 keV (dependent on material), where photoelectric absorption of

the incident photon occurs, completely transferring its energy to an electron. The electron is then emitted, accompanied by an Auger electron or a secondary photon. Compton scattering dominates for photons of energy between 100 keV and 10 MeV, where the photon transfers some of its energy to an electron, and then scatters. Pair production dominates at energies above 10 MeV, requiring a minimum photon energy of 1.022 MeV, and results in an electron and positron.

The junction of n-type and p-type semiconductors is especially relevant in radiation dosimetry. The boundary region between the two is called the depletion region and is almost entirely free of charge carriers. A potential applied to the region sweeps out the created charge carriers, with electrons going toward the n- side and holes toward p- side. Altering the bias voltage can change the physical size of the depletion region. The number of electron-hole pairs produced is proportional to the absorbed energy.

Dosimetry is the measure of radiation energy absorbed per unit mass, and is most commonly measured in the SI unit of Gray, where 1 Gray equals 1 Joule/kilogram. Absorbed dose D is defined by the International Organization for Standardization according to:

$$D = \frac{d\bar{\varepsilon}}{dm} \tag{2.1}$$

where $d\bar{\varepsilon}$ is the mean energy imparted to matter of mass dm [10].

Hereafter, the concept of dose branches out into the respective fields of luminescence dating and medical physics.

2.2.1 Dose: luminescence dating

Quartz and feldpspar, the two most abundant minerals on Earth, themselves serve as natural dosimeters by absorbing and storing energy as trapped electrons. These electron traps can then be emptied by heat or by exposure to photons of various wavelengths, causing luminescence. The intensity of the emitted luminescence is in

turn related to the growth of the absorbed dose. The fundamental assumption in luminescence dating of sediments is that the minerals have been "bleached" prior to burial: the charge traps have been emptied by sunlight and thus any record of radiation exposure prior to burial has been erased [11].

The radiation energy absorbed by sediments is termed the "equivalent dose" (D_e), because it accounts both for the amount and type of radiation absorbed by the material.

2.2.2 Dose: medical physics

In medical physics, the concept of dose revolves around the biological effect that radiation has on organs and tissues in the human body, rather than pure energy deposition. The biological effect stems from the local rate of energy deposition along the particle track and is influenced by the linear energy transfer (LET). Heavy charged particles have a high LET, whereas the lighter electrons have a low LET: thus the same dose will have a greater biological effect in the case of alpha particles, as compared to electrons.

For uncharged particles (e.g., photons), this concept is further addressed by the measurement of kerma, forming the basis of medical physics dose calculations. Kerma is defined by the kinetic energy released per unit mass, and is approximately equal to the absorbed dose for low energy photons, but is greater than the absorbed dose in the case of higher energy photons, due to some of the particles escaping the medium without being absorbed. Photons transfer their energy in a two-step process:

1. Primary uncharged particles transfer energy to secondary charged particles via the photoelectric effect, Compton scattering, or pair production.
2. Secondary charged particles transfer energy to the medium via excitation and ionization.

Kerma is usually measured as air-kerma, and then related to absorbed dose by accounting for the location of measurement, spatial distribution of radioactivity and packaging of the radiation source, photon scattering and attenuation due to various factors, and source anisotropy for the brachytherapy source addressed in this thesis. The precise mode of dose calculation is addressed in Chapter 7.

Chapter 3

Part 1

Retrospective dosimetry: dating of geological sediment

Accurate chronology is fundamental to the studies of archeology and geology. The correct temporal placement of biological and cultural remains and geological phenomena is essential in order to establish a timeline of events and piece together the complex evolution of hominins, the nature of their societies and migration patterns. Geological events, in turn, can further our knowledge on Earth's structure and evolution over time, and act as an aid in a multitude of related studies, including human evolution and dispersal.

3.1 Luminescence dating

Luminescence dating has been widely employed for chronology of archeological and geological materials [12-17]. Techniques such as thermoluminescence (TL), optically stimulated luminescence (OSL), and infrared stimulated luminescence (IRSL) are used to measure the luminescence signal of sediment. TL methods can be

applied to both quartz and feldspar [11], whereas OSL methods focus on quartz [18], and IRSL on feldspars [19]. Quartz is sensitive to wavelengths of blue/green photons, and feldspar is especially sensitive to infrared photons [20]. These dating methods can cover a wider range of ages than radiocarbon dating — from hundreds to hundreds of thousands of years [21]. Techniques such as post-IR IRSL [22, 23], violet stimulated luminescence (VSL) [24, 25] and thermally-transferred (TT) OSL methods [26] can potentially extend up to 1 million years. Furthermore, luminescence ages are derived directly in calendar years, without conversion systems, such as that applicable to radiocarbon years. Dating is performed directly on the mineral debris in sediments, as opposed to scarce organic materials. An advantage of OSL over TL is the simplicity of the procedure, that among other aspects, reduces the setbacks related to heating, such as alteration and oxidation of the sample [27]. Moreover, the OSL signal is easier and more completely reset by sunlight, than is the TL signal.

The luminescence age of sediment is calculated using two components: the equivalent dose, D_e (sometimes referred to as the paleodose) and the environmental dose rate, D_r, according to the following equation:

$$\text{Age} = \frac{D_e}{D_r} \qquad (3.1)$$

The equivalent dose is determined in Grays from the intensity of the OSL signal of the sample, calibrated against the radiation dose given in the laboratory. Most recently this has been done using the single-aliquot regenerative-dose (SAR) technique, that takes account of sensitivity changes due to laboratory treatments of the sample [27-29], as well as using single grains. A grain is the most fundamental unit of analysis in sediment dating, and thus D_e evaluation at the level of individual grains allows assessment of the distribution of the determined D_e values. Thus grains with favorable luminescence properties can be selected, sufficient sample bleaching prior to burial can be verified using statistical models, and outlier D_e values resulting from insufficient bleaching or post-depositional mixing can be rejected prior to age determination [27, 30-32].

3.2 Environmental dose rate

The environmental dose rate quantifies the radioactivity of the sample and the materials surrounding it. It is defined as the sum of the individual dose rate ($\dot{D}$) contributions from the alpha, beta, gamma, and cosmic ray particles that the dosimeter grains are exposed to throughout their burial period. Environmental dose rate contributors are primarily related to radioisotopes in the uranium and thorium decay series and potassium (^{40}K), that are naturally present in the environment, along with the cosmic rays penetrating the Earth's surface. The dose rate component of the age equation is the focus of this thesis, and is expressed as follows:

$$D_r = \sum \dot{D}_\alpha , \dot{D}_\beta, \dot{D}_\gamma, \dot{D}_{cosmic} \quad (3.2)$$

^{238}U and ^{235}U constitute natural uranium and occur in concentrations of 99.28% and 0.72%, respectively; both undergo alpha decay, and have respective half-lives of 4.47 x 10^9 y and 7.04 x 10^8 y. ^{232}Th constitutes 99.98% of natural thorium, also undergoes alpha decay, and has a half-life of 1.40 x 10^{10} y. ^{238}U and ^{235}U constitute natural uranium and occur in concentrations of 99.28% and 0.72%, respectively; both undergo alpha decay, and have respective half-lives of 4.47 x 10^9 y and 7.04 x 10^8 y. ^{232}Th constitutes 99.98% of natural thorium, also undergoes alpha decay, and has a half-life of 1.40 x 10^{10} y. Both the uranium and thorium series are characterized by complex decay schemes, containing 18, 16, and 11 daughter isotopes for ^{238}U, ^{235}U, and ^{232}Th, respectively. ^{238}U daughters include the elements Th, Pa, Ra, Rn, Po, At, Pb, Bi, Tl, and Hg, ending in the stable ^{206}Pb; ^{235}U daughters include the elements Th, Pa, Ac, Ra, Fr, At, Rn, Bi, Po, Pb, and Tl, ending in the stable ^{207}Pb; ^{232}Th daughters include the elements Ra, Ac, Rn, Po, Pb, Bi, and Tl, ending in the stable ^{206}Pb.

^{40}K is the isotope of natural potassium that undergoes beta decay into stable ^{40}Ca and ^{40}Ar with a half life of 1.25 x 10^9 y. ^{87}Rb is the radioactive isotope of natural rubidium that contributes a small proportion to the total dose rate (usually as an

internal contributor to K-feldspar grain dose rates) via beta decay, with a half-life of 48.1 x 10^9 y. Equation 3.2 is disaggregated into its respective dose rate components as follows:

$\dot{D}_\alpha$: ^{238}U and U, Th, Ra, Rn, Po, Bi daughter products; ^{235}U and Pa, Ac, Th, Fr, Ra, Rn, Po, Bi daughter products; ^{232}Th and Th, Ra, Rn, Po, Bi daughter products.

$\dot{D}_\beta$: ^{238}U and U, Th, Pa, Ra, Pb, Bi daughter products; ^{235}U and U, Pa, Ac, Th, Fr, Ra, Rn, Bi, Pb, Tl daughter products; ^{232}Th and Th, Ra, Ac, Pb, Bi, Tl daughter products; ^{40}K; ^{87}Rb.

$\dot{D}_\gamma$: ^{238}U and U, Th, Pa, Ra, Pb, Bi daughter products; ^{235}U and U, Pa, Ac, Th, Fr, Ra, Rn, Bi, Pb, Tl daughter products; ^{232}Th and Th, Ra, Rn, Ac, Pb, Bi, Tl daughter products; ^{40}K.

$\dot{D}_{cosmic}$: cosmic ray dose for muons (D_0) is determined for x, a depth below ground level, measured in hg/cm^2. x can range from surface-level to 10^4 hg/cm^2 of rock, at any altitude to 5 km. D_0 is quantified as follows [33]:

$$D_0 = \frac{6072}{(x+11.6)^{1.68}+75)(x+212)} \exp\left(-5.50\text{x}10^{-4}x\right) \quad (3.3)$$

Complete lists of the uranium and thorium decay series with their corresponding energies and dose rates can be found in Adamiec and Aitken (1998) [34]. The fundamental assumption is that the dose rate has been constant throughout the sample's burial period. Secular equilibrium (i.e. activity equilibrium of the parent and daughters) is also often assumed when only the parental concentrations of U and Th are measured (e.g., by inductively coupled plasma mass spectrometry). If disequilibrium is present, then its effect should be estimated and corrected, when necessary, using models such as those developed by Olley et al. (1996) [35, 36]. Moreover, water exhibits greater attenuating effects as compared to air, and thus its presence in sample pores must also be considered.

Cosmic rays have the highest effect upon environmental dose rates in the top meter of sediment. The range of alpha, beta, and gamma particles in sediment is much

lower: ~0.03, 3, and 300 mm, respectively. While cosmic rays comprise just a small fraction of the total dose rate, and U and Th are normally present in 1-10 ppm concentrations, K accounts for 0.5 - 3% of the sample weight [37]. ^{40}K typically accounts for ~40-70% of the environmental dose rate, and up to 80% of the total beta dose rate.

3.2.1 ^{40}K beta dose rate

Beta dose rate can be measured either by quantifying the ^{40}K concentration within the sample, or by direct counting of the sample beta particles. The dose rate is then estimated based on the infinite matrix assumption, postulating that the dose rate is equal to the rate of energy emission per unit mass (Aitken, 1985). Dose rate conversion factors have been determined using the data compiled in Evaluated Nuclear Structure Data Files by the National Nuclear Data Center in the Brookhaven National Laboratory, as reported in Table 3.1.

^{40}K		
Natural abundance (mg/g)		0.119
Beta $\bar{E}$ (MeV)		0.499
Gamma $\bar{E}$ (MeV)		0.1557
Specific A (Bq/kg), 1% nat. K		
	β	282.5
	γ	33.73
Dose rate at 1% (Gy/ka)		
	β	**0.7982**
	γ	**0.2491**

Table 3.1. ^{40}K isotope data for each disintegration, and natural abundance of 116.7 ppm, modified from Guérin et al. (2011) [38].

^{40}K distribution within sediments may be inhomogenous due to the non-uniform distribution of K-feldspar grains and the spatially variable presence of other K-bearing materials (such as hearth ash and phosphates). In single-grain OSL dating, sand-sized grains (e.g., 180-212 μm in diameter) are routinely used, and thus small-

scale beta variability can result in a large coefficient of variation in dose and dose rate. Precise information on the location of the dose rate sources in relation to the dated grains would therefore enable a more accurate estimate the environmental dose rate. Moreover contextual information on the microstratigraphy of the sample would allow the assessment of potential diagenesis and post-depositional disturbances that may affect the distributions of measured doses and dose rates.

Beta dose rates are commonly measured on homogenized, bulk samples of much greater sizes than the range of beta particles using techniques such as beta counting or inductively coupled plasma mass spectrometry/optical emission spectroscopy (ICP-MS/OES). These bulk-sample approaches may not be informative for individual grain distributions [39]. To better interpret the dispersion of single-grain D_e values and improve the accuracy and precision of ages obtained using single-grain OSL dating, D_r values corresponding to the respective individual grain D_e values should be obtained, to ultimately achieve "grain by grain" dating [20, 40].

3.3 Project aim

The aim of this study is to employ solid-state semiconductor dosimetry to develop a method of deriving spatially resolved dose rates for intact sediment samples, thereby preserving their microstratigraphic integrity and estimating dose rates at a spatial resolution that accounts for the range of beta particles in sediment. This aim was divided into three components:

1. Determine the feasibility of measuring dose rates in sediment using the proposed detector.
2. Develop a measurement procedure and visualize radiation 'cold' and 'hot' spots within the samples; calibrate the detector in order to convert measurement output to environmental dose rates.
3. Apply the developed method to determine spatially resolved dose rates for a selection of real sediment samples.

Chapter 4

Radiation inhomogeneity in sediments

In single-grain OSL dating techniques, D_e values are often obtained from a small proportion (e.g., 20% or less) of the measured grains following a meticulous rejection process [27, 41, 42]. While strict selection criteria may be used for the dosimeter grains, D_r measurements fail to deliver similar accuracy. The scatter in the D_e distribution is directly affected by the radioemitter distribution within samples, and hence, their D_r values. Grains located in close proximity to radioactive sediment components such as K-feldspar, zircon, and monazite receive higher amounts of dose, as compared to the grains positioned further away. Accounting for the scatter in the dose rates, in addition to that of the equivalent doses, is especially important due to the high radiation gradients within sediments.

4.1 Previous studies

Radiation inhomogeneity within samples has been addressed in previous studies using both simulation and experimental methods. Simulation studies employ modeling algorithms to quantify dose rate distributions, while experimental studies

directly measure sample radioactivity, and have sometimes been applied in combination with modeling techniques.

4.1.1 Simulation approach

Monte Carlo (MC) methods have commonly been utilized to expedite the long measurement times required by experimental studies, as well as to achieve high spatial accuracies. The MC radiation transport code enables the estimation of accumulated doses in samples of various geometries, packing arrangements, and elemental compositions. Complex distributions of dosimeter and source grains within the sample can be achieved, and various radionuclide concentrations can be assigned to the sources in order to emulate the real sediment context. Although previous simulation studies involve simplifications of sample geometry by utilizing approximations such as random grain packing [43] and pure statistical modeling [44], they have demonstrated the importance of accounting for beta heterogeneities in dose rate calculations. Geant4, a MC simulation toolkit developed by CERN [45, 46] allows higher levels of geometrical complexity, and has been incorporated into the DosiVox modeling software customized for sediment applications [47]. DosiVox provides a user-friendly interface for sediment dose modeling, allows different levels of geometrical complexity, and has been shown especially useful in the cases where the assumption of an infinite dose matrix is not applicable [47-49].

Other studies have used a combination of MC simulations and experimental measurements to assess the influence of beta heterogeneity. Nathan et al. (2003) [50] and Cunningham et al. (2012) [51] have used Monte Carlo N-Particle (MCNP) Transport Code in combination with physical α-Al_2O_3: C grain measurements, concluding that beta heterogeneity affects the distribution of in single grain D_e values. Both cases, however, were lacking in agreement between experimental and simulation results. Moreover, in the case of Cunningham et al. the experimental component involved neutron bombardment of the sample to achieve sufficient irradiation of the dosimeter grains within the two-week timeframe of measurement.

4.1.2 Experimental approach

Experimental measurements of spatially resolved dose rates in sediments constitute a challenge due to the inherently low levels of activity in natural samples. High detector sensitivity and effective background suppression are imperative to enable sample measurement at the desired spatial resolution. Moreover, detector stability over long measurement periods is essential; these can range from days to months. Previous studies have developed methods to visualize and quantify dose rate dispersion in sediments, employing techniques such as autoradiography, α-Al_2O_3: C grains, and fission tracks. Autoradiography methods have been successful in the visualization of the radioactivity within geological samples, allowing samples in various forms to be placed directly on the imaging plate to measure the intensity of the emitted radiation signal [52]. These studies have also found that the autoradiography detection limit is reached for some low-activity environmental samples [53]. α-Al_2O_3: C grains of 200-300 μm diameter have been mixed with sediments to quantify dose rate distributions using the SAR protocol, successfully measuring the D_r distribution and attributing a relative uncertainty of 18% to D_r inhomogeneity [54]. The fission track method employed for spatially resolved dose rate determination in U and Th isotopes allows a 20 μm spatial resolution; dose rates are estimated via measurement of fission track densities following neutron bombardment [55].

Other studies have employed X-ray spectroscopy [56], X-ray computed microtomography [57], and CCD imaging [58] for the visualization of potassium feldspars within sediments. These studies have further highlighted the possible deviations from the mean beta dose rate values, and the significance of highly concentrated radiation emitters in close proximity to dosimeter grains. Laser Ablation Inductively-Coupled Plasma Mass Spectrometry (LA-ICP-MS) has also been used to visualize and quantify concentrations of radioemitters [59].

4.2 Visualization of radiation hotspots using the Timepix detector

Solid-state dosimetry has not been extended to sediment measurements, primarily due to the low activity of sediment samples and, thus, the inability to discriminate sample emissions from the background noise. This study employs a highly sensitive pixelated semiconductor detector, the Timepix, to visualize radiation hotspots within sediment samples.

4.2.1 The Timepix

The Timepix is a hybrid-pixel detector that contains a 300-μm high-resistivity silicon sensor that is bump-bonded using Flip Chip® [60] technologies (Fig. 4.1). The sensor area is 1.98 cm^2 and contains a 256 x 256 array of 55 x 55 μm^2 pixels. Each pixel has to its own 14-bit counter, threshold discriminator, and preamplifier, and contains 65,536 independent readout channels, providing excellent spatial resolution [61]. It was developed by the Medipix2 collaboration, incorporating the Timepix readout chip into the conventional event-counter chip, enabling energy deposition measurement in the "time-over-threshold" mode. For energy measurement, the counter is incremented continuously during the period of time that the preamplifier output charge exceeds the threshold [62].

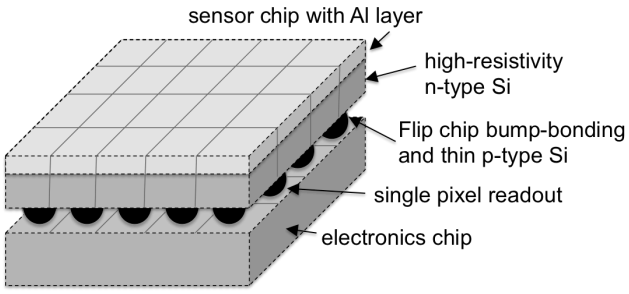

Figure 4.1 Timepix chip.

The detector is able to recognize particle types such as alphas, betas, gammas, and cosmic rays based on their energy deposition and morphology of their tracks [63]. Each particle is characterized by the shape of the cluster that it creates in the

detector pixels while depositing its energy in the silicon chip, which varies depending on the particle charge, velocity, mass, and angle of incidence. An incident particle deposits its charge by interacting with the silicon sensor, and electronic transport of the particle charge to the pixel preamplifiers results in a signal. Charged particles interact with electrons in the silicon, which can result in strong collisions in the case of beta particles, creating winding tracks within the detector, or create secondary short ranged electrons that deposit their energy quickly and involve nearer pixels, such as alpha particles. Energetic beta particles leave long, curly tracks (figures 4.2a,b,c), while less energetic betas of < 100 keV produce single, double, triple, and quadruple hits. Gamma particles deposit their energy indirectly through electrons, and thus their track shapes resemble those of the less energetic beta particles. Alpha particles are heavier and deposit their energy in the form of blobs (figure 4.2d).

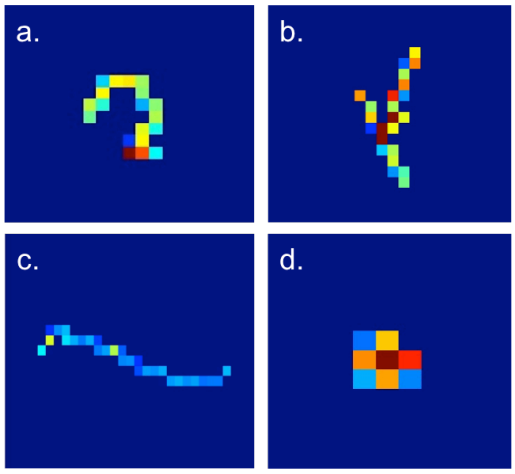

Figure 4.2 Cluster shapes of beta particle tracks (a, b, c) and a heavy blob characteristic of alpha particles (d).

Timepix operates on a frame-by-frame basis: a digital shutter opens and closes, after which the data collected in the pixels is read out. Frame length must be long enough for registered particle tracks to not overlap, and short enough to reduce the total number of frames and, thus, analysis time and data storage. It is set by the user and can be as short as 80 frames per second. Pixelman readout software is used for

measurement acquisition, allowing the user to select measurement settings such as the frame length, time of acquisition, measurement threshold, and the file type where the acquisition is stored [64]. The frame-by-frame visualization is displayed on the screen, where the individual particles detected are displayed as a heatmap of their energy deposition in each pixel (figure 4.3).

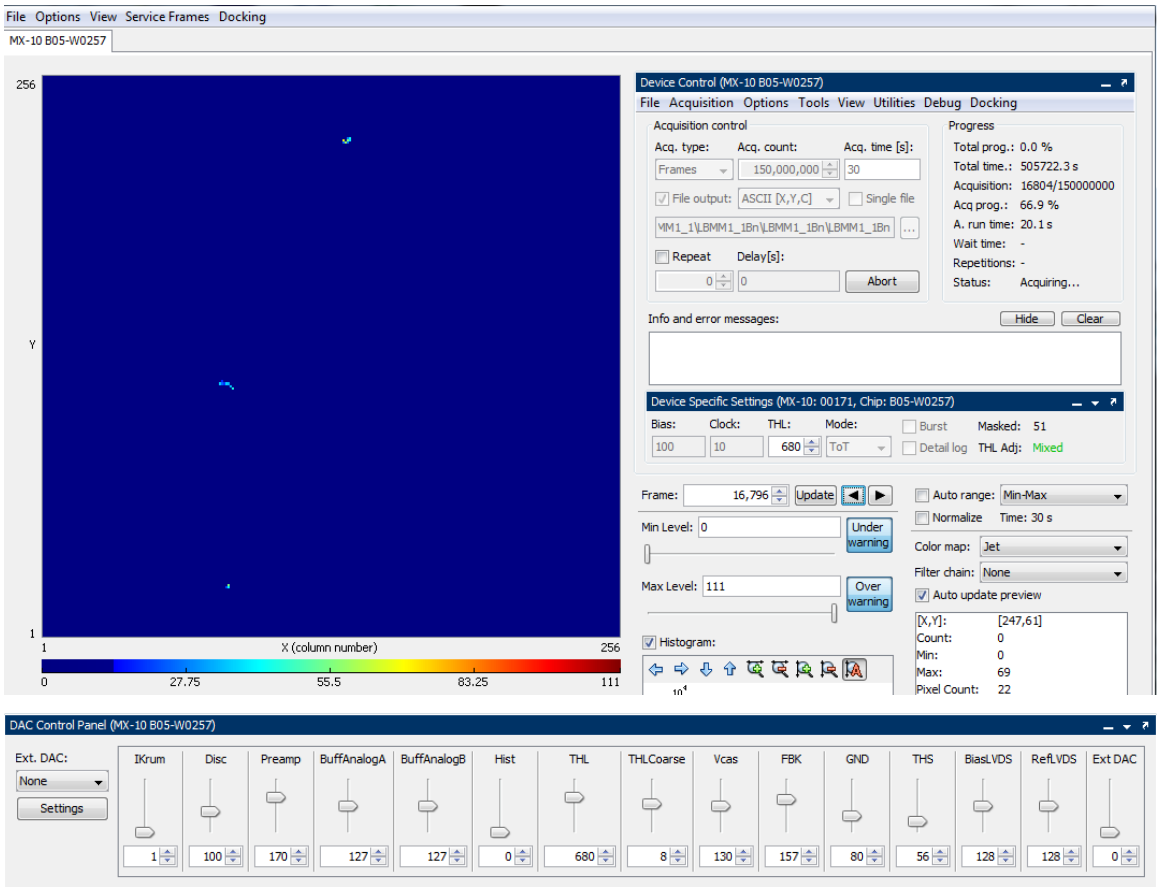

Figure 4.3 Example of output display using Pixelman software.

Individual frames are stored as 256 x 256 matrices, containing energy deposition or count data for each pixel. The Jablotron MX-10 Timepix chip used in this study is pre-calibrated, with linear parameters a and b, and non-linear parameters c and t, used to convert each TOT frame into pixel-by-pixel energies as follows:

$$TOT = a + bE + \frac{c}{t - E} \tag{4.1}$$

where TOT is the time-over-threshold response of the detector (ns), and E is the input energy (keV).

Energy calibration can be carried out assuming that all pixels have a uniform response, or by compensating for the differences in pixel response (i.e., an inherent property of the detector). Energy calibration is typically performed using four spectral lines: the 5.9 keV peak from ^{55}Fe, 59.5 keV peak from ^{241}Am, and two additional from X-ray fluorescence lines. The TOT value of single pixel hits is measured and fit to the most likely value of the spectrum, corresponding to pixel energy [65].

In order to ensure a uniform response among pixels a threshold equalization procedure is carried out with a fixed energy setting to align pixel thresholds using the background noise. This can be done either using the "noise edge", where noise is defined by pixels exceeding a certain noise value, or using the "centroid" method, where the center of the noise is determined using a Gaussian distribution. The latter method is recommended to better accommodate the pixel-to-pixel response variation over the entire chip. More details on this procedure can be found in [65]. DAC settings established during the centroid threshold equalization procedure are shown at the bottom of figure 4.3. This procedure also masks any existing dead pixels to prevent consistent over-response.

The acquired measurement frames are then run through cluster analysis, based on the Medipix Analysis Framework (MAFalda) that groups registered pixel hits into clusters [66]. The clusters are characterized according to a number of parameters, including the total number of pixels and inner pixels in each cluster, cluster TOT, energy, x and y centroids, length in the x-y directions, type, and the time of cluster registration. A "minimum bounding box" is drawn for each cluster, and used to

determine the length, width, x-y dimensions, and density. Clusters are then attributed to one of the six geometric types, characterizing the physics of the particle, as defined by the Institute for Advanced Experimental Physics at the Czech Technical Institute in Prague: small blob, medium blob, heavy track, heavy blob, straight track, and light track [63]. They are distinguished according to the cluster number of inner pixels, length/width ratio, and additional criteria (i.e., a light track is not straight, density value, total number of pixels). Beta particles are attributed to light tracks.

4.2.2 Background suppression

A 3 cm-thick lead container capable of enclosing the Timepix detector was used for all sediment measurements. The interior walls of the container were lined with a thin layer of aluminum to absorb backscattering. Measurement setup is shown in figure 4.4, with the Timepix positioned inside the lead box and connected to a laptop with Pixelman software. Figure 4.4b shows a sample placed over the Timepix sensor inside the lead container.

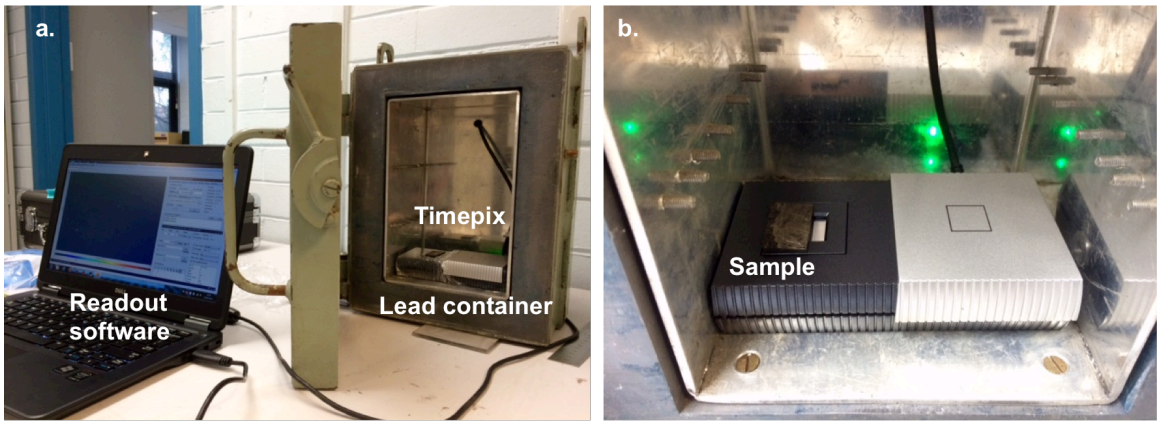

Figure 4.4 Measurement setup with the lead container (a) and sample placed over the Timepix for measurement (b).

Cosmic rays are characterized by particularly high energies and are able to penetrate through the lead shielding, but they also deposit their energy in particular energetic tracks in the silicon chip of the Timepix. Following measurement and

cluster analysis of the acquired frames, they were eliminated from sample analysis along with other heavy particle tracks, while curly electron tracks of > 100 keV, mostly pertaining to the ^{40}K betas, were selected for sample evaluation.

4.2.3 Initial feasibility studies

The aim of this study was to test the feasibility of radioactivity visualization in geological samples using the Timepix detector, starting with samples of high activity and progressing to samples of lower activity, which are more representative of sediment samples from the field.

4.2.3.1 High activity samples

The first geological sample selected for measurement on the Timepix was biotite, chosen due to its high ^{40}K content and, thus, naturally high levels of beta activity. A 13 x 18 x 3 mm^3 slice of the dark mica material was placed on the plastic exterior of the Timepix, about 2 mm above the detector sensor, covering approximately half of the chip (figure 4.4b). The measurement was acquired using the integral frame measurement setting, to test the ability of visualizing the region of the chip occupied by the radioactive material. A 2D 256 x 256 pixel hitmap of the preliminary measurement is shown in figure 4.5a, where the portion of the Timepix chip occupied by the biotite slice is clearly visible on the bottom half of the hitmap. The hitmap scale corresponds to the number of counts. The total counts acquired during the measurement in the Y pixel of the sensor are shown in Fig. 4.5b on a one-dimensional hitmap, demonstrating a range of 1200-1800 counts in the biotite region, and a range of 450-1100 counts for the region containing no sample, with the higher counts of the latter range attributed to scattering from the sample.

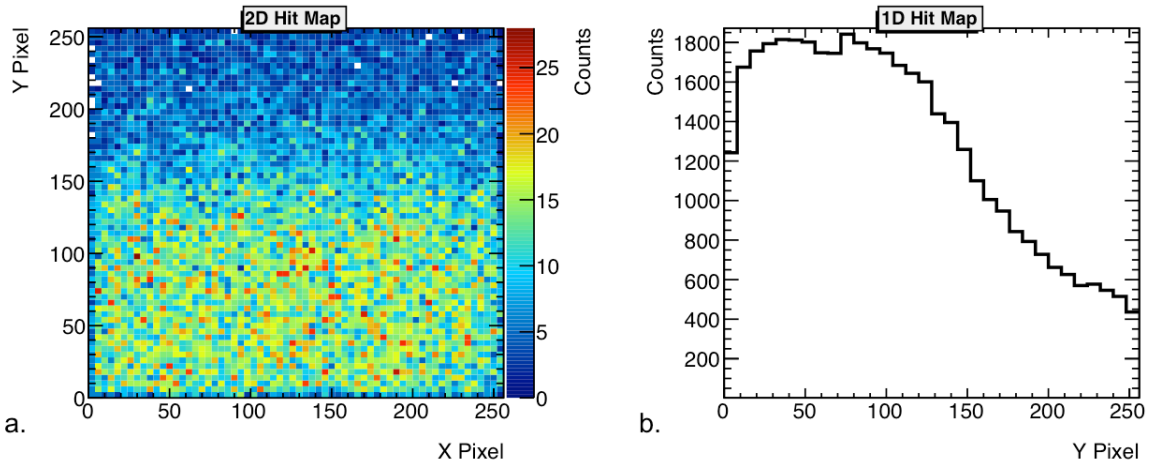

Figure 4.5 2D (a) and 1D (b) hitmaps of the biotite slice measurement.

The next sample was produced to represent a sediment sample with cold-spots and radioactive hot-spots distributed inside (figure 4.6a). Biotite spheres were embedded in a block of resin and measured on the Timepix for 6 days. The 2D pixel-by-pixel hitmap is shown in figure 4.6b, with the eight biotite spheres clearly visualized, containing ~3 times the number of counts as compared to the resin region of the sample.

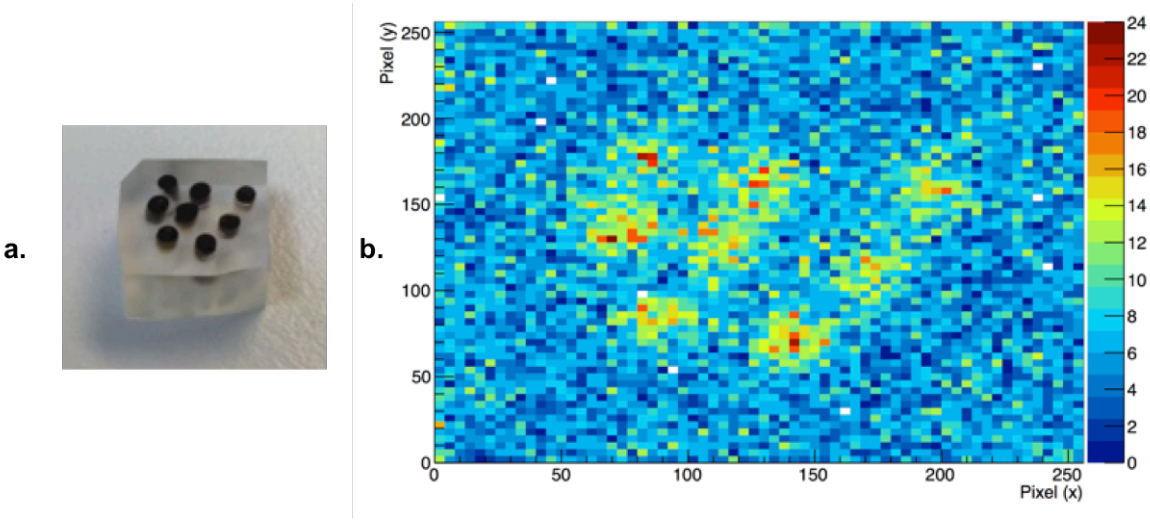

Figure 4.6 Biotite spheres embedded in resin (a) and the corresponding Timepix 2D hitmap of sample counts (b).

The next artificial sample was produced using biotite, quartz, and monazite grains, again held together by resin. Monazite was selected as an additional high-activity natural mineral containing high concentrations of thorium. The results of the 5-day measurement are shown on the 2D hitmap in figure 4.7. Monazite proved to be even more radioactive than biotite, completely overpowering the biotite emissions, and replicating the shape of the monazite sample component in its count distribution.

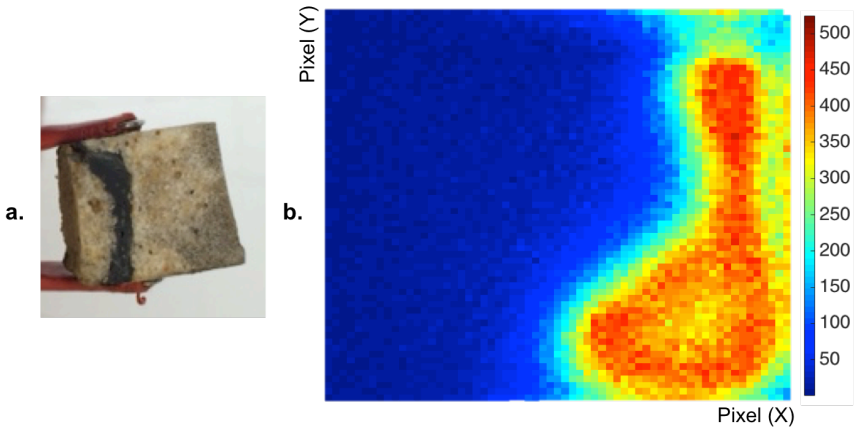

Figure 4.7 Quartz (light brown), biotite (black), and monazite (dark brown) sample (a) and the Timepix 2D hitmap of counts (b).

Thus, high activity geological materials were successfully visualized by the spatially resolved Timepix count distribution. The next step was to assess the detector's ability to detect significantly lower concentrations of radioactive materials in natural and artificially produced samples.

4.2.3.2 Lower activity samples

Diorite was selected due to its variety of ^{40}K radioemitters, including feldspar and biotite. The sample (figure 4.8a) was cut from a rock and not prepared in any other way (e.g., crushing, powdering or impregnating in resin). It was then measured for 11 days, and an average count rate of 2.58 counts/min was determined.
Measurement frames were analyzed with cluster analysis, and alpha and beta tracks were selected to visualize the radiation distribution in the sample. The

corresponding 2D hitmap is shown in figure 4.8b, where the radiation hot-spots are shown as increased count regions.

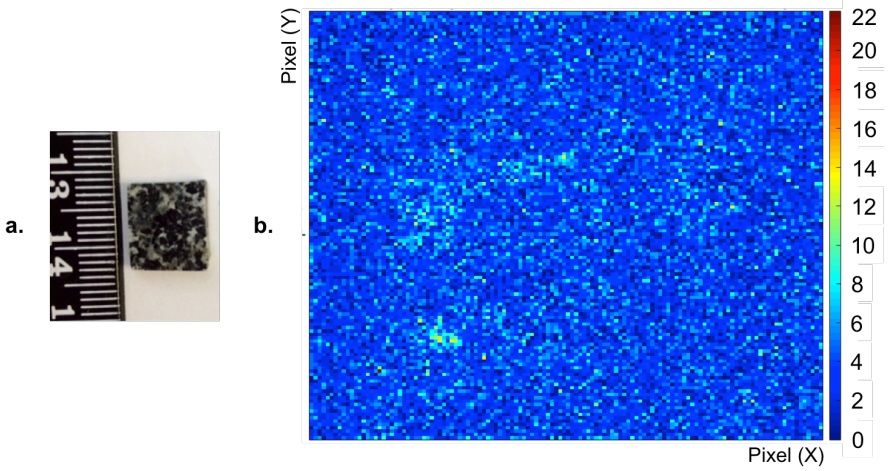

Figure 4.8 Diorite sample (a) and the corresponding 2D hitmap of counts (b).

An artificial sample was also fabricated to provide an appropriate model of a sediment sample. 200-300 μm diameter grains of natural feldspar and purified quartz were uniformly mixed in respective concentrations of 7 and 93%, and solidified using epoxy resin (figure 4.9a). The sample was measured on the Timepix for 21 days, and subjected to cluster analysis selecting electron tracks, arriving at a total dose rate of 2.36 counts/min. The resulting 2D hitmap of these particle tracks is shown in figure 4.9b. A few radiation hotspots are visible, despite attempted uniform mixing of the sample, demonstrating the high spatial resolution of the Timepix.

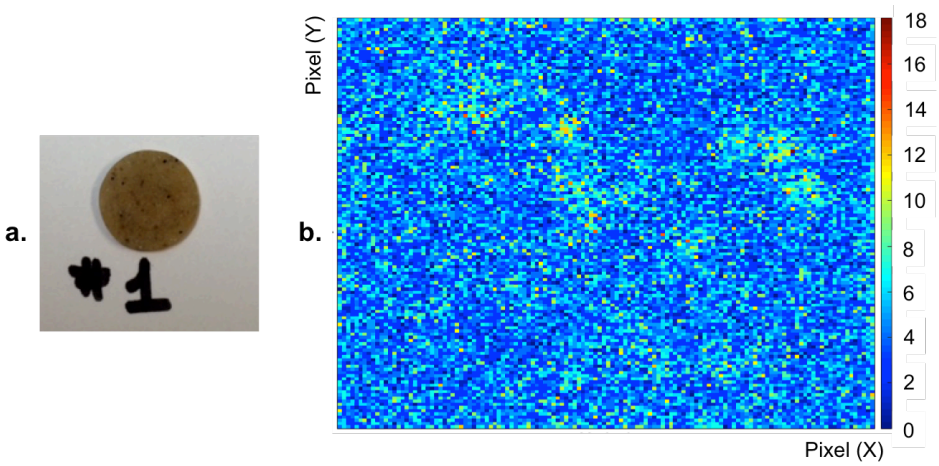

Figure 4.9 Custom sample composed of 7% feldspar and 93% quartz (a) and the corresponding 2D hitmap of counts (b).

These measurements served as preliminary estimates of the measurement time required to obtain radioisotope visualization for high- and low-activity sediments. As a result, measurement time was estimated to lie in the range of 4 days to one month, depending on the radionuclide concentrations of the particular sample. Importantly, the Timepix showed a stable response over the 21-day measurement period.

4.3 Conclusions

Previous studies have highlighted the need for further development of experimental methods to quantify spatially resolved dose rates in sediment samples, as discussed in section 4.1.

The challenge of minimizing background noise for sediment sample measurement on the Timepix has been addressed through a combination of physical shielding and post-acquisition data analysis. Lead shielding resulted in a noise reduction of more than 50%. Background particles of uncharacteristically low and high energies in the

context of the expected ^{40}K emissions could be discriminated using cluster analysis, allowing for the sole analysis of beta tracks deposited in the detector.

Preliminary feasibility studies employing real and artificial samples of high and lower radiation activity demonstrated the ability of the Timepix to visualize radiation hotspots within samples and the potential to derive spatially resolved beta dose rates for natural sediment samples.

Chapter 5

Spatially resolved dose rates in sediment samples: development of method

5.1 Aim of this chapter

Following the preliminary feasibility studies described in the previous chapter, the next step was to develop a procedure for Timepix sediment measurements and establish a calibration to convert the measured count rates in silicon to dose rates in sediment.

This involved both MC simulations and experimental methods. Both relative and absolute dose rate calibration functions were derived, beginning with the former and concluding with the latter, and thus minimizing dose conversion uncertainties.

5.2 Geant4 simulation component

MC simulations were used to facilitate Timepix method development, addressing both the measurement procedure and data analysis. Experimental setup was simulated by modeling the Timepix sensor as a 14 x 14 x 0.3 mm^3 silicon box with

an overlaid grid containing a 256 x 256 voxelized readout geometry, emulating individual pixels of the Timepix. Energy deposition in each voxel and its corresponding x-y coordinates were scored for each incident particle, and reported in the simulation output file. Geant4 version 10.1 with *EmStandardPhysics_option3* for particle electromagnetic interactions and Geant4 Radioactive Decay Model were included in the Physics List. The sample was modeled as a 10 x 10 mm^2 piece of SiO_2 containing a uniform distribution of ^{40}K.

The first simulation serving as validation for the geometry and ^{40}K decay was a reproduction of the biotite study described in section 4.2.3.1. The results of the 1-week measurement simulation are shown in figure 5.1, with the number of particles per unit energy (keV) plotted as a function of the energy deposition in the Timepix. The experimental results, shown in black, demonstrated good agreement with the simulation results, shown in red. A minor discrepancy between the two in the lower energy region (< 50 keV) is explained by the lack of background noise in the Geant4 environment.

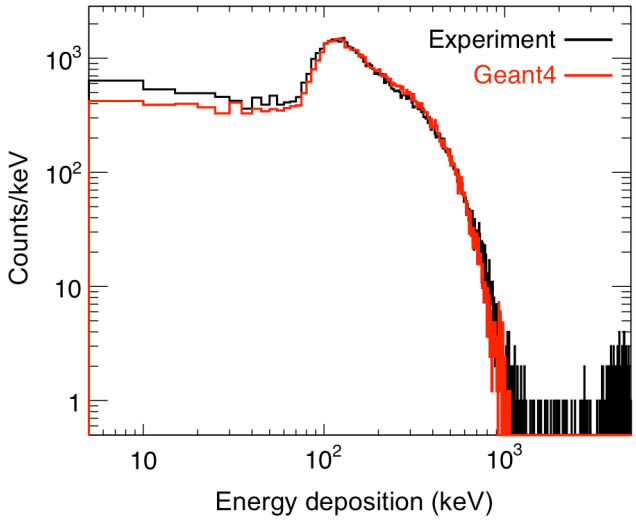

Figure 5.1 Experimental and Geant4 simulation results for the biotite sample measurement on the Timepix detector.

Geant4 simulations were then used to determine optimal sample-to-detector distance and sample thickness, as well as to derive an edge correction for pixels located close to the sample edge.

5.2.1 Sample-to-detector distance

To determine optimal placement of the sample with respect to the detector sensor, the biotite sample distance from the detector chip was varied between 0 and 10 mm in the simulation geometry. Counts detected in the silicon detector chip were evaluated for each of the 10, 7.5, 5, 4, 3, 2, 1, and 0 mm biotite distances from the detector. Figure 5.2 shows the counts detected by the Timepix as a function of the sample position on the sensor for all sample-to-detector distances.

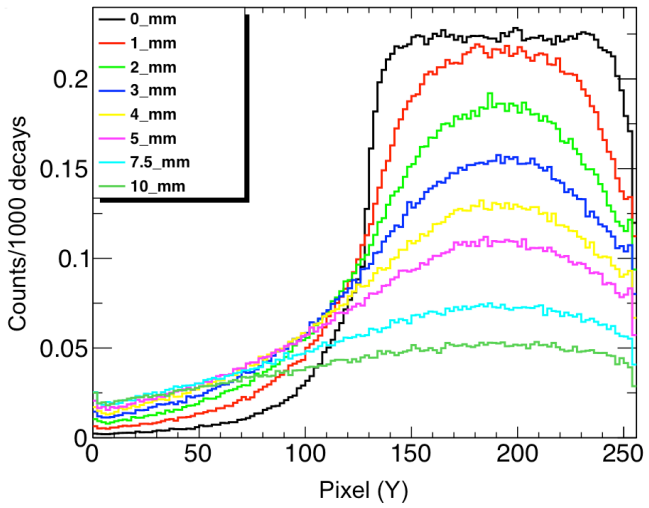

Figure 5.2 Timepix counts as a function of sample position on the Timepix for a range of source-to-detector distances.

These results show that decreasing the sample-to-detector distance from the 2 mm position used in the biotite study to 0 mm resulted in a 25% increase in detected counts. Thus, to maximize sample counts, the sample should be placed directly on the detector sensor.

5.2.2 Sample thickness

Simulation geometry was modified to correspond to sample placement in the center of the Timepix sensitive area, and simulations were run to evaluate the effect of

increasing sample thickness. The schematic of the simulation geometry is shown in figure 5.3a, where the gray slab represents the Timepix silicon sensor, and the orange cube represents the SiO_2 sample. Figure 5.3b shows the beta (white) and gamma (green) particles resulting from the uniform ^{40}K decay within a 10 mm-thick sample, outlined in red, that are incident on the yellow Timepix sensor.

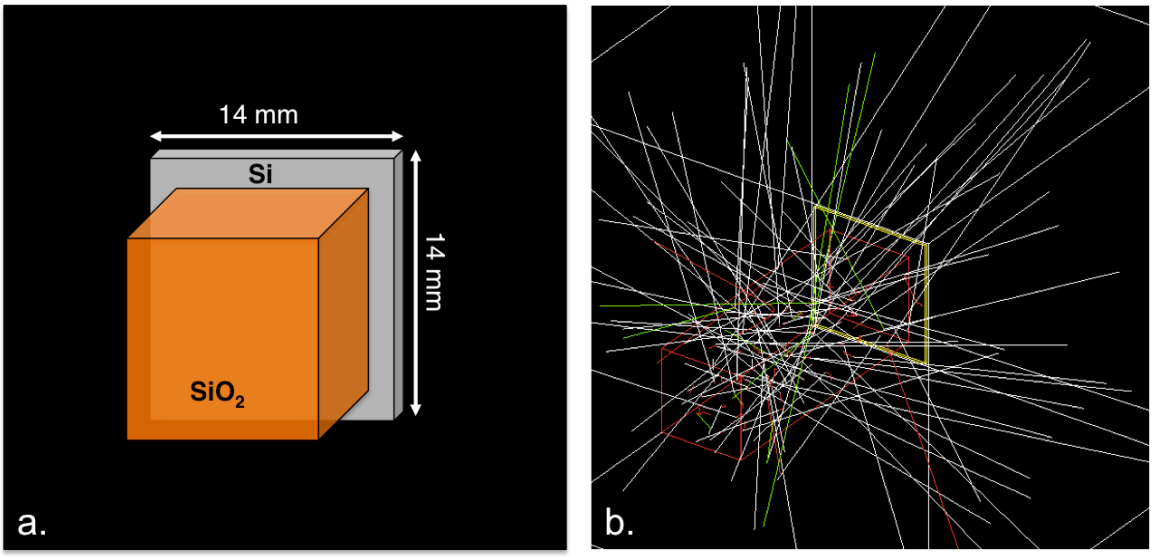

Figure 5.3 Schematic of the Geant4 simulation geometry, where the gray slab represents the Timepix silicon sensor, and the orange cube represents the SiO_2 sample (a), and the uniform emission of the ^{40}K decay particles arising from the sample (b).

The z-dimension of the SiO_2 sample was modified between simulation runs to test thicknesses of 0.1, 1-10, 15, 20, and 30 mm. The results of these simulations are shown in figure 5.4. A plateau in the detected counts per pixel resulted at thicknesses of ≥ 3 mm, similar to the known range of beta particles in sediment.

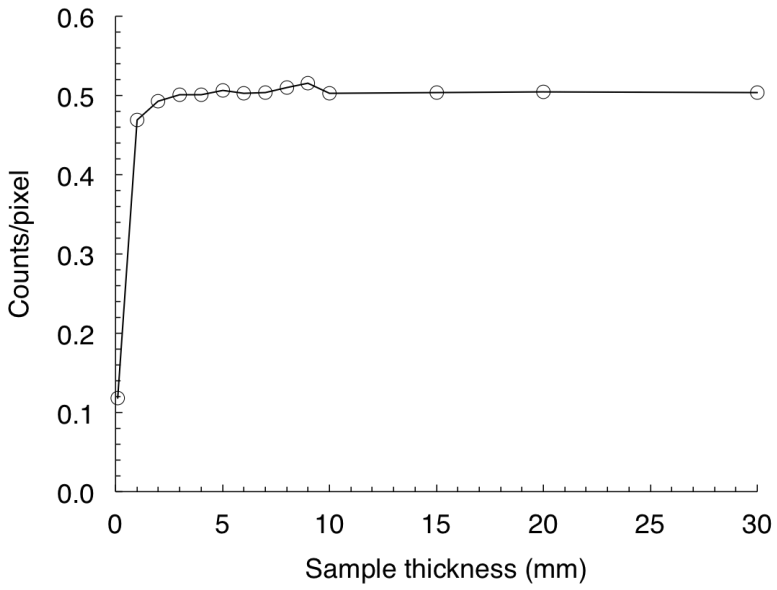

Figure 5.4 Clusters/pixel detected by the Timepix as a function of sample thickness.

This plateau is explained by beta absorption inside the sample, from which it was concluded that sample thickness should be kept at 3 mm to maximize detected counts and optimally visualize the radioemitter distribution within the sample.

5.2.3 Edge correction

When a sample of finite size is placed on the detector sensor (which is also of finite size), a decrease in sample emissions incident on the detector is observed close to the sample edge, due to the lack of 2π geometry of emissions. An edge correction was derived as a function of pixel proximity to sample edge, utilizing the spatially resolved Geant4 simulation results of a 3 mm-thick sample positioned on the Timepix sensor. The simulation output matrix of the scored particle positions was converted into a binary matrix, where the pixels below the sample area were assigned a value of 1 and pixels outside this area were assigned a value of 0. Pixels were grouped into clusters, and the proximity of each cluster to the sample edge was defined by the sum of the binary matrix, weighted by a Gaussian kernel. Higher pixel values indicated proximity to the center of the sample, while lower values indicated proximity to the edge. Normalized counts as a function of pixel proximity

to sample edge, defined in arbitrary units and normalized to unity at the sample center, are plotted in figure 5.5.

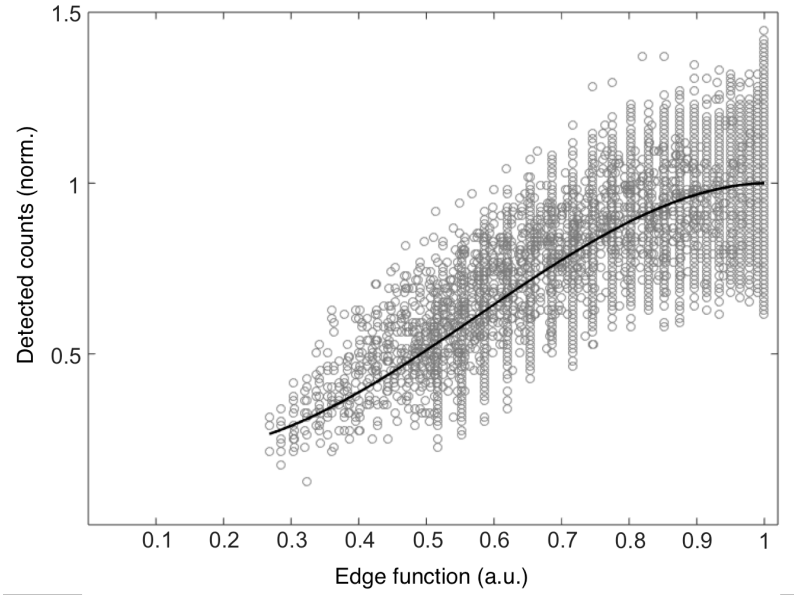

Figure 5.5 Edge correction function (arbitrary units).

These results were then fitted with a polynomial function, f (i.e., the correction factor that defines the degree of count adjustment based on the fraction of detected counts in relationship to the detection rate at the center of the sample), determined as follows:

$$f(d) = -2.3875d^3 + 4.1156d^2 - 1.0169d + 0.2888 \qquad (5.1)$$

Each pixel underneath the sample must be defined in terms of its proximity to the edge of the sample, d. Its corresponding count rate is then adjusted by multiplying the measured counts by $1/f$.

5.3 Sample preparation and measurement setup

There are two main requirements for geological sample measurement on the Timepix: they must be consolidated to prevent potential damage to the highly sensitive detector window, and sufficiently small for direct placement on the sensor.

5.3.1 Sample preparation

Geological samples were impregnated with epoxy resin for sample consolidation according to the method of geoscience sample mounting applied in the University of Wollongong (UOW) micromorphology laboratory [67]. A plaster mold was used to encase the sample, placed inside a vessel, and epoxy resin was poured around it to allow sample uptake of the resin via capillary action. A 7:3 proportion of resin and styrene, respectively, were combined, and MEKP catalyst was added to allow the mixture to harden. Once the sample was completely dry, it was cut into 10 x 10 x 6 mm^3 subsamples using an IsoMet low-speed cutting machine for measurement on the Timepix. Both sides of the sample were then measured.

5.3.2 Measurement setup

A thin strip of mylar film was placed between the detector sensor and the sample to provide protection against scrapes (the beta particle range was unaffected). Measurement setup is shown in figure 5.6a with a sample positioned over mylar film on top of the Timepix sensor.

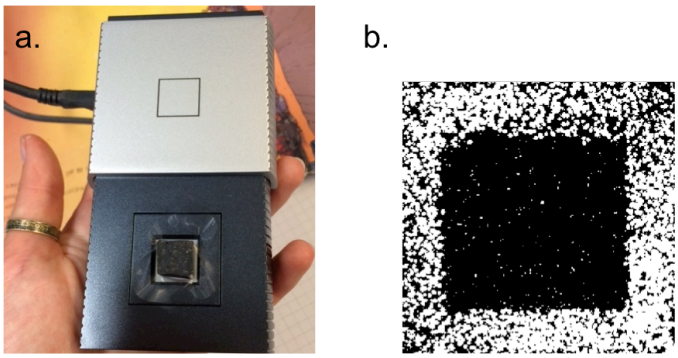

Figure 5.6 (a) Timepix detector with a sample placed over mylar film. (b) Alpha particle outline of the sample position on the detector's sensitive chip.

Once the sample had been placed for measurement, an outline of its position was created using an alpha ^{241}Am source. The boundaries of the sample area were delineated by holding the source above the measurement setup for a sufficient amount of time to produce a precise outline of the sample shape on an integral measurement frame displayed in the Pixelman software (figure 5.6b).

5.4 Dose rate calibration

The following sub-sections describe the methodology used to derive a calibration curve to convert the Timepix count rate (counts/pixel) into environmental dose rate (Gy/ka), applying both relative and absolute methods.

5.4.1 Relative calibration

A relative calibration was derived by measuring custom-made calibration samples of varying radioactivity concentrations on the pre-calibrated beta counter and the Timepix detector, and then relating the beta counter dose rates to the Timepix count rates.

5.4.1.1 Sample preparation

Two geological minerals, biotite and quartz, were selected for the radioactive and nonradioactive components, respectively. Biotite was selected as an easily obtainable mineral containing a high concentration of ^{40}K. Quartz was extracted from purified sand that has been treated with hydrofluoric acid to dispose of organic materials, carbonates and feldspars, and then subjected to solutions of hydrogen peroxide, hydrochloric acid and heavy mineral separation. The grain diameter range was selected as approximately 200-350 μm to keep the grains uniform for homogenous mixing. A total of five calibration samples were created containing approximately 100, 80, 60, 40, and 20% biotite content by mass, with the rest of the sample occupied by the nonradioactive quartz. Timepix samples were prepared as described in section 5.2.1.

Beta counter samples were crushed and left for two weeks prior to measurement to allow for secular equilibrium of radon and its daughter products. The samples were not consolidated, to comply with the powder form of the beta counter calibration source used to quantifying the beta environmental dose rate.

5.4.1.2 Beta counter measurement

A Risø GM-25-5 beta counter was used to quantify the beta dose rate in Gy/ka. The instrument consists of a gas flow counter (99% argon, 1% butane) with five Geiger-Mueller (GM) tubes and a common guard counter [68, 69]. The beta counter is housed inside a 10 cm-thick Pb bunker to reduce background interactions. A sample of Nussloch Loess (Nussi) that had been measured previously by high-resolution gamma spectrometry, and for which the dose rate is well-established [70], was used for the beta dose-rate calibration [71].

Five 25 mm-diameter cylindrical pots were positioned on a sliding vessel to ensure setup reproducibility. Three of the pots were filled with the powdered sample, one with the powdered Nussi reference standard, and one with MgO as background. The

measurement was run for 24 hours using 1-hour cycles that simultaneously measure the 5 samples.

To convert the measured count rate into dose rate, the three replicate sample measurements were averaged and compared against Nussi, following subtraction of the background count rate. The dose rate was then determined using previously established conversion factors [38]. The errors associated with the final dose rate are quantified as the counting statistics of each sample, combined in quadrature, and other instrumental reproducibility uncertainties (e.g., varying efficiencies of the GM tubes), as detailed in Jacobs and Roberts (2015) [71]. The dose rate error of the Nussi standard has been quantified at 1.8% from the concentration uncertainties of U, Th, and K [70].

5.4.1.3 Results

The post-cluster analysis beta particle count rates calculated for the uniform (central) region of the sample on the Timepix detector for the five calibration samples are plotted against the corresponding dose rates measured using the beta counter in figure 5.7. A calibration curve was derived to convert the Timepix-measured count rate into beta dose rate:

$$D_r = 7E{+}06 * C_{Tpx} - 5.499 \qquad (5.2)$$

where D_r is the beta dose rate (in Gy/ka) and C_{Tpx} is the count rate measured using the Timepix detector (counts/s/pixel).

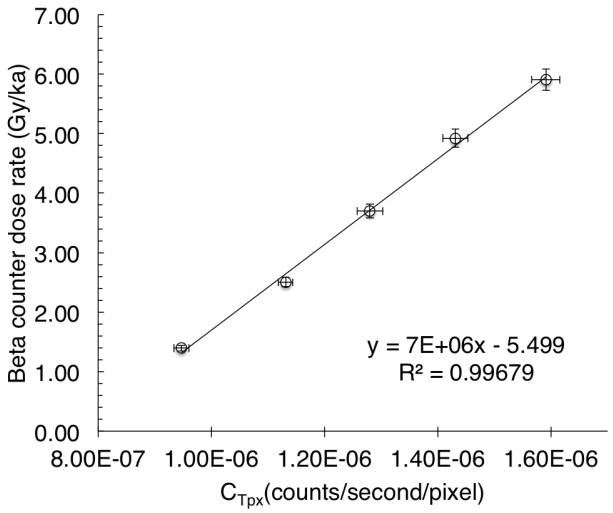

Figure 5.7 Timepix count rate to beta counter dose rate calibration curve. Errors are shown at 1σ.

5.4.1.4 Discussion

Calibration samples were assumed to contain a uniform distribution of biotite and quartz minerals with resin occupying only the pore spaces between the grains. The linearity of the calibration function (figure 5.7) would appear to justify this assumption.

Measurement uncertainties are attributed to errors associated with the Timepix detector and beta counter. Beta-counter errors have been quantified by Jacobs and Roberts (2015) [71]. Random errors include those arising from instrument fluctuations, reproducibility among replicates, counting statistics, and variation in the MgO background. Systematic errors associated with the beta counter are estimated at ~1.8% for the Nussi reference standard and ~2% for the dose rate conversion factors of Guerin et al. (2011) [38].

The Timepix count rate error was estimated by assuming a Poisson distribution, and calculated as the square root of the total number of detected counts. The average relative error associated with converting the Timepix count rate to beta dose rate (using figure 5.7) was calculated as 3.16% for the beta counter and 1.50% for the

Timepix detector, which gives a total relative error on the calibration curve of 3.50% for the total Timepix measurement area (all errors at 1σ). The error arising from the conversion to Gy/ka is both small and systematic between pixels.

Although this calibration method is acceptable, beta-counter samples were placed in plastic pods in powder form, whereas Timepix samples were fabricated using intact grains embedded in resin, thus relating a higher dose rate to a lower one. Moreover, a relative calibration method combines the errors of the two dose rate methods, increasing the total calibration curve uncertainty.

5.4.2 Absolute calibration

5.4.2.1 Materials and methods

IAEA standard materials of IAEA-RGK-1, IAEA-RGTh-1, and IAEA-RGU-1, were obtained for Timepix calibration of potassium, thorium, and uranium dose rates, respectively. The potassium standard was produced from 99.8% potassium sulphate, while the uranium and thorium standards were produced by the dilution of uranium and thorium ores containing respective concentrations of 7.1% and 2.9%, mixed with floated silica powder, and verified for sample homogeneity and radionuclide equilibrium by the supplier.

Three samples of varying isotope concentrations were prepared using MgO material for radioisotope dilution. Potassium samples contained 100, 24, and 8% concentrations of RGK-1 by mass, with corresponding dose rates of 39.6, 9.6, and 3.0 Gy/ka, respectively. Thorium samples contained 100, 49, and 12% concentrations of RGTh-1, with corresponding dose rates of 22.2, 10.9, and 2.7 Gy/ka, respectively. Uranium samples contained 100, 23, and 5% concentrations of RGU-1, with corresponding dose rates of 55.3, 12.7, and 2.7 Gy/ka, respectively. The dose rates were estimated using the conversion factors of Guérin et al. (2011) [38].

All samples were produced as described in section 5.2.1 and measured for 3-4 days to obtain adequate statistics of the registered counts. Post-cluster analysis beta

particle emission rates were then evaluated. Background counts were measured using a small block of resin for a 3-week count acquisition on the Timepix chip.

5.4.2.2 Results

Three calibration functions were derived for the three isotopes, relating Timepix count rate (counts/pixel/second) to environmental dose rate (Gy/ka/pixel). The background-adjusted calibration functions are plotted in figure 5.8, and were derived as follows:

$$D_r\,(K) = 2.9E{+}06 * C_{Tpx} \quad (5.3)$$

$$D_r\,(Th) = 3.6E{+}06x * C_{Tpx} \quad (5.4)$$

$$D_r\,(U) = 3.3E{+}06x * C_{Tpx} \quad (5.5)$$

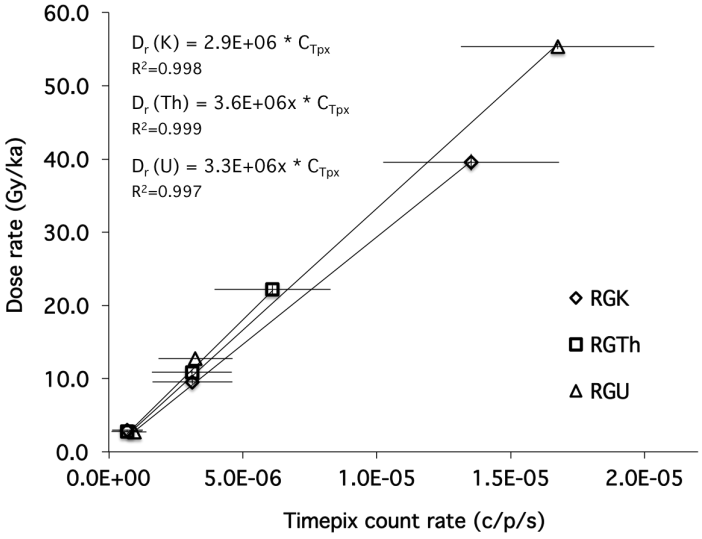

Figure 5.8 Timepix absolute calibration results for K, Th, and U dose rates.

The error bars in figure 5.8 reflect the error on the pixel (i.e., 55 x 55 μm^2) spatial resolution and are shown at 1σ. The corresponding R^2 values of the linear fit are 0.998, 0.999, and 0.997 for K, Th, and U, respectively.

5.4.2.3 Discussion

Calibration count rate errors for each 55 x 55 μm^2 pixel are 24.3%, 22.2% and 35.4%, for K, U and Th, respectively, decreasing to 5.7%, 7.4% and 11.8% at a 1 mm^2 resolution (i.e., containing counts for 18 x 18 adjacent pixels). The relative standard uncertainty of the IAEA standard is quantified as 2.86%, yielding total uncertainties (at 1σ) of 5.7%, 5.2% and 8.3% for the potassium, uranium and thorium dose rates, respectively, at the 1 mm^2 spatial resolution.

The spatially resolved Timepix beta particle count rate in counts/pixel/second can be converted into an environmental dose rate at the desired spatial resolution using the determined count rate-to-dose rate relationship. All three curves are based on the beta particle dose rate, which is more relevant for dating than the dose rate due to alpha particles, which are also prominent in the uranium and thorium radionuclides, but which have a much shorter range and are commonly removed as a dose-rate contributor by acid-etching of sand-sized grains prior to D_e measurement.

5.5 Sediment dose rate measurement: procedure outline

Following the Geant4 simulation and experimental method development described in sections 5.2 - 5.4, a procedure was established for sediment dose rate measurement with the Timepix, as outlined below:

1. Sample of sediment is resinated and cut to obtain a consolidated sample of 10 x 10 x 6 mm^3 dimensions.
2. Sample is placed on the Timepix sensor, separated by mylar film.
3. Sample position on the sensor is delineated using an ^{241}Am source on an integral measurement frame.

4. Measurement is acquired using efficient frame lengths and ensuring adequate counting statistics for dose rate derivation. Measurement length can range from days to more than one month.
5. Cluster analysis of the acquired frames is performed and measurement frames are integrated into one hitmap.
6. Beta particles are selected and adjusted for background noise.
7. Pixels outside the sample area are excluded, using the ^{241}Am source delineation.
8. Edge correction is applied.
9. Pixels are binned into sub-millimeter regions to reduce the counting errors.
10. Spatially resolved beta particle dose rates are derived using the applicable calibration curve for K, U, and Th.

Chapter 6

Spatially resolved dose rates in sediment samples: application of method

6.1 Aim of this chapter

The aim of this chapter is to apply the developed Timepix methodology to determine dose rates in sediments. First we examine an artificial sample, followed by field samples from two cave sites of high archeological significance: Liang Bua in Flores, Indonesia and Denisova in southern Siberia, Russia.

6.2 Artificial sample

Spatially resolved sediment dose rates were first determined for an artificial sample with visible stratification of known radioactive and nonradioactive components.

6.2.1 Materials and methods

A micro-stratified sample was prepared as per Timepix sample preparation procedure (section 5.3.1), using 200–350 μm-diameter grains of quartz and biotite. The sample was chosen as a simplified representation of a real sediment sample,

with dose rates previously quantified using the beta counter. The sample is shown in figure 5.1b, where the dark layers correspond to the radioactive biotite, and the light layers to the non-radioactive quartz. The sample was measured on the Timepix for a period of 7 days.

6.2.2 Results

Spatially resolved count rates at 0.1 mm resolution (i.e., cumulative counts for 2x2 pixels) are shown on a 2D hit map in figure 6.1a, with the scale on the right corresponding to the number of counts per pixel cluster (c/p). The two sample components are clearly visible based on their count rates, plotted as the x-y centroids of the detected beta particles. The count rates of the biotite and quartz regions are in the range of 25-60 and 0-25 counts/pixel cluster, respectively.

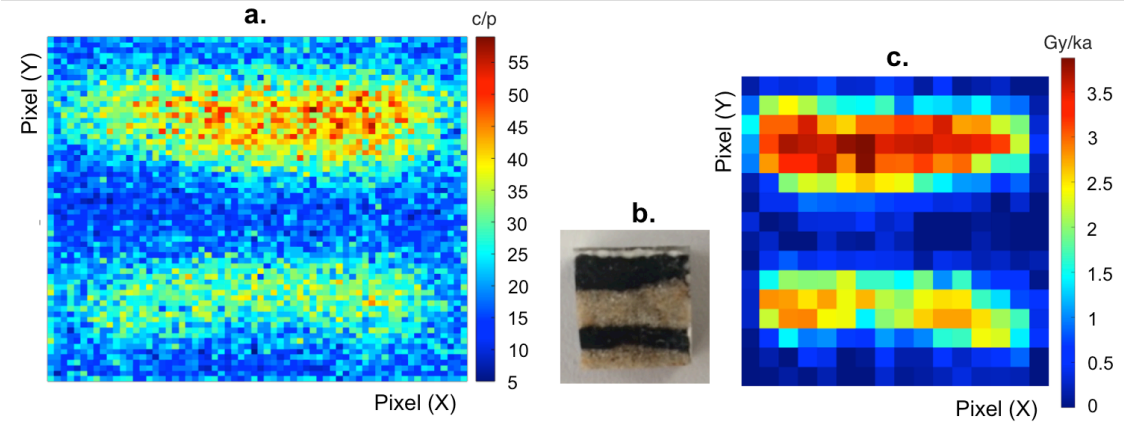

Figure 6.1 Artificial sample results: total number of counts per pixel cluster (a), photo of micro-stratified sample (b), derived dose rate distribution within the sample (c).

The corresponding spatially resolved dose rates in Gy/ka are shown in figure 6.1c at a resolution of 0.88 x 0.88 mm^2 (16x16 pixels). ^{40}K dose rates were determined using the absolute potassium calibration curve, and range between -0.16 and 3.57 Gy/ka. The dose rates attributed to the biotite regions of the sample range between 0.82 and 3.57 Gy/ka, whereas the dose rates in the quartz region are distributed

around a dose of 0.05 Gy/ka. The dose rates of the x and y pixel profiles are plotted in figure 5.2, where the x-profile corresponds only to quartz, and the y-profile captures both quartz and biotite, as shown in the figure 6.2 inset photo.

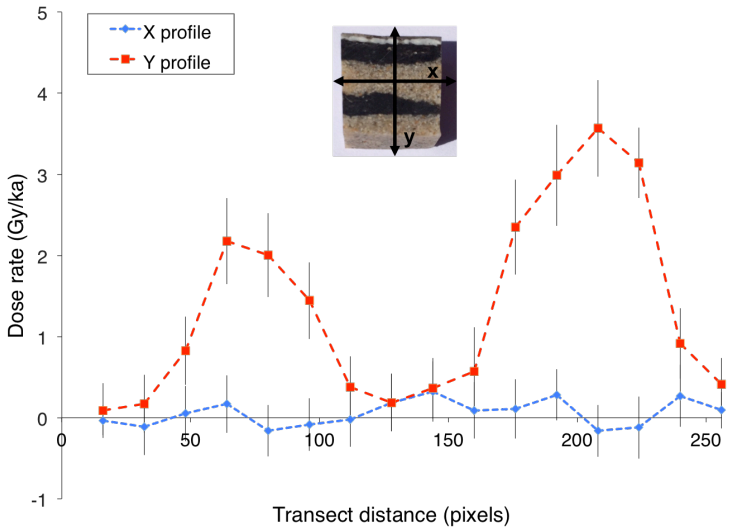

Figure 6.2 X and y dose rate profiles of the artificial sample. Error bars are shown at 1σ.

6.2.3 Discussion

Relative uncertainties (at 1σ) of 19.8 and 30.3% were determined for beta dose rates of 3.5 and 1 Gy/ka, respectively, at a spatial resolution of 0.77 mm^2, assuming 14 days of measurement time.

Because of Poisson statistics pertinent to Timepix count rates, some negative dose rate values resulted following background adjustment. Dose rates below 0 were found in regions of low count rates and are, therefore, considered to be statistically insignificant. This is further demonstrated by the error bars on the x-profile in figure 6.2, which show that negative dose values are consistent with statistical uncertainty. It is possible to eliminate negative dose rate values altogether, either by increasing measurement time or decreasing the spatial resolution.

6.2.4 Conclusion

A spatially resolved beta dose rate distribution has been determined for an artificial sample with a simplified ^{40}K distribution, utilizing the Timepix count rate measurement and dose rate conversion procedure outlined in chapter 5. The ability to quantify the beta-particle dose rate distribution using the proposed method has been demonstrated with sub-millimeter spatial resolution.

6.3 Samples from Liang Bua and Denisova Cave

Liang Bua and Denisova Cave are both sites where archaic hominins have been discovered in recent decades: the *Homo floresiensis* at Liang Bua, located on the eastern Indonesian island of Flores [72-74], and Denisovans and Neanderthals at Denisova Cave, located in the Altai Mountains of southern Siberia, Russia [4, 75, 76]. Robust dating methods are necessary to establish a reliable timeline for these archaic hominin populations and to gain further understanding on the possible interactions of these hominins with modern humans (*Homo sapiens*).

6.3.1 Materials and methods

The deposits in Liang Bua and Denisova Cave are characterized by variable compositions and textures, thus allowing a broad range of sample types to be measured on the Timepix. Liang Bua is located close to the equator in Indonesia and is characterized by a warm climate with chemical alterations of the sediment after deposition. Denisova Cave is situated in a colder region, the Altai Mountains in Russia, so the original sedimentary context is better preserved as the deposits have experienced fewer chemical modifications throughout the burial period.

A profile sample measuring 10 x 50 x 6 mm^3 was obtained from each of these sites and separated into five 10 x 10 x 6 mm^3 sub-samples to accommodate the Timepix detector. The Liang Bua sample was collected from Sector XXIV, straddling layers 8 and 9, and is composed of cave earth, limestone, manganese, and calcium carbonate.

The Denisova Cave sample was collected from the Main Chamber, straddling layers 21 and 20, and contains regions of limestone, fine-grained silts and clays, phosphate minerals, and fragments of bone.

Both sides of each 10 x 10 mm^2 surface were measured for 4-19 days per side, depending on sample activity. ^{40}K dose rates were determined using the ^{40}K absolute calibration function (equation 5.3). Example results of the multiple phases of data analysis are shown in figure 6.3: Liang Bua sample b (LB,b) is pictured in figure 6.3a; figure 6.3b displays the raw hitmap of the total count rate of the LB,b measurement, and figure 6.3c shows the resulting spatially resolved dose rates following the selection of the area occupied by the sample on the detector sensor and the conversion of count rate to environmental dose rate (Gy/ka). Figure 6.3c is the final spatially resolved distribution of beta dose rates within this sample after edge correction, which elevates the dose rates closer to the sample edge.

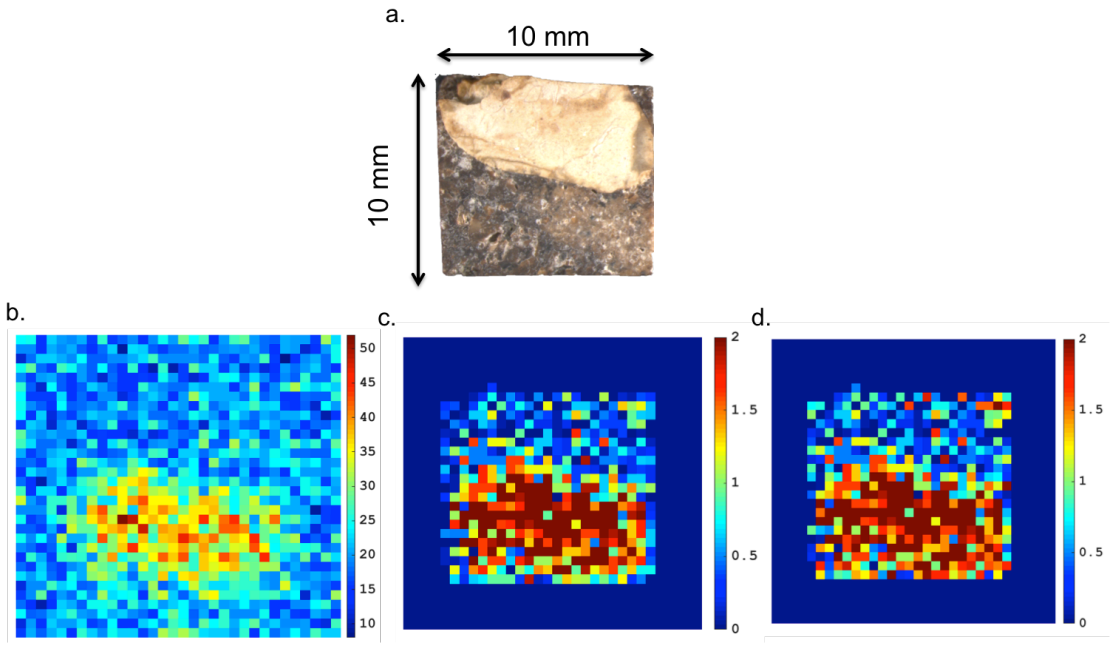

Figure 6.3 Data analysis process of Liang Bua sample b (LB,b) shown in (a): 2D count rate hitmap (total counts/pixel) (b), result after application of the dose rate calibration (Gy/ka) (c), and (d) result after application of the edge correction (Gy/ka).

6.3.2 Results and discussion

The Liang Bua and Denisova Cave sample profiles and their 2D dose rate maps, are shown in figures 6.4 and 6.5, respectively. In each of these figures, the first two columns on the left correspond to the front side of the sample, and the second two columns correspond to the back of the sample. In the Liang Bua profile, the beta dose rates range between 0 and 4 Gy/ka, with a mean value of 0.71 Gy/ka. In the Denisova Cave sample profile, the dose rate ranges between 0 and 5.4 Gy/ka, with a mean beta dose rate of 1.65 Gy/ka. The dose rate scale in both of the figures was chosen for optimal visualization of the beta dose rate distribution.

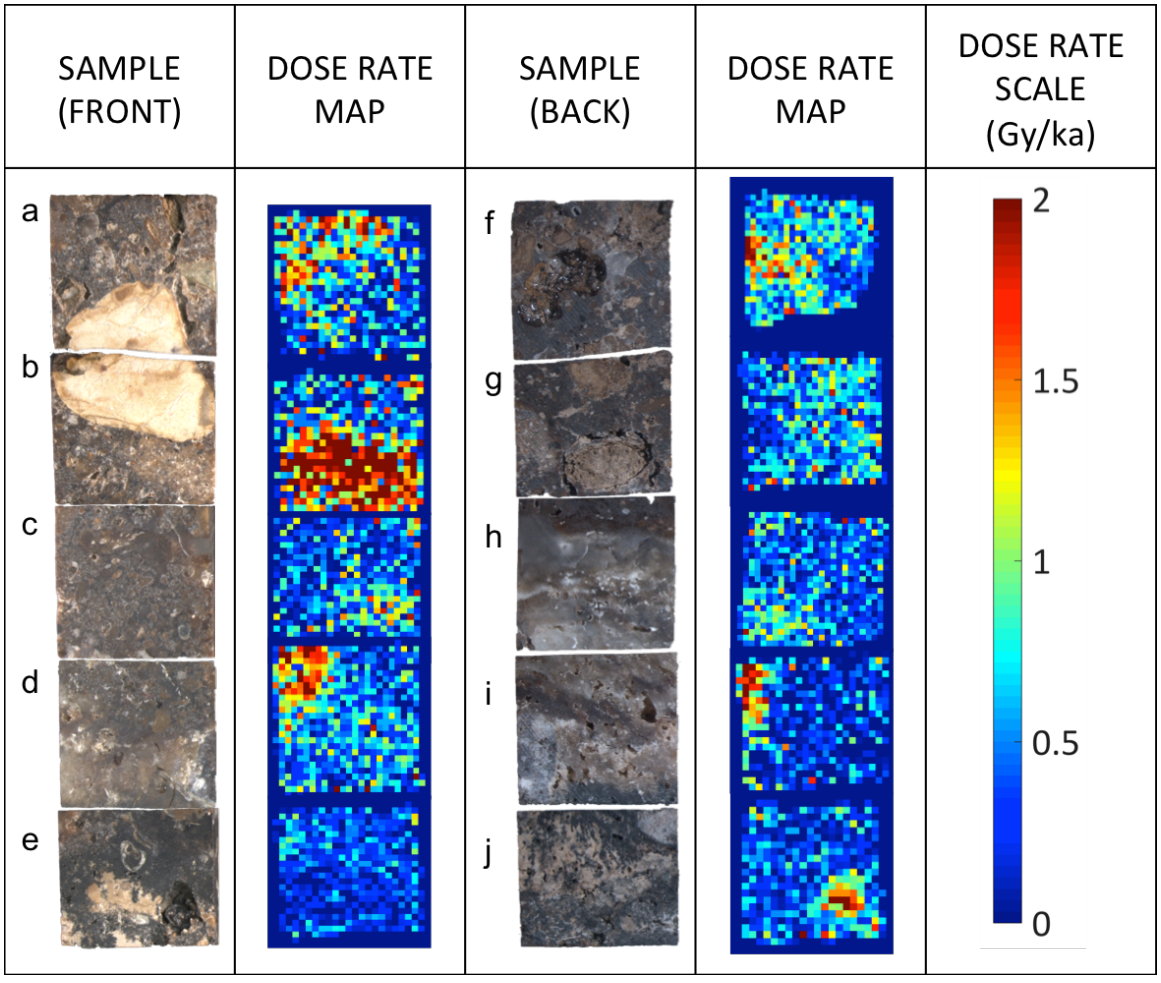

Figure 6.4 Spatially resolved beta dose rates in the Liang Bua sample profile. Each sub-sample is 10x10x6 mm^3 in size.

Although the range in dose rate of the two samples is relatively similar, the Denisova Cave profile has a mean dose rate 2.3 times higher than that of the Liang Bua sample. This difference can also be seen on the 2D dose rate hit maps of the two samples, where the Liang Bua samples contain radiation hotspots surrounded by non-active regions, whereas the Denisova Cave sediments have a more uniform radioactivity distribution. The results of both profile sample measurements demonstrate the variable extent of sample beta inhomogeneity and its relation to the specific architecture of the sample under investigation (e.g., presence of limestone clasts, bone fragments, etc.). The application of a mean dose rate for samples such as that from Denisova Cave may accurately represent the average for the bulk sediments, whereas for samples such as that from Liang Bua, which show greater spatial variability in beta dose rate, a more individualized approach should be considered.

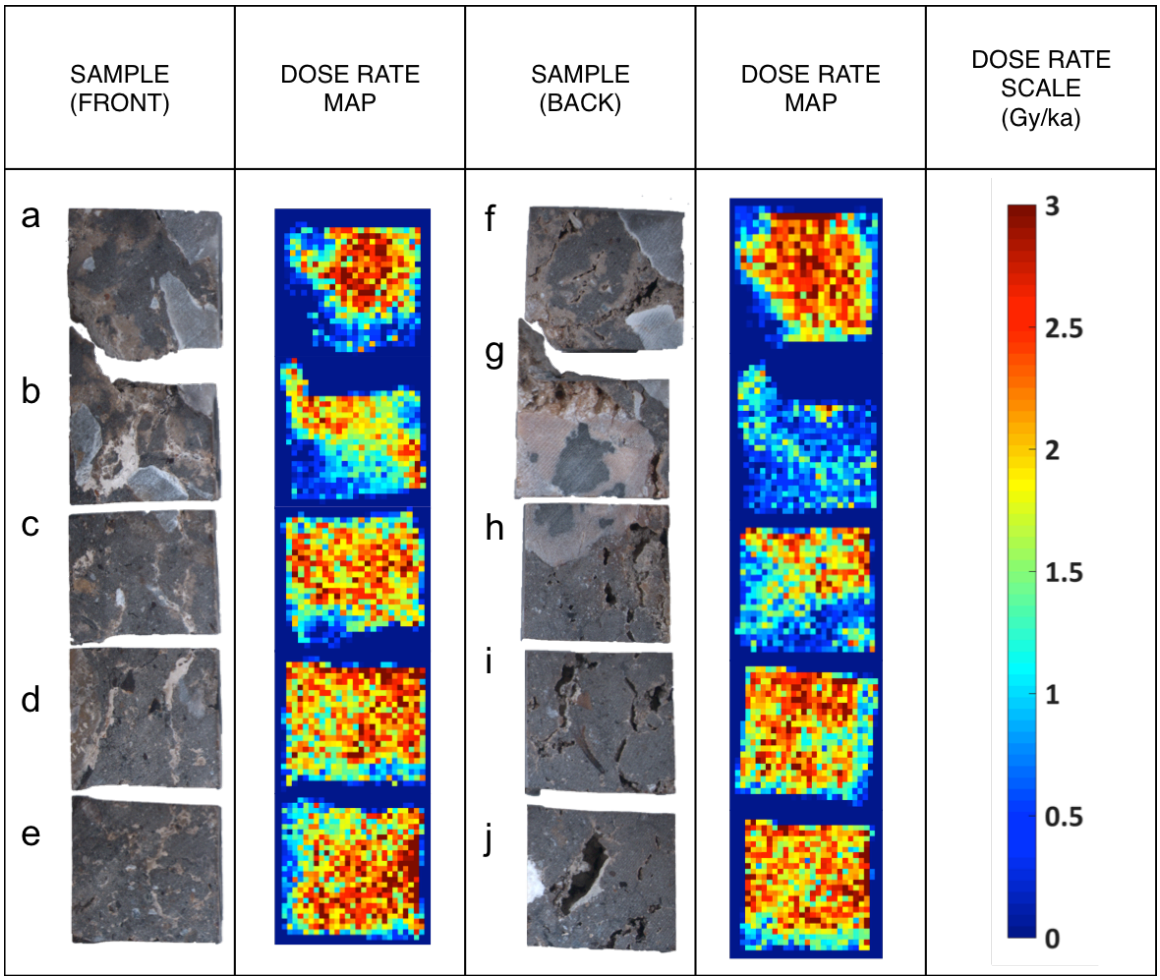

Figure 6.5 Spatially resolved dose rates in Denisova sample profile. Each sub-sample is 10x10x6 mm^3 in size.

Figure 6.6 illustrates sample dose rate inhomogeneity at the 0.44 x 0.44 mm^2 (8x8 pixels) spatial resolution in the form of a frequency plot, with Denisova Cave dose rates in red and Liang Bua dose rates in blue. The variability within each of the 50 x 10 x 3 mm^3 profiles is shown, with dose rates ranging from 0.1 to 4 Gy/ka and 0.1 to 5.4 Gy/ka for the Liang Bua and Denisova Cave samples, respectively. The frequency of dose rates above 4.8 Gy/ka in the Denisova Cave sample is so low that they are not visible on the plot. While the Denisova Cave sample dose rate distribution appears moderately Gaussian in shape, distributed around a value of 2 Gy/ka, the Liang Bua dose rate distribution is positively skewed towards dose rates of < 1 Gy/ka.

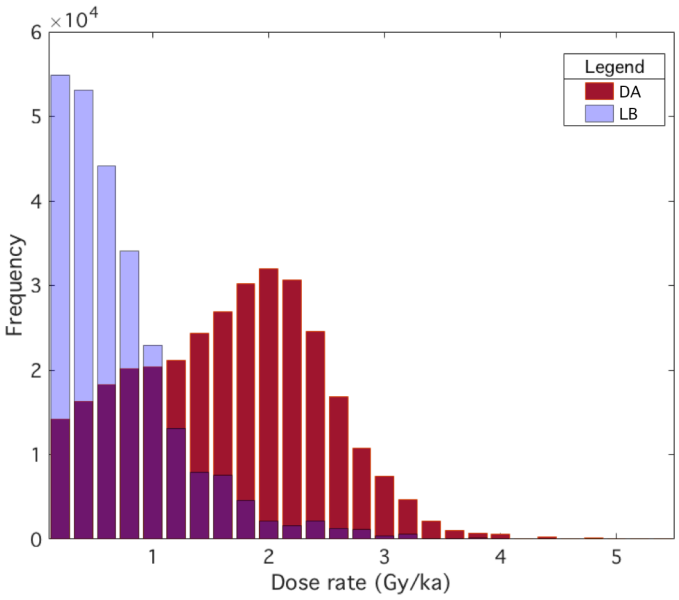

Figure 6.6 Frequency plot of the dose rate distribution within the Denisova Cave (DA) and Liang Bua (LB) samples (including 5 sub-samples, front and back).

The errors in the derived dose rates depend on the spatial resolution (i.e., the binning of the resulting single pixel data). Spatial resolution of 0.44 x 0.44 mm^2 (8x8 pixels, figures 6.4 and 6.5) results in a relative error of 27.7% for the mean dose rate of 0.71 Gy/ka in the Liang Bua sample, for a measurement time of 10 days. The relative error decreases to 14.1% and 7.5% for spatial resolutions of 0.77 (16x16 pixels) and 3.10 mm^2 (32x32 pixels), respectively. Radiation hotspots in the Liang Bua sample, shown in red on the dose rate heat maps in figure 6.4 and corresponding to dose rates of 2 Gy/ka and higher, have maximum relative errors of 16.7% and 5.0% for resolutions of 0.19 and 3.10 mm^2, respectively. In the Denisova Cave profile, the relative errors for the mean dose rate of 1.65 Gy/ka range from 18.3% to 5.3% for spatial resolutions of 0.19 to 3.10 mm^2, respectively. The radiation hotpots in the sample, capped at 3 Gy/ka in figure 6.5, have maximum relative errors of 13.7% and 4.4% for spatial resolutions of 0.19 (8x8 pixels) to 3.10 mm^2, respectively.

6.4 Discussion

All three calibration curves are based on the beta particle rate, which is the most relevant for dating due to its greater range in sediment and the removal by acid etching of the alpha dose rate component when dating sand-sized mineral grains. Since the Timepix detector is only able to provide the detection rate of the particle type, radionuclide identification is not possible at this stage. The elemental composition of the sample must be known or assumed to determine the sample environmental dose rate. In principle, it is possible to use the Timepix for isotope identification based on the detected particle energy, when the detector is used in the "time-over-threshold" mode, which is energy calibrated. This method can be investigated by distinguishing uranium and thorium radionuclides from potassium by means of their alpha particles, and then use respective alpha particle energies to identify the radionuclide. Other methods to determine elemental composition of the sample, such as laser-ablation ICP-MS or electron microprobe analysis in a scanning electron microscope, can also be applied.

The Denisova Cave and Liang Bua samples are known to have ^{40}K as the principal contributor to sample beta dose rate. When absorbed doses are quantified for single grains, it is important to consider the distribution of sources around the dosimeter grains, since it may have a significant effect on the sample age in some cases. In the case of the LB,b (figure 6.4), the mean dose rate of the 3 x 10^2 mm^3 sample would yield a ~40% difference in age to that determined using the mean dose rate of the entire 3 x 10^3 mm^3 Liang Bua sample profile. The apparent difference in age between a grain located at the bottom of LB,b, where there is a high concentration of ^{40}K, as compared to that of the top of the sample, where the dose rate is extremely low, is ~20%, both occurring within the 3 x 10^2 mm^3 volume of this sample.

The same analysis of the Denisova Cave sub-sample shown in panel 'e' (figure 6.5), in which the mean dose rate is higher than the average for the entire profile, results in a decrease of age by 70%, as compared to the age determined using the average

dose rate of 1.65 Gy/ka for the entire 3 x 10^3 mm^3 profile. The calculated age of grains located in the top left corner of this sub-sample, where ^{40}K is less concentrated, differs by ~40% from that estimated from the dose rates in the lower part of the sample.

These potential age differences highlight the need to make multiple single grain D_e measurements for age determination and to determine the beta dose rate from sediments collected at an appropriate spatial scale (i.e., at the same scale as the D_e values used for age determination).

6.5 Conclusion

^{40}K dose rates have been quantified for the Liang Bua and Denisova Cave samples, the error margin is 7.5% or less (at 1σ) at spatial resolutions of 3 mm^2, and 27.7% or less for spatial resolutions of 1 mm^2. Method weaknesses include the need for measurement times up to 10 days, as well as a sample size that does not exceed the area of the Timepix sensitive chip (14 x 14 mm^2).

A procedure for measuring and deriving dose rates for intact sediment samples using the Timepix pixelated detector has been developed and applied to samples collected from two key archeological and hominin sights. A calibration curve has been derived for ^{40}K and the uranium and thorium decay series, and spatially resolved Timepix beta particle count rates (measured in counts/pixel/second) can be converted into environmental dose rates at the desired spatial resolution using the determined count rate-to-dose rate relationships.

The proposed method is a novel application of the Timepix pixelated solid-state semiconductor detector. In doing so, this study represents a further step towards "grain-by-grain" dating of archeological and geological deposits, and a means of improving both the accuracy and the precision of luminescence age estimates.

Chapter 7

Part 2

Real-time dosimetry: rationale and dose calculation

Today cancer is the leading constituent of the disease burden in Australia: 1 in 4 women are diagnosed with cancer before the age of 75. Most commonly these are breast, colorectal, lung, and gynecological malignancies, the latter generally occurring in the endometrial lining and the cervix. In 2017 an estimated 2511 women had endometrial (i.e., uterine cancer), with a total of 494 deaths attributed to the disease. For cervical cancer the incidence and mortality were estimated at 813 and 223 persons, respectively [77].

7.1 Rationale

Radiotherapy (RT) is prescribed to approximately 50% of all cancer patients, and can be in the form of external beam or internal irradiation. Brachytherapy (BT) is an internal radiotherapy treatment that allows irradiation directly within, or in close proximity to the tumor target, and is a common treatment modality for patients

with gynecological malignancies. BT can achieve higher biological doses as compared to other RT modalities, but is limited to the sites that can be accessed internally. It is the most conformal form of RT, offering reductions in both side effects and post treatment toxicity, and thus can be used to treat patients who cannot handle more aggressive treatments. Prostate BT, for instance, has shown better prognostic features, as compared to EBRT and surgery [78]. EBRT patients show worse bowel, sexual, and hormonal scores, while radical prostatectomy patients show worse sexual summaries and urinary incontinence scores [79]. While BT treatment setup is more complex and time-consuming, its benefits often outweigh these shortcomings.

High dose rate brachytherapy (HDR BT) involves temporary implants and utilizes sources with energies exceeding 50 keV and dose rates of ≥20 cGy/min, namely ^{60}Co and ^{192}Ir. The dose gradient around HDR sources is ~10% per mm [80], and thus extreme care should be taken to ensure proper targeting. Over time HDR BT has become complex and hyperfractionation more frequent, increasing the risk of potential mistargeting, and elevating the role of treatment quality assurance.

7.2 Iridium-192 and remote afterloader

Iridium-192 is the nuclide of preference for temporary implants in HDR BT. The ^{192}Ir active core is encapsulated in stainless steel, giving the source rigidity and absorbing alpha and beta particles that are not used for treatment. The contribution of bremsstrahlung is also considered negligible. ^{192}Ir is a gamma emitter that decays via beta minus decay (95.1%) and electron capture (4.9%). The ^{192}Ir decay chain is shown in figure 7.1 (based on ICRP Publication 38, 1983). For every beta minus and electron capture decay ~ 2.2 photons with an average energy of 361 keV, and 0.1 photons with an average energy of 252 keV, respectively, are emitted [81]. Since the

half-life of ^{192}Ir is 73.81 days, the source must be changed at an interval of three to four months.

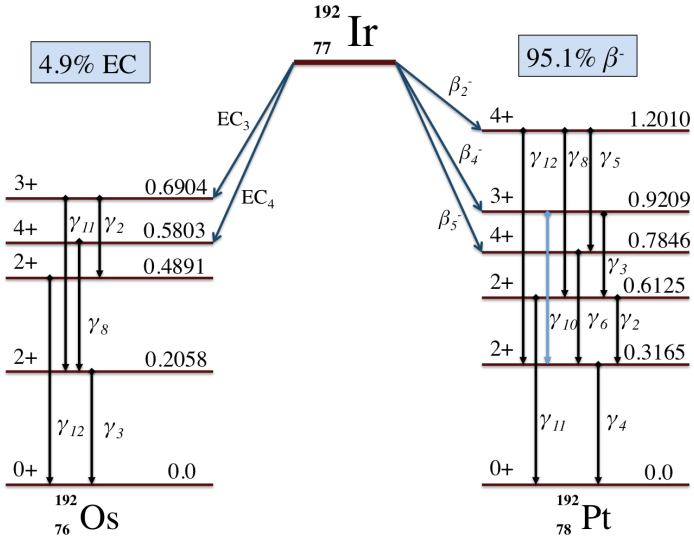

Figure 7.1 Decay chain of ^{192}Ir.

The HDR source is delivered using a remote afterloading device, that contains a tungsten safe for source storage. The afterloader has two motor and control systems: one for the HDR source, and one for the check source. The check source is a non-radioactive cylinder, analogous in shape and size to the HDR source, and is used to ensure transfer tube and catheter functionality prior to the release of the source into the patient. The Flexitron afterloading device is shown in figure 7.2 without the lid (7.2a), showing the tungsten safe and the drum containing the check source, and with the lid (7.2b).

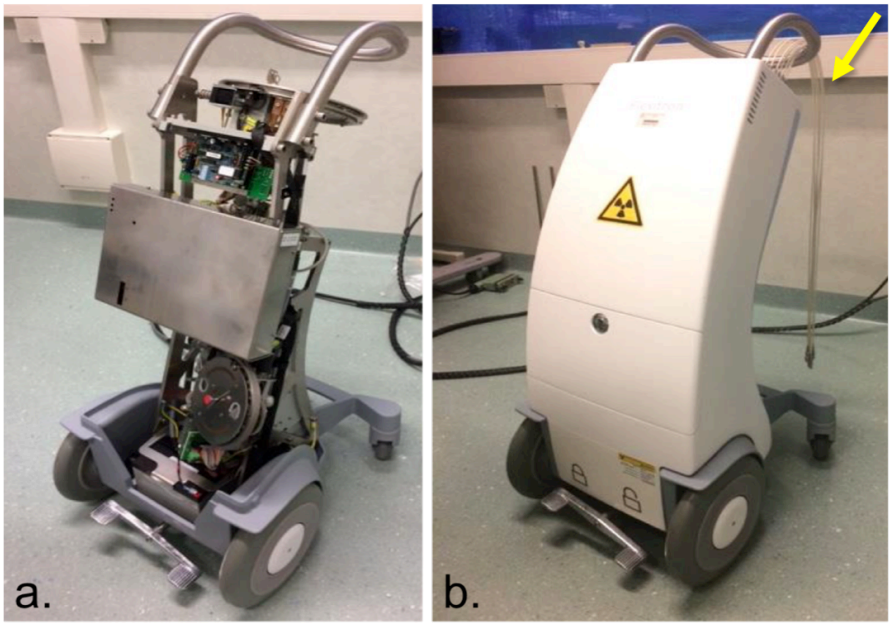

Figure 7.2 Flexitron afterloading device with the lid (a) and without (b). Yellow arrow in (b) points to the transfer cables that are connected to channels on the drum, and then to the BT applicator channels inside the patient, and used as the pathway for the HDR source.

Both of the sources are attached to steel wires that are wrapped around two drums inside the afterloader. Stepping motors rotate each drum to allow the source to enter its designated cable that corresponds to specific channels inside the applicator. The microprocessor receives information on the required channels using an encoder, and positions the source by monitoring the movement of the stepper motor.

7.3 BT dose calculation

Dose calculation algorithms used in BT treatment planning are based on the TG-43 [82] and the updated TG43-U1 formalism [83]. They are based on a combination of TLD measurements in water and MC simulations, and account for the ^{192}Ir source design. The dose to point P (figure 7.3) is calculated to account for its surrounding

geometry, and the dose to water is quantified using a number of parameters described below.

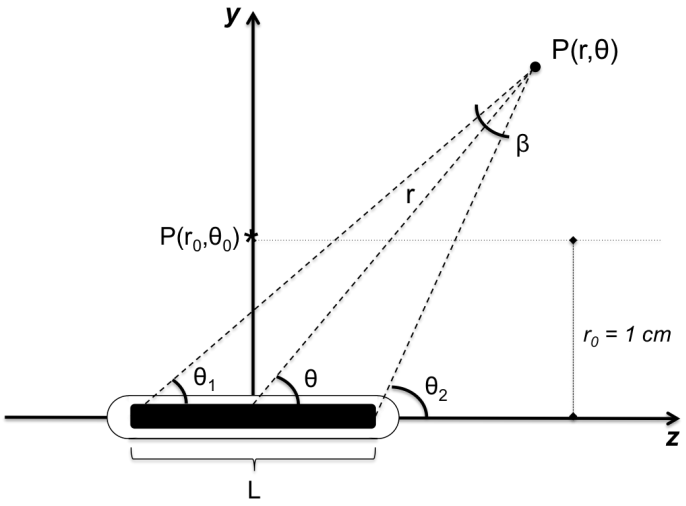

Figure 7.3 Reproduced geometry of the AAPM TG-43 dose calculation to point P [83].

In the line source approximation the dose rate in a water medium at point P, located at radial distance *r* and polar angle θ from the source, is calculated as follows:

$$\dot{D}(r,\theta) = S_K * \Lambda * \frac{G_L(r,\theta)}{G_L(r_0,\theta_0)} * g_L(r) * F(r,\theta) \tag{7.1}$$

S_K is the air-kerma strength (unit of measurement: 1 U = 1 cGy.cm^2.h^{-1}) that is numerically equal to the reference air-kerma rate (unit of measurement: 1 cGy.h^{-1}). Reference air-kerma rate ($\dot{K}_{\text{ref}}$) is the in-air kerma rate to air at the 1 m reference distance r_0. The two quantities are related by the following formula:

$$S_K = \dot{K}_{\text{ref}} \cdot r_0^2 \tag{7.2}$$

$\dot{K}_\delta(d)$ is the air-kerma rate in vacuum for photons above an energy of δ (in HDR BT, δ=10 keV), and thus accounts for attenuation and scattering in any mediums between the source and detector, as well as scattering from the floor, walls, and ceilings of the facility. Distance d is on the transverse plane of the source, from the

center of the source to the point of the specified $\dot{K}_\delta(d)$, and is large enough that any variation in S_K from source geometry is eliminated. Usually it is specified at a distance of 1 meter:

$$S_K = \dot{K}_\delta(d)d^2 \tag{7.3}$$

Λ is the dose rate constant in water, determined as the ratio of the dose rate at the reference position and the air-kerma strength:

$$\Lambda = \frac{\dot{D}(r_0, \theta_0)}{S_K} \tag{7.4}$$

G_L is the geometry function, where θ is the angle of P with respect to the source center, β is the angle subtended by both ends of the source (in radians), L is the active length of the source, and r is the distance from P to the source center. For the ^{192}Ir line source:

$$G_L(r, \theta) = \frac{\beta}{L * r * sin\theta} \tag{7.5}$$

(if θ≠0) and

$$G_L(r, \theta) = (r^2 - {}^{L^2}/_4)^{-1} \tag{7.6}$$

if θ=0.

$g(r)$ is the radial dose function, which equals to 1 at r_0 = 1 cm, and is used to adjust for any reduction in dose from attenuation and scattering on the transverse plane, that is not already accounted for by the geometry function:

$$g_L(r) = \frac{\dot{D}(r, \theta_0) * G_L(r_0, \theta_0)}{\dot{D}(r_0, \theta_0) * G_L(r, \theta_0} \tag{7.7}$$

$F(r, \theta)$ is the anisotropy function that accounts for any dose variation with respect to the polar angle, considering the scattering and absorption of photons resulting from the source encapsulation, and potentially also the cable to which the source is attached (it is equal to 1 on the transverse plane):

$$F(r, \theta) = \frac{\dot{D}(r, \theta) * G_L(r, \theta_0)}{\dot{D}(r, \theta_0) * G_L(r, \theta)} \tag{7.8}$$

7.4 Gynecological HDR BT treatments

HDR BT is prescribed to patients with cervical, endometrial, and vaginal cancers, often in combination with EBRT, chemotherapy, and/or surgery, according to disease progression. It can be used as a monotherapy in low-risk cases, and as a boost following hysterectomy to eliminate any residual disease from endometrial cancer. The source can be administered to the cervix and vaginal cuff using interstitial needles and intracavitary applicators. Interstitial treatments allow superior targeting when the gross tumor volume (GTV) is clearly visible, whereas standard applicators are more suitable in cases where a more uniform dose distribution (e.g., for simpler tumor geometry) is required. The applicator is selected based on target volume geometry, positioning of the organs-at-risk (OARs), and pathological conditions [80]. Treatment targets including the uterus, cervix and vaginal wall are densely vascularized and exhibit high radiation tolerance, but exist in close proximity to radiosensitive OARs, namely the bladder, rectum, and sigmoid. Patient geometry is shown on an MR image in figure 7.4 with OAR contours of the bladder in blue, sigmoid in turquoise, and rectum in pink, as well as the high-risk clinical target volume (HR-CTV) and GTV contoured in red and green, respectively.

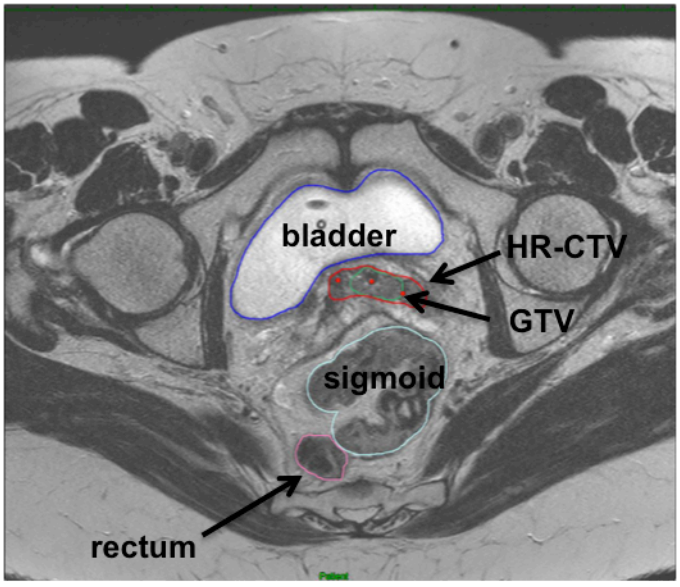

Figure 7.4 MR image of patient geometry with HR-CTV (red), GTV (green), and OAR contours (bladder in blue, sigmoid in turquoise, rectum in pink).

The patient undergoes a clinical evaluation following diagnosis, and the treatment goal is defined (i.e., whether it is local tumor control, palliative or curative treatment). Treatments normally consist of 3-7 fractions, and an approximate outline of the treatment flow is presented below (Erickson, Demanes et al. 2011.):

1. **Applicator implantation.**

   Applicator implantation is carried out by the radiation oncologist, with the aid of nurses and radiotherapy technicians, with or without anesthesia.

2. **Image acquisition (normally with CT or MR) for visualization of the applicator with respect to patient geometry.**

   The most common imaging modalities employed in the planning stage of the treatment are computed tomography (CT) and magnetic resonance (MR) [84]. The cylindrical multichannel applicator and surrounding tissues are shown both on CT (a,b) and MR (c,d) images of a gynecological patient plan in figure 7.5. The arrows in the axial images (7.5a,c) demonstrate superior soft tissue visualization provided by the MR image (7.5c), while the arrows on the sagittal images (7.5b,d) demonstrate the superior applicator visualization on the CT (7.5b). While MR minimizes artifacts arising from high-Z materials (that may be present in the gynecological applicator) and offers high-resolution tissue visibility, CT supersedes in its ability to visualize the applicator, and improves the accuracy of applicator reconstruction [85].

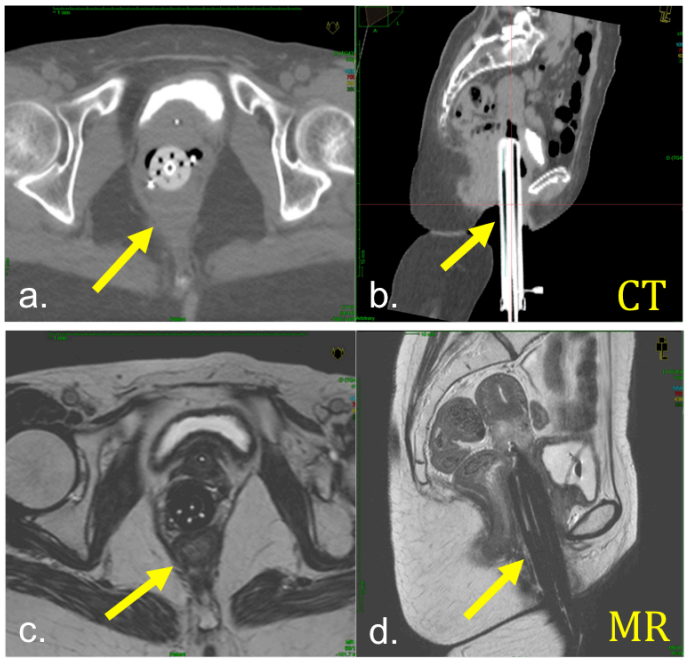

Figure 7.5 CT (top) and MR (bottom) images of the cylindrical applicator and surrounding tissues for a gynecological patient.

3. **Treatment planning using designated Treatment Planning Software and CT/MR images to reconstruct the applicator, contour target volumes and OARs, and optimize dose distributions.**

The target is defined based on the location and type of disease, treatment course (i.e., number of fractions and concomitant EBRT/chemotherapy/surgery), and the goal of the treatment. The GTV encompasses the visible tumor, and the CTV includes the GTV and an additional safety margin [86]. For treatments of the vaginal cuff, the dose is most often prescribed to a volume located at a distance of 5 mm from the surface of the applicator, with the vaginal wall as the treatment target. OAR and target dose distributions are verified on the Dose Volume Histogram (DVH). An example of a patient treatment plan prescribing 500 cGy for a total of 5 fractions is shown in figure 7.6. Isodose lines correspond to 150, 100, 90 and 50% of the prescribed dose in the turquoise, red, yellow, and green regions, respectively. Dwell positions in the central channel and one peripheral channel are denoted by the red spheres, and OARs visible on the image include the rectum (pink) and the bladder (blue).

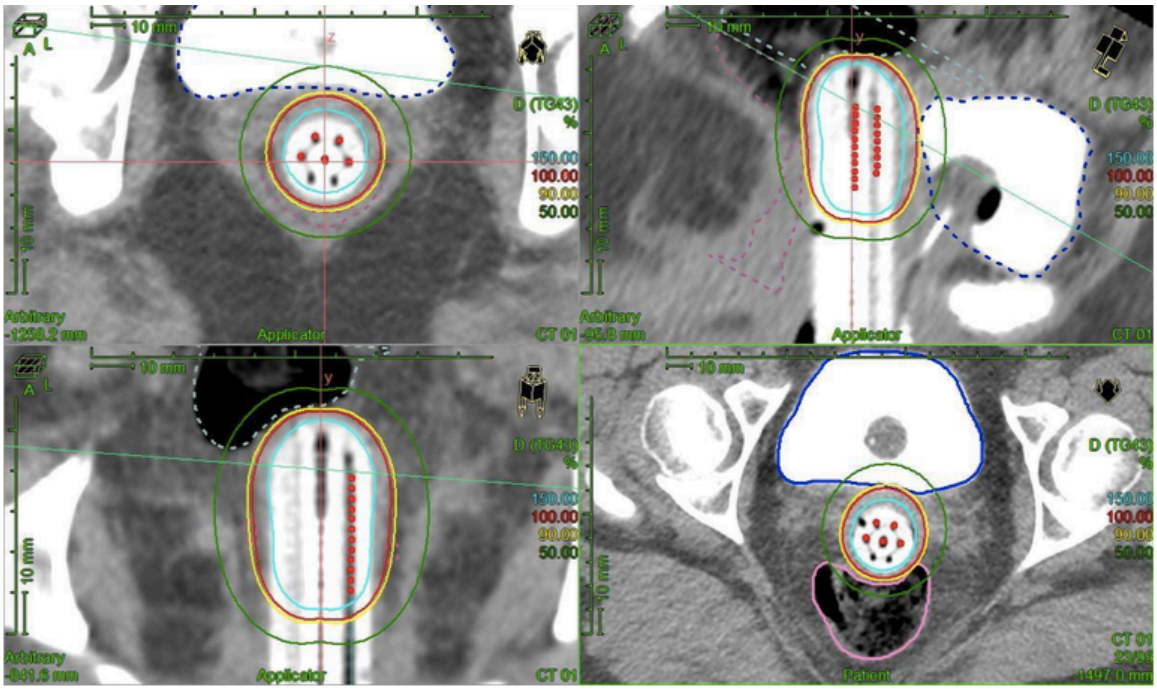

Figure 7.6 CT treatment plan with isodose contours (150% of the prescribed dose is shown in turquoise, 100% in red, 90% in yellow, and 50% in green) around the cylindrical applicator. Dwell positions are shown by the red spheres.

4. **Treatment dose delivery.**

   Transfer tubes are connected to the afterloader and their respective channels in the applicator. Throughout dose delivery hospital staff monitor the patient outside the BT bunker via an in-suite camera. Treatments usually last 5-15 minutes in length.

7.4.1 Quality assurance in HDR BT

A comprehensive quality assurance (QA) program provides verification against possible treatment discrepancies (as a result of equipment and human error) at all stages of the treatment, and thus ensuring the safety of patients, staff, and any other affected persons. Each treatment consists of multiple steps and involves various staff members along the way (summarized above).

The arrival of new equipment at a clinical facility begins with acceptance testing of the TPS, afterloader, source, and applicator. Acceptance testing for the HDR source includes the verification of source identity, air-kerma strength, physical dimensions and properties; for the applicator it includes the verification of the ability to deliver the source to the intended positions and the evaluation of the applicator shielding effect; for the TPS it includes the validation of system functionality using manual calculations, checks for constancy, and testing using standardized plans. Subsequently, a series of quarterly and daily checks take place, such as system prompts for date/time and sound verification; shielding and exposure monitoring; and specific procedures for source localization and temporal accuracy (usually carried out upon source replacement).

The remote afterloader system has built-in quality assurance checks that ensure applicator and source functionality in the pre-treatment stage. The afterloader verifies catheter length and confirms that no blockages are present in the catheters and transfer tubes using the nonradioactive dummy source. In the event of a blockage the source is automatically retracted. An emergency stop motor inside the afterloader is also able to retract the source upon the detection of unacceptable source stepping discrepancies, or in the case that the source fails to return to the tungsten safe. A reference point determined by the optopair inside the afterloader is used to detect when the source passes between the safe and the channel selection tube. Step size is verified by the microprocessor, with an error margin for variations due to friction. The afterloader contains a primary and secondary timer for dwell time verification. The primary timer calculates the total dwell time of all selected positions, while the secondary timer verifies that this total dwell time is within ±1% of the of the sum of the dwell times per channel and twice the time that the source is in transit [87].

A check ruler is installed with Flexitron afterloaders in particular, and used to verify source position and dwell time within ±2 mm and ±2%, respectively, accounting for the transit dose. A QA check is carried out using the in-suite camera and stopwatch.

During this check source position and dwell time are crosschecked to be within 1 mm and 1%, respectively of that indicated by the Treatment Console. Transit dose and the possible rounding error that may arise during the transfer of the plan from the TPS to the afterloader, are included in the error margin.

7.4.2 Errors in BT

A number of RT accidents occurred in the past despite the exhaustive pre-treatment QA process [88-91]. Errors may occur during and before dose delivery — for example in the planning phase with multiple specialists failing to detect a systematic error [92]. Errors reported for HDR BT include the delivery of the wrong patient plan, afterloader malfunction, indication of incorrect activity units, and source staying inside the patient following treatment completion [93]. The consequences can be as grave as death, and extend outside the treatment facility (e.g., radiation exposure of bystanders). The frequency of BT errors is not thoroughly covered in literature; the occurrence of transfer tube misconnections and patient organ and applicator motion are often not known altogether. Errors are rare, but nevertheless unavoidable, and may be consequential due to the high doses delivered per fraction. Both over- and under- dosing the treatment area is undesirable, since lower doses will result in an insufficient coverage of the tumor, whereas higher doses may cause toxicity in the form of acute and late effects of radiation.

Treatment errors may be the result of mechanical events, such as malfunctions of equipment, and human error, in one or more of the treatment phases. Potential errors in manual procedures could take place during data entry (e.g., source strength, step size, dose prescription, isodose value, and transfer tube, applicator and indexer lengths); applicator insertion and reconstruction during treatment planning and target contouring, especially in cases when the GTV is not clearly visible; misconnection of transfer tubes between the afterloader and the applicator; and general procedures (e.g., medical indication, patient identification, site of treatment, prescription, and diagnosis) [94]. Additionally, post-imaging changes in patient anatomy and applicator shifts may affect the dose distribution.

Two potential errors that may take place in BT treatments are positional shifts of the applicator and the interchange of transfer tube connections. Both of these errors can alter the delivered dose distribution within the treatment region. An example of a ~4 mm multichannel applicator shift in the para-sagittal plane is shown in figure 7.7, with the correct applicator positioning shown on the top images (7.7a,b) and the implications of a modification in the applicator position shown on the bottom images (7.7c,d). The yellow arrows in the figure point to the isodose contours in the correct and shifted applicator positions. As a result of implant modification, the dose distribution to the target also shifts in the same plane, and the target is no longer encompassed by the intended 350-cGy dose in the para-sagittal plane (7.7b,d), and the 400-cGy dose in the para-transveral (7.7a,c) plane. The applicator shift also increases the dose to the rectal wall.

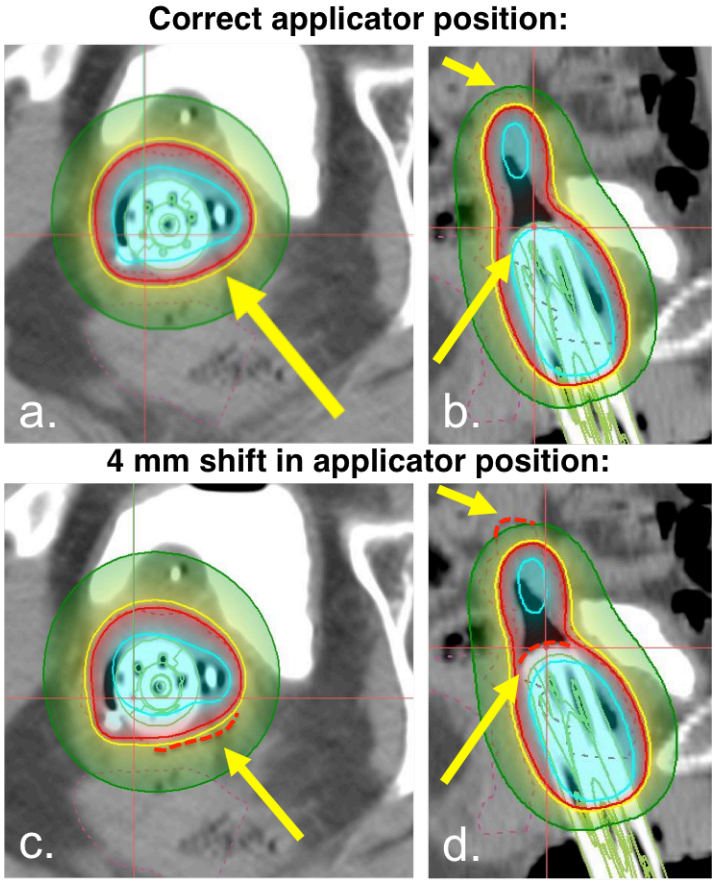

Figure 7.7 Para-transversal (a,c) and para-sagittal (b,d) views demonstrating the effect of a ~4 mm shift in the cylindrical applicator position inside the patient. The yellow arrows point to the isodose contours in the correct and shifted applicator positions.

The possible implications of a transfer tube misconnection, resulting in dose delivery to the wrong channel inside the applicator, are shown in figure 7.8. The arrows on the patient CT point to the two regions that will be affected by the switched transfer tube connections. In this example, if the source dwells in channel 7 (7.8b) instead of the planned channel 3 (7.8a), the 2-cc volume of the rectum will receive 6% more dose, whereas the target will be under-dosed.

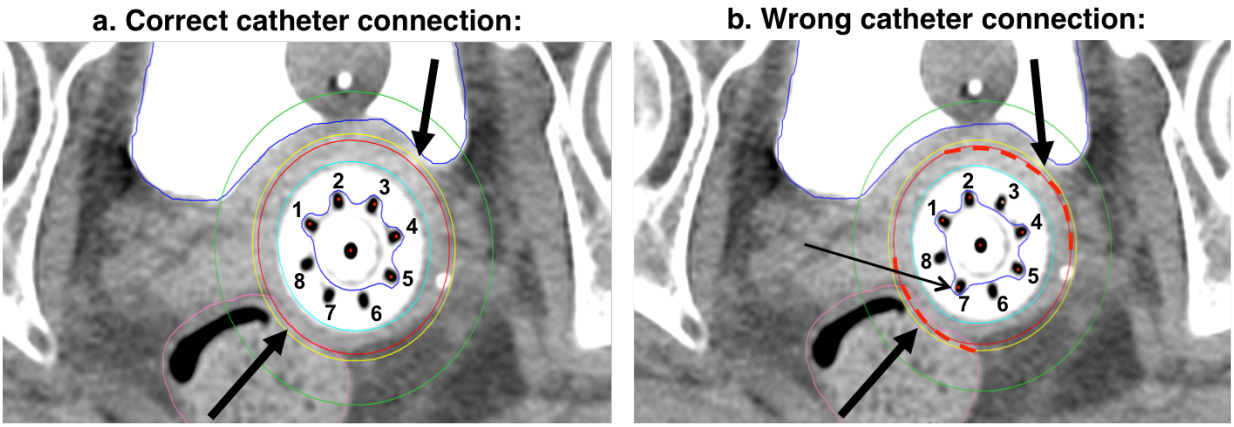

Figure 7.8 Possible implications of a transfer tube misconnection shown on a patient plan: instead of channel 3, channel 7 is connected on (b).

Both of the described errors (figures 7.7 and 7.8) can occur easily, and can affect the outcome of the patient treatment. Moreover, unless the HDR BT treatment setup or dose delivery is verified in real-time or post-treatment, these errors remain unnoticed.

Moreover, most frequently errors do not occur due to equipment malfunctions, but rather, due to human error, arising from mistakes, inadequate knowledge, and miscommunication [13-16, 19]. The American Association of Physicists in Medicine (AAPM) recommends QA of the entire HDR BT treatment process, outlined in detail in AAPM TG-56 [95] and TG-59 reports [96]. The various QA procedures discussed in section 7.4.1 thoroughly cover the treatment process prior to the dose delivery phase. However no real-time or post-treatment quality assurance protocol exists to verify that the dose delivery was carried out as intended by the radiation oncologist.

7.5 Real-time treatment verification

Real-time treatment verification that is able to fill in the gaps of pre-treatment QA checks would increase the quality of cancer care for the patient. Such verification has the potential to ensure that the treatment has been delivered according to the treatment plan: the dose has been administered correctly to the tumor target, and that intended minimal exposure of the surrounding tissues has been ensured. Moreover, it contributes to the awareness of treatment errors, currently lacking in the BT community, by monitoring the occurrence types and rates of frequency.

Some of the most essential characteristics of real-time verification systems include the ability to identify HDR source position; accurately determine doses to the target and organs at risk; provide precise knowledge of dosimeter location, all the meanwhile allowing inherently low Type A statistical errors [97].

7.5.1 System requirements

Especially important concepts for dosimetry system evaluation are sensitivity and specificity. Sensitivity describes the system's ability to detect treatment errors, and is expressed as the fraction of 'true positives'. Specificity is expressed as the fraction of 'true negatives' (i.e., system ability to identify the absence of error). However, an increase in sensitivity results in a greater number of false positives, and thus lowers specificity.

Other prominent considerations in dosimeter suitability for real-time BT treatment verification include:

- Energy dependence
- Angular dependence
- Dose rate dependence
- Detector size (i.e., ability to incorporate the dosimeter into the existing treatment accessories)

- Practicality of the system: robustness, stability, simplicity, and ease of incorporation into existing treatment routine
- Online readout

7.5.2 Two approaches

Two approaches to real-time BT treatment verification exist: *in vivo* dosimetry (IVD) and the verification of HDR source positions and dwell times. IVD is the measurement of absorbed dose to the target or organs-at-risk. HDR source verification is the tracking of source positions and dwell times in the dose delivery phase, using imaging or radiation detectors. When applied in real-time, both of these methods allow the clinician to interrupt the treatment in case of error detection, and prevent potential under-dosing of the tumor target and over-dosing of the OARs.

Chapter 8

Real-time BT QA: *In vivo* dosimetry

The aim of *in vivo* dosimetry is to serve as an independent and accurate method of verification of the dose to the target or organs-at-risk during the dose delivery phase. It can be used as a tool to verify dose at specific points within the treatment region, and thus detect errors causing an impact on the absorbed dose.

8.1 *In vivo* dosimetry for treatment verification

Major national international organizations such as the International Atomic Energy Agency (IAEA), World Health Organization (WHO), International Commission on Radiological Protection (ICRP), American Association of Physicists in Medicine (AAPM) and European Society for Radiotherapy and Oncology (ESTRO) recommend the use of IVD for treatment verification, however, it has not been widely integrated into regular treatment flow, except in the case of external beam radiotherapy (EBRT) total body irradiation. This is due to a number of reasons that arise both from the logistical and technical aspects: cost ineffectiveness, complexity of use and laboriousness of existing systems, shortage of resources and inefficiency, and the absence of set decision criteria for dealing with detected discrepancies. Moreover, the value of IVD is under question, with systems lacking in their capability to detect

a sufficient number of relevant errors to justify efforts, and a wide belief that the pre-treatment QA checks provide enough confidence in the treatment. Therefore IVD methods must be further developed to achieve higher accuracy, practicality, and user-friendliness.

In addition to BT treatment errors discussed in section 7.4.2, uncertainties in the absorbed dose may occur as a consequence of TPS algorithm shortcomings, such as failure to account for appropriate scatter conditions and tissue inhomogeneity. The finite patient volume as opposed to the infinite medium used in dose calculation, interfaces between different densities (i.e., tissue-to-air), and shielding by the applicator [98] may change the dose to the target. Clinical dose distributions in the planned target volume (PTV) may be affected by up to a factor of 10, either under- or over-estimating the dose [99]. The presence of the applicator may also affect the dose, especially for the organs in proximity to the PTV (e.g., the bladder and rectal wall), and result in an overestimation of the reported OAR dose for toxicity assessments due to a lower-density interface, such as the skin surface of the patient in breast cancer treatments [100].

8.1.1 IVD systems

Passive dosimetry systems most prominently used for BT treatment verification are TLDs [101-105] and film [106, 107]. TLDs come in various forms (e.g., rods, chips, ribbons, powders) and are valued for their robustness and small size, long lifetime, dose linearity, flat energy dependence, capability of measuring dose to tissue, and dynamic range for both high and low energy sources [108]. TLDs show the least sensitivity dependence on detector position, with response varying by 10-15% over the 1-10 cm range with respect to ^{192}Ir [109]. However, TLDs have to be annealed, exhibit fading, and can be expensive. Film has been widespread due to its ease of use, 2D dose distribution mapping, and energy independence; however it requires multiple measurement corrections such as those addressing film darkening and non-uniformity [110]. The major drawback of the aforementioned techniques is that

detected errors cannot be addressed during the treatment, since they are recognized following treatment completion.

A number of real-time IVD systems have been studied that allow the treatment to be interrupted or terminated, in case of major dose discrepancies from the treatment plan. These include electronic portal imaging devices (EPIDs) [111-113], plastic scintillation detectors (PSDs) [114-117], optical fibers coupled to a small aluminum oxide crystal [118], diodes [119-122], and metal oxide semiconductor field effect transistors (MOSFETs) [123-126]. EPIDs are constructed according to amorphous silicon photodiode technology, and show dose rate independence, can be calibrated in terms of tissue dose; however they exhibit angular dependence, over-respond to low energy photons and have a response lag [113]. PSDs are able to measure tissue-equivalent dose as a function of the light emitted by the polymerized solvent that is transmitted via an optical fiber to a photodetector. These systems have a small sensitive volume, long lifetime, show dose linearity and energy independence, and can be read out with nanosecond precision. Their shortcomings include high background (i.e., stem signal and temperature dependence) when used in vivo [127, 128].

Diodes and MOSFETs are both semiconductor dosimeters. Diodes have a response that is dependent upon energy, dose rate, temperature, and angle of incidence, and are known to change in sensitivity with changing source-to-detector distance (SDD) due to the variation in photon spectra. However their strengths often outweigh the shortcomings due to characteristics such as high sensitivity, robustness, long lifetime, ability of online readout, and simplicity of use [128]. The MOSFET is a type of transistor used for amplifying or switching electronic signals, and MOSFET dosimetry systems measure dose as a function of the change in threshold voltage. They are small in size, capable of displaying dose to tissue upon readout, and do not exhibit temperature dependence once equilibrium has been reached for a range of temperatures between 15 and 40° C [129]. MOSFETs require angle, energy, and sensitivity corrections with accumulated dose, and have a limited lifetime. Both

diode and MOSFET systems can be used in real-time also in passive mode, giving them an additional advantage of performing IVD without the application of a bias.

It is often difficult to select the ideal dosimeter for surface dose measurement due to the dose build up and scattering resulting from treatment equipment and shielding. MOSFETs have been compared to TLDs in anatomical sites such as breast, neck, chest, back, and nose and were found to be in good agreement. MOSFETs showed advantages over TLDs due to simple calibration, maintenance and operation, and the possibility of immediate readout. TLDs proved to be more laborious due to annealing, dependence on environmental conditions, and inherent impurities [130].

8.1.2 MOSFET dosimetry

MOSFETs have been used for EBRT dose measurements in anatomical sites such as the nose [131], breast [132], chest [133] and pelvis by placing dosimeters on the skin layer of the desired site [134], as well as under acrylic masks for head and neck patients [130, 135]. IAEA Human Health Report No. 8 describes MOSFET use for EBRT treatment monitoring, mainly to check the entrance dose in similar anatomical sites as Ramani et al. (1997), including the pelvis, head and neck, breast, and others [136]. MOSFETs have also been successfully applied to eye dosimetry in pediatric cranial CT scans [137] and neuro-interventional procedures [138]. In prostate treatments MOSFETs have been placed on rectal balloons during EBRT [135]; on urinary catheters to monitor the dose to the urethra in low dose rate (LDR) BT implants [124, 139], and on ultrasound probes for rectal wall dosimetry in HDR BT [140].

A feasibility study placing sterilized MOSFET dosimeters (coupled to a position-sensor) in a urinary catheter has also been performed for gynecological HDR BT, and determined positional accuracies of 1 mm within a 1-10 cm SDD, concluding the potential to detect a 2-mm movement of the bladder [141]. The above studies have demonstrated the capability of MOSFET dosimetry systems in successful real-time *in vivo* treatment verification.

8.2 Aim of this chapter

This chapter addresses the IVD approach to gynecological HDR BT treatment verification using MOSFET-type MO*Skin* dosimeters. The primary aim was to develop, test, and apply a rectal wall IVD system in an in-phantom feasibility study, followed by the clinical application of the developed system to an in-patient study. The secondary aim was to investigate a method of simplified MO*Skin* calibration adjustment for IVD, and propose a post-IVD MO*Skin* quality control (QC) check utilizing a low-activity beta source.

The feasibility study has been published as Romanyukha, A.A., Carrara, M., et al., *Applications of MOSkin dosimeters for quality assurance in gynecological HDR brachytherapy: An in-phantom feasibility study*. Rad. Meas. (2016), http://dx.doi.org/10.1016/j.radmeas.2016.12.010.
The *in vivo* application of the method has been published as Carrara, M., Romanyukha A.A., et al., *Clinical application of MOSkin dosimeters to rectal wall in vivo dosimetry in gynecological HDR brachytherapy*. 41 Phys. Med. (2017): 5-12. 10.1016/j.ejmp.2017.05.003.
The MO*Skin* calibration adjustment study has been prepared for submission to Physica Medica Journal as Romanyukha, A.A., Carrara M., et al., *Defining a simplified method of MOSkin calibration for in vivo dosimetry in a clinical setting*.

8.3 MO*Skin* dosimeters

MO*Skin* dosimeters are MOSFET-type detectors originally developed for skin dose measurements at the Centre for Medical Radiation Physics (CMRP) in the University of Wollongong (UOW) to address some of the traditional MOSFET dosimeter shortcomings [142]. The detectors are four-terminal devices consisting of the source, gate, drain, and substrate (figure 8.1).

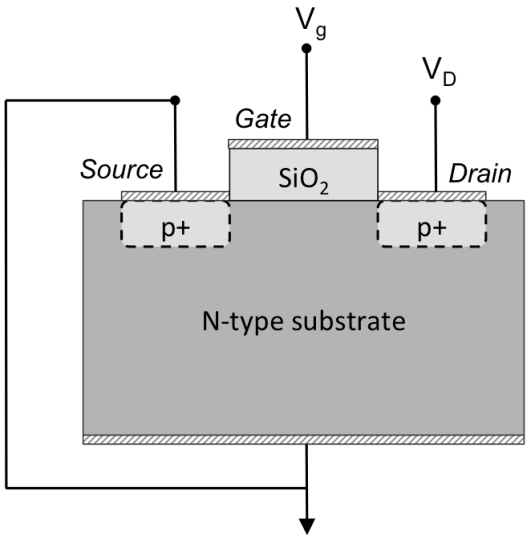

Figure 8.1 Schematic structure of the p-type MOSFET dosimeter.

The gate oxide (i.e., MO*Skin* sensitive volume) is made of a 4.8 x 10^{-6} mm^3 silicon oxide placed on silicon substrate (350 μm thickness). It limits dose-averaging effects arising from larger sensitive volumes, allowing optimal point measurements in high dose gradients. The threshold voltage V_{TH} is the voltage required for current to flow between the source and the drain, and the shift in V_{TH} (i.e., ΔV_{TH}) is proportional to the absorbed radiation in the gate of the MOSFET.

The silicon chip is assembled over a Kapton pigtail with the complete detector probe measuring 350 x 3 x 0.4 mm^3. In traditional MOSFET dosimeters the sensitive volume is protected by a bubble epoxy resin layer lacking reproducible thickness, making it unsuitable for skin dosimetry. However, MO*Skin* geometry contains a thin 0.07-mm water equivalent depth (WED) build-up layer of Kapton (shown in figure 8.2) that is achieved by special CMRP packaging technology of silicon sensors, making it ideal for dose measurements at the surface level.

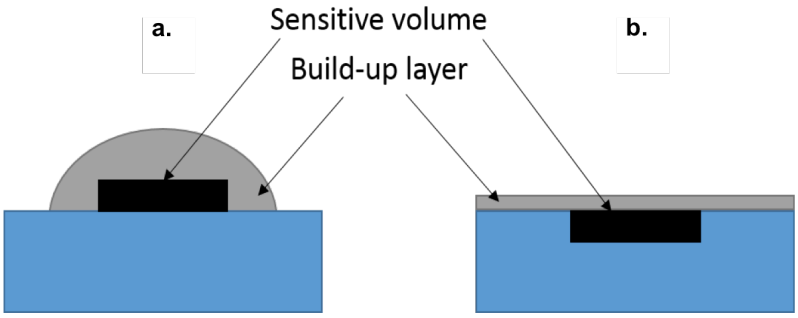

Figure 8.2 Traditional MOSFET geometry (a) with epoxy bubble for sensitive volume protection and MO*Skin* geometry (b) with a 0.07-mm Kapton build-up layer, allowing surface level dose measurements.

MO*Skin*, as a p-channel MOSFET, requires a positive bias on the gate during radiation exposure, causing charge separation: the electrons are pulled towards the gate, and the holes toward the interface between Si and SiO_2. Holes are captured into traps at the interface to form a positive charge layer. Threshold voltage changes a function of dose, as follows:

$$\Delta V_{TH} \sim 0.0022 \cdot D^{0.4} \cdot t^2_{ox} \quad \text{(passive mode)} \qquad (8.1)$$

$$\Delta V_{TH} \sim 0.04 \cdot D \cdot t^2_{ox} \cdot f \quad \text{(active mode)} \qquad (8.2)$$

where D: dose

t_{ox}: oxide thickness

f: fraction of holes escaping recombination

Dosimeter sensitivity is primarily determined by the oxide thickness and the electrical field. A higher bias during irradiation causes a larger proportion of charge collection, increasing the sensitivity of the device and reducing the total dose the device is able to record before saturation. The gate threshold is known to vary with temperature, and depends on the amount of radiation exposure the detector has received. Other shortcomings include angular dependence, finite shelf life, and dose fading.

The MO*Skin* readout system is the *Clinical Semiconductor Dosimetry System*, a dedicated microprocessor reader, which acquires and integrates the signal over the selected interval from up to five dosimeters at a time (figure 8.3). The readout interval can be set as low as 1 second. A bias of 0-15 V (established as thermostable during current-voltage detector characterization) can be applied on dosimeter gate during radiation exposure, and this way measurement sensitivity can be adjusted to accommodate the specific application. Accompanying *MosPlot* readout software was also developed at CMRP, allowing graphical and numerical representations of the instantaneous and total ΔV_{TH} shifts. Detector sensitivity factors obtained during calibration can be defined prior to measurement to display absorbed dose (cGy) in real-time.

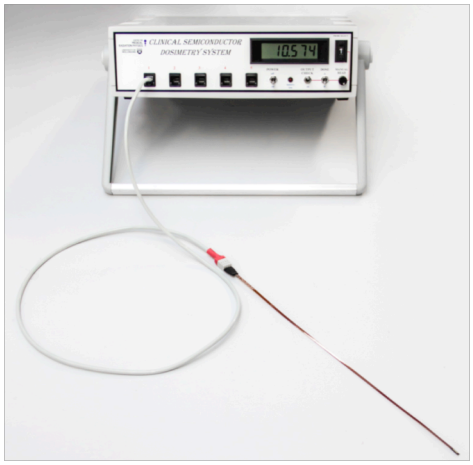

Figure 8.3 Clinical Semiconductor Dosimetry reader with one MO*Skin* detector connected.

Errors due to reader uncertainty for consecutive readings and the creep-up effect (i.e., charge arising from the measuring circuit) were quantified as ±1 mV and ≤4 mV, respectively, and together contribute to < 1% error, given that the integral dose is recorded following a 1-minute time interval. The fading effect (i.e., reduction of charge following radiation exposure) of MO*Skin*s is avoided if readout is recorded within 15 minutes of irradiation. Since the acquired data is automatically stored in a data file, the creep-up and fading effects, respectively, are accounted for by

recording the ΔV_{TH} once a plateau is reached (in the case of post-measurement data analysis).

The detectors have been optimized to measure dose in steep dose gradients, as those characteristic of HDR BT sources such as ^{192}Ir [143], and fully characterized in previous studies [144]. MO*Skin*s were found to accurately determine doses in steep dose gradients as well as at interfaces, correctly reproduce tissue scattering conditions, and allowing to determine the dose to tissue at the time of readout.

8.3.1 MO*Skin* calibration

8.3.1.1 INT HDR BT facility

The following studies took place at the Istituto Nazionale dei Tumori (INT) in Milan, Italy. The HDR BT facility was equipped with the microSelectron HDR remote afterloading device and Oncentra Brachytherapy TPS for treatment planning, both provided by Elekta (Nucletron Elekta, Veenendaal, Netherlands). The afterloading device allows up to 30 transfer tube connections, a positional accuracy of ± 1 mm, and a minimum step size of 2.5 mm. The lowest dwell time setting is 0.1 seconds. The active length of the ^{192}Ir source was 3.6 mm with an active diameter of 0.65 mm [87]. The source reference air-kerma rate was certified to be within 5% (k=3) by the vendor calibration certificate, and then verified at INT using a primary standards dosimetry lab-traceable well type ionization chamber of 200cc vented sensitive volume [145].

8.3.1.2 Calibration procedure

For calibration, each dosimeter is positioned in the center of a 100 x 100 x 100 mm^3 LR Plastic Water phantom slab (CIRS, Norfolk, VA). The plastic needle delivering ^{192}Ir was placed at a distance of 21 ± 0.1 mm from the center of the MO*Skin* sensitive volume, chosen in consideration of the predicted SDD for IVD in rectal wall dose measurements. An additional 100 x 100 x 100 mm^3 of scattering volume was added below the source to ensure adequate scattering conditions [100]. The calibration setup is shown in figure 8.4. Prior to each calibration, Oncentra was used to

determine the dwell time corresponding to a dose of 100 cGy at the selected distance using a CT scan of the calibration setup. The TPS-determined dwell time was crosschecked using an AAPM TG-43-based Matlab script for dose calculation.

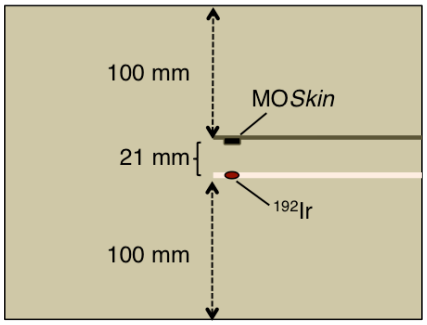

Figure 8.4 MO*Skin* calibration setup.

ΔV_{TH} readings M were taken at an interval of 5 seconds by applying a 15-V bias on the detector, ensuring response stability of the detector. The calibration coefficient N_S (cGy/mV) was determined as the quotient of the dose rate, calculated as the delivered dose (cGy) per dwell time (s), and the slope of the ΔV_{TH} shift per unit time (mV/s). Once the dosimeters have been calibrated the absorbed dose D was determined from M (measured in mV) as follows:

$$D = M \cdot N_s \tag{8.3}$$

An example of calibration curves for three dosimeters is shown in figure 8.5. In this case 100 cGy were delivered for a total source dwell time of 42.4 seconds. Linear fits were derived, serving as the calibration coefficient, and correspond to 2.53, 2.36 and 2.48 mV/cGy for the three dosimeters, respectively, with R^2-values of 0.999 in all cases.

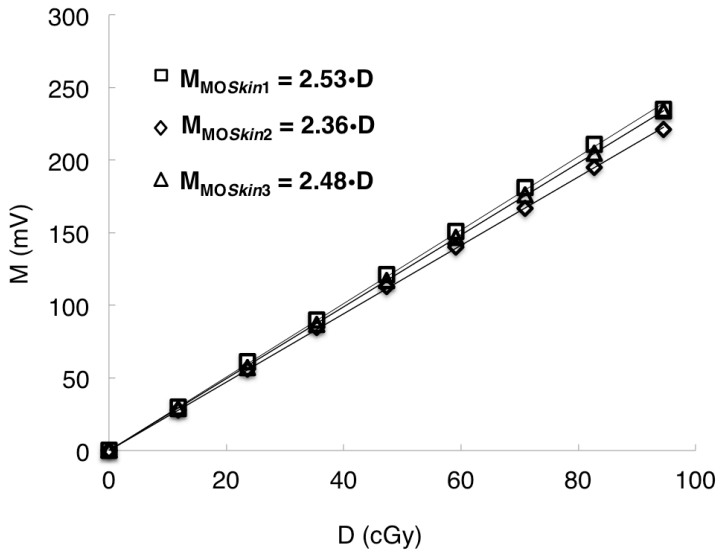

Figure 8.5 Example of calibration curves for three MO*Skin*s, with calibration coefficients of 2.53,2.36 and 2.48 cGy/mV determined for the three dosimeters, respectively.

8.4 Simplified method of MO*Skin* calibration adjustment

A change in MOSFET detector sensitivity is known to occur with radiation exposure. In order to ensure precise dosimetry, calibration coefficients obtained prior to radiation exposure must be adjusted throughout the lifespan of the detectors. The calibration adjustment is usually determined by repeating the calibration procedure, which can be time consuming and impractical due to the necessity of the BT facility, that is often occupied for patient treatments in the clinic. A simplified method of MO*Skin* sensitivity measurement, which can be carried out outside the BT bunker without demanding strict radioprotection requirements, would thus facilitate the calibration adjustment procedure.

8.4.1 MOSFET change in sensitivity

A number of studies have investigated this topic, and have come to a similar conclusion: precise dosimetry demands either recalibration or a shortened MOSFET lifetime [125, 135, 136, 140, 146-148]. The IAEA has recommended a recalibration

of MOSFET dosimeters following a total dose of approximately 23 Gy (i.e., 2/3 of the estimated detector lifetime) [136]. Ramani et al. (1997) avoided calibration adjustments by discontinuing MOSFET use at dosimeter accumulated threshold voltage of ≥18.5 V [130]. Haughey et al. (2011) found MOSFET dosimeters in a rectal wall IVD study unsuitable, citing the change in the response of the detector as one of the main reasons [125].

Fagerstrom et al. (2008) quantified the change in MOSFET (Dose Verification System, Sicel Technologies) sensitivity using third order polynomials [146], whereas Haughey et al. (2011) found a 1 ± 0.8% change per 0.5 V in the calibration of the dosimeters when testing them for gynecological and prostate IVD. Zilio et al. (2006) determined MOSFET reproducibility between 3.5 and 4.5% per V [148]. For MO*Skin*s in particular, Hardcastle et al. (2010) found measurements to be reproducible within 1% for doses up to 10 Gy, after which the dosimeter was discarded due to the nature of the rectal balloons used in the IVD study [135]. Recalibration has been recommended for MO*Skin*s at every 5 V of accumulated dose [147], which corresponds to a dose of ~22 Gy, or approximately four HDR BT fractions. In the prostate IVD study carried out by Carrara et al. (2016) the dosimeters were recalibrated after use in three HDR BT fractions, or following a cumulative dose of 15 Gy [140].

It is evident that the adjustment of initial dosimeter calibration is mandatory, and currently involves a replication of the initial calibration procedure described in section 8.3.1.2, involving the BT theater or linear accelerator bunker, in addition to the transport of the phantom to the relevant facility. Treatment rooms remain busy throughout the day in the clinic, and cannot be accessed for calibration purposes. Moreover, the phantom that ensures proper scattering conditions is heavy and difficult to transport.

8.4.2 Aim of this study

MOSFET dosimeters are known to be energy-dependent, and it has been noted previously that the accumulated dose effect is not linear between sources of varying energies, and thus cannot be adjusted for using a single correction factor [146]. The aim of this study was to investigate a method utilizing the ratio of dosimeter sensitivities to the RT and a low-activity source for MO*Skin* calibration adjustment, throughout its use in the clinic. The low dose rate-emitting ^{90}Sr source was used to adjust MO*Skin* calibration coefficients for absorbed dose measurement in EBRT beams of 6 and 15 MV, and the HDR BT ^{192}Ir source. The goal was to simplify MO*Skin* recalibration employing a source that does not require extensive radioprotection precautions, such as the shielding necessary for BT and EBRT treatments, is compact, and can be used inside an office or a laboratory.

Moreover, to provide confidence that the detector has functioned properly throughout measurement and has yielded reliable results, a method for MO*Skin* quality control following IVD is proposed utilizing the ^{90}Sr source.

8.4.3 Materials and Methods

Six brand new MO*Skin* dosimeters were selected for the study: three for use with ^{192}Ir, and three for measurement with the linear accelerator (linac) beams. MO*Skin* sensitivity ratios between ^{90}Sr and RT sources were calculated at three stages of detector lifetime, separated by 15 Gy of total accumulated dose. At each stage MO*Skin* response to ^{90}Sr was acquired first, followed by measurement with the RT source. MO*Skin* response ratios between ^{90}Sr and each RT source were determined and evaluated as a function of total detector accumulated dose.

8.4.3.1 The ^{90}Sr source

The ^{90}Sr source was selected due to its accessibility in the RT clinical environment. It is commonly used in the hospital as a check-source for Markus and Farmer chambers to verify their stability and determine correction factors for air density prior to use in EBRT QA practices [149]. The source (type T48012, PTW, Freiburg,

Germany) has a half-life of 28.7 years, an activity of 33 MBq, and decays by β− decay with beta energy of 0.546 MeV. Its decay scheme is shown in figure 8.6, and includes a 2.28 MeV β− decay from yttrium-90 ($T_{1/2}$ of 64.1 h) to the stable zirconium-90.

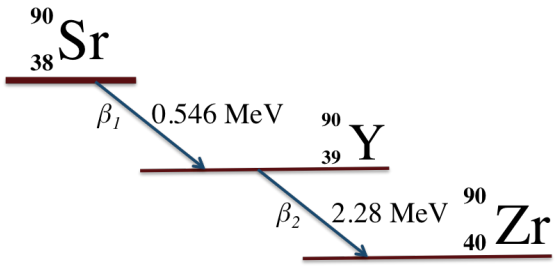

Figure 8.6 Decay scheme of ^{90}Sr.

The manufacturer reports a dose rate below 1 μSv/h at a distance of 10 cm from a closed-cover source [150]. The source is packaged inside a shielded container and is accompanied by a plastic holding device measuring 10 cm in diameter and 2 cm in depth. It consists of two precisely aligned top and bottom pieces, allowing the ^{90}Sr source to be fixed in place during measurement. Due to the long half-life of the source any change in activity during this two-week study was considered negligible.

8.4.3.2 MOSkin sensitivity measurements

The most widely used EBRT beams of 6 and 15 MV, respectively, were selected. Linac output was confirmed for each energy spectrum according to the IAEA TRS-398 protocol utilizing the Farmer ion chamber (NE2581). MO*Skin*s were positioned on top of a 100 mm-thick LR Plastic Water phantom for backscatter, with maximum buildup depths of 15 and 30 mm for beams of 6 and 15 MV, respectively. A dose of 1 Gy at a rate of 200 MU/minute was delivered at SSD of 100 cm, with ΔV_{TH} read out at a 5-second interval. Calibration coefficients N_{6MV} and N_{15MV} were calculated as described in section 8.3.1.2.

To quantify ^{90}Sr sensitivity, each MO*Skin* was placed directly below the open ^{90}Sr source inside the plastic holding device (figure 8.7a), centering the sensitive volume on the lower piece so that it directly faces the active part of the source (figure 8.7b).

Due to the thinness of the detector pigtail it was possible to align the two plastic pieces precisely and without gaps.

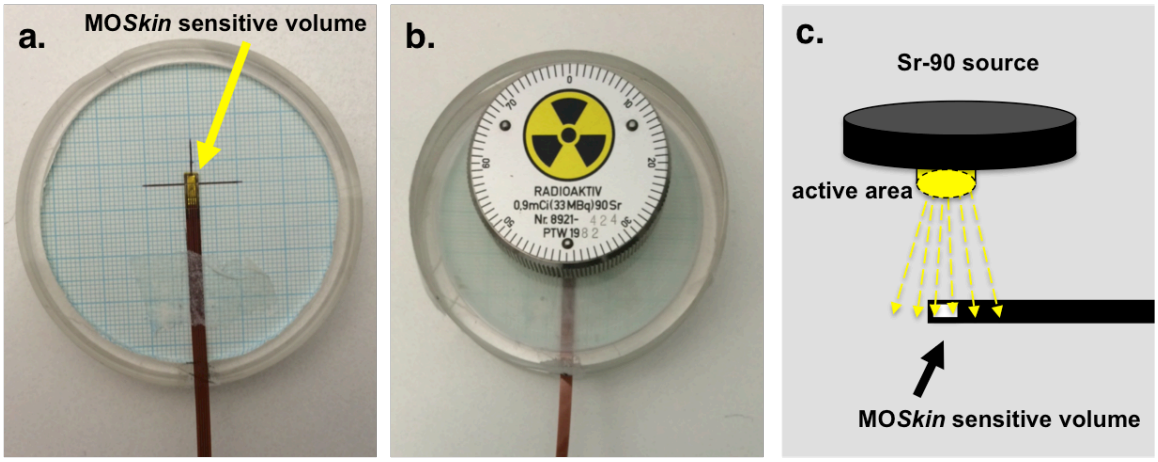

Figure 8.7 ^{90}Sr plastic holding device, consisting of a bottom (a) piece where the MO*Skin* was fixed, and a top piece (b) where the source was positioned. Irradiation geometry is shown in (c) with the source active area positioned directly above the MO*Skin* sensitive volume.

An integral dose of 15 Gy was delivered between sensitivity measurements (i.e., between stages 1 and 2, and stages 2 and 3, respectively), using the RT source, to simulate three stages of detector lifetime. MO*Skin* response to each source was acquired three times, delivering a total dose of 3 Gy at each stage. The dose delivered by ^{90}Sr could not be precisely quantified, but is estimated to be no more than 3 Gy throughout the entire experiment (i.e., when applying the 6 and 15 MV EBRT calibration coefficient). Total doses received by the dosimeters were 39 and 48 Gy in BT and EBRT experiments, respectively. A chronological schematic of the experiment is shown in figure 8.8.

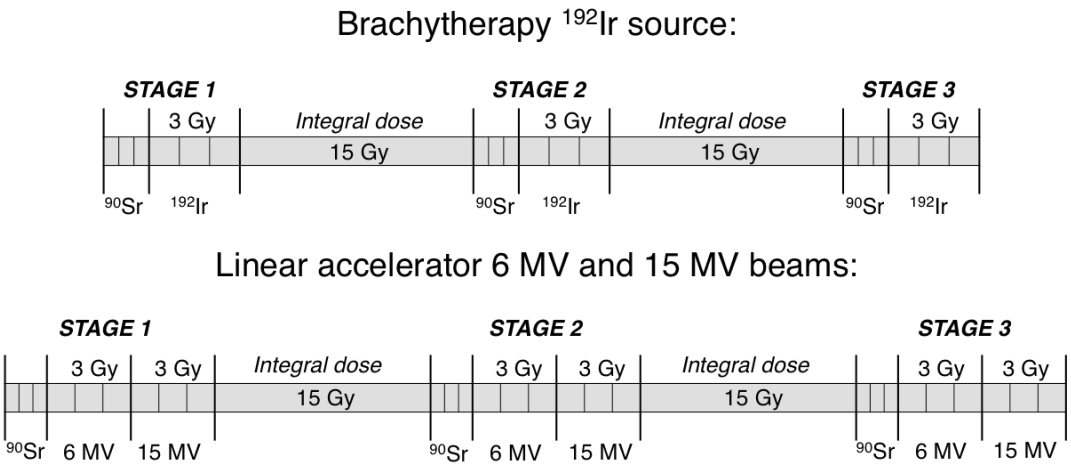

Figure 8.8 Schematic plan of MO*Skin* measurements throughout the experiment, where each section corresponds to the irradiation type, and each subsection corresponds to one irradiation.

For measurement of MO*Skin* sensitivity to ^{90}Sr, the detectors were positioned as shown in figure 8.7, and M readings were taken at a 15 second-interval, for a total of 120 s by applying 15 V to the gate of the MO*Skin* in each readout step. The relationship between the acquired ΔV_{TH} and time was evaluated by determining the slope of the linear fit of the measurement (mV/s). The mean linear fit of the three irradiations was determined, and its inverse (i.e., N_{Sr90}, s/mV) was used to describe MO*Skin* sensitivity to ^{90}Sr.

MO*Skin* sensitivity to the RT sources was evaluated in terms of calibration coefficients at each stage of accumulated dose. The procedure for BT ^{192}Ir source calibration is described in section 8.3.1.2, and calibration coefficients N_{Ir192} were obtained as the mean of the three 1-Gy irradiations.

8.4.3.3 Ratios of MOSkin sensitivity to ^{90}Sr and RT sources

MO*Skin* response ratios $K_s(t)$ between ^{90}Sr and RT source S were determined at each stage *t* for ^{192}Ir, 6 MV and 15 MV individually, as follows:

$$K_s(t) = \frac{N_S(t)}{N_{Sr90}(t)} \tag{8.4}$$

The least squared method was used to investigate the linear fit of the $K_s(t)$ as a function of $V_{TH}(t)$, and resulting linear correlations were evaluated by the Pearson Product Moment correlation coefficient *r*.

8.4.4 Results and application of method

8.4.4.1 Results

Mean N_s values at each of the three stages of detector lifetime are reported in Table 8.1. The decrease in MO*Skin* sensitivity with accumulated dose was determined as 3.0 ± 0.9 % per 10 Gy, with minimum and maximum values of 2.1% and 4.6% respectively. Variability in the response of the three dosimeters also increased with accumulated dose, represented by the increase from a mean variability of 5.1% at stage 1 to 6.3% at stage 3, further supporting the individuality of the sensitivity changes in each dosimeter.

STAGE	SOURCE	Average N_s	σ (%)
1	^{192}Ir	0.378 cGy/mV	3.5
	6 MV	0.402 cGy/mV	4.2
	15 MV	0.414 cGy/mV	4.2
	^{90}Sr	1.948 s/mV	8.4
2	^{192}Ir	0.405 cGy/mV	3.8
	6 MV	0.428 cGy/mV	4.4
	15 MV	0.443 cGy/mV	5.2
	^{90}Sr	2.043 s/mV	8.4
3	^{192}Ir	0.441 cGy/mV	2.8
	6 MV	0.461 cGy/mV	6.8
	15 MV	0.475 cGy/mV	7.7
	^{90}Sr	2.152 s/mV	7.7

Table 8.1 Mean N_s values at each of the three stages of detector lifetime, and corresponding σ values indicating the reproducibility of MO*Skin* response.

$K_s(t)$ ratios were plotted as a function of detector V_{TH}, recorded prior to each irradiation. Each data point corresponding to the stage of dosimeter accumulated voltage was obtained as the mean of the three irradiations and the three dosimeters for each irradiation type. A linear relationship between V_{TH} and $K_s(t)$ ratios was established as follows:

$$K_s = m_S \cdot V_{TH} + b_s \quad (8.5)$$

m_S indicates linear slope, determined as 0.0009 and 0.0012 cGy/s/V for the BT and linac beams, respectively. The introduction of b_s values offers a dosimeter-specific sensitivity adjustment, supported by the increased variability between the response of individual detectors with accumulated dose, reported in table 8.1. Individual curves are plotted in figure 8.9, with b_s values of 0.1975, 0.1771, 0.1829 cGy/s for the BT source and EBRT beams of 6 and 15 MV beams, respectively. The corresponding R^2 values for the three curves were 0.976, 0.992, and 1.0, resulting in p-values of 0.099, 0.057, and < 0.00001 on the 0.1 confidence level.

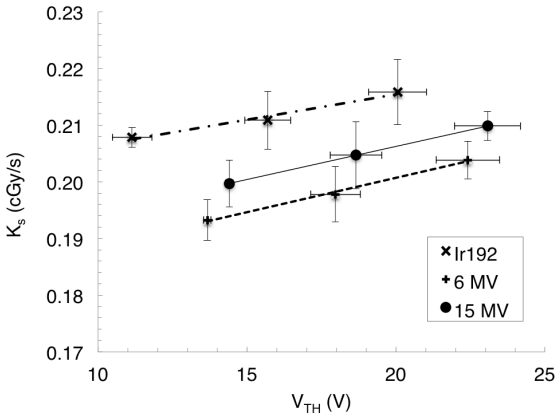

Figure 8.9 Mean $K_s(t)$ values (i.e., averaged over the three irradiations and three dosimeters), plotted as a function of detector V_{TH}, with error bars corresponding to the variability between the three dosimeters.

8.4.4.2 K_S application for MOSkin calibration correction

Initial calibration is performed with the RT source according to the conventional procedure, and dosimeter response to ^{90}Sr is obtained. At the initial t_0 stage of

MO*Skin* calibration, $K_S(t_0)$ are determined for each dosimeter, using the acquired $N_S(t_0)$ and $N_{Sr90}(t_0)$ (according to equation 8.4). b_s values stay constant throughout the life of the dosimeter, and are calculated as follows:

$$b_s = K_S(t_0) \cdot m_S \cdot V_{TH}(t_0) \quad (8.6)$$

Combining equations 8.4 and 8.6, results in:

$$N_s(t) = N_{Sr90}(t) \cdot [m_S \cdot V_{TH}(t) + b_s] \quad (8.7)$$

Finally, from the combination of equations 8.6 and 8.7, the calibration coefficient can be adjusted to account for the decrease in MO*Skin* sensitivity, at any time *t,* using its $V_{TH}(t)$ reading and post-IVD response to ^{90}Sr, as follows:

$$N_S(t) = N_{Sr90}(t) \cdot [K_S(t_0) + m_S \cdot (V_{TH}(t) - V_{TH}(t_0))] \quad (8.8)$$

The standard error of this approach was calculated as 0.1±1.4% at all three stages of accumulated voltage. Total Type A uncertainties were quantified as 1.51%, including MO*Skin* measurement reproducibility for both the RT and ^{90}Sr sources, determined as 0.95 and 1.17%, respectively.

8.4.5 Discussion

Electronic equilibrium within the detector volume is assumed due to the small sensitive volume of the MO*Skin*, the use of large 10x10 cm^2 field sizes in EBRT irradiations, and adequate scatter and build up conditions, as recommended by AAPM and ESTRO for HDR BT [100] and by the IAEA TRS-398 protocol for EBRT applications.

As the MO*Skin* is exposed to increased amounts of radiation, there is a decrease of the electric field in the SiO_2 layer of the MO*Skin* sensitive volume due to holes trapped on the Si-SiO_2 interface, which would lead to a stronger recombination of electron-hole pairs produced by ionizing radiation in the gate of the MOSFET and in particular particles of higher LET, such as the electrons of ^{90}Sr (i.e., the average photon energy of ^{192}Ir is 0.361 MeV, as compared to the spectra of the 6 and 15 MV

linac photons, and the 0.546 MeV electrons measured from ^{90}Sr). This study presents a characterization of this effect by proposing an adjustment that takes into account the amount of dose accumulated on the detector in the calibration coefficient adjustment. The dose accumulated on each dosimeter as a result of the ^{90}Sr irradiations showed an average ΔV_{TH} of 0.68 V, influencing the total decrease in dosimeter sensitivity by <1%, and thus considered negligible.
It is also possible to correct for change in MO*Skin* sensitivity by assuming a uniform accumulated dose effect between dosimeters. For the dosimeters irradiated in this study, sensitivity was found to change by -3.0% per 10 Gy on average, and would have resulted in an average calibration coefficient error of 2.4±4.7%, that increases with accumulated dose to 4.7 ± 5.9% at stage 3 of detector lifetime. These errors are 0.9 and 3.2% higher, respectively, than the error attributed to the approach described in this study.

8.4.6 Post-treatment QC check

Measurement precision can be ensured against any significant change in sensitivity to radiation or overall damage of the device by means of a simple post-treatment quality control check [151]. A method for MO*Skin* QC following IVD is proposed using the ^{90}Sr source and employing the above uniform accumulated dose effect assumption over all MO*Skin*s.

K_s values obtained as a function of the post-treatment detector response to ^{90}Sr (i.e., $K_{s,est}$), can be cross-checked against the expected K_s (i.e., $K_{s,exp}$,), assuming normal detector functionality at the current state of accumulated voltage. The estimated $K_{s,est}$ can be derived according to equation 8.4, as the quotient of the $N_s(t_0)$, and $N_{Sr90}(t)$, measured following the treatment. The initial calibration factor can be adjusted using the expected average MO*Skin* detriment (quantified as 2.96% per 10 Gy in this study).

The $K_{s,exp}$ can be calculated as a function of $V_{TH}(t)$, following equation 8.5, where the b_s is derived for the applicable radiotherapy source at t_0. If the values of $K_{s,est}$ and

$K_{s,exp}$ agree within ±3.12% (i.e., three standard deviations) of MO*Skin* measurement reproducibility, it can be assumed that the detector has functioned properly throughout the treatment.

8.4.7 Conclusions

This proposed method utilizing the ^{90}Sr check source simplifies the sensitivity adjustment procedure, no longer requiring the radiotherapy facility and the large phantom, following the initial calibration of the source. The use of ^{90}Sr does not demand any stringent radioprotection measures, and provides a reliable relative measurement of MO*Skin* response in the case of linear accelerator beams and the ^{192}Ir brachytherapy source. Moreover, the proposed method can be employed as a QC check of the dosimeter to ensure accuracy of the performed IVD. In principle, it is also possible to extend this approach to other MOSFET dosimeters.

This work serves as a proof of method, and further measurements would be required to support these preliminary results prior to the implementation of such technique in a clinical setting.

8.5 *In vivo* verification of the rectal wall dose in gynecological HDR BT

The upper part of the rectal wall, a major OAR in gynecological HDR BT treatments, that is known to be more radiosensitive than the rest of the rectum [80, 114], was chosen for dose verification. An IVD method employing MO*Skin* dosimeters was first developed and a feasibility study of the proposed setup was performed. Following positive results of the feasibility study, the method was extended to in-patient application.

8.5.1 IVD system description

A common semi-flexible rectal probe was assembled with three MO*Skin* dosimeters positioned 10 mm apart, to constitute the dosimetric rectal probe (DRP), allowing a simultaneous point-dose verification in three positions along the rectal wall (figure 8.10).

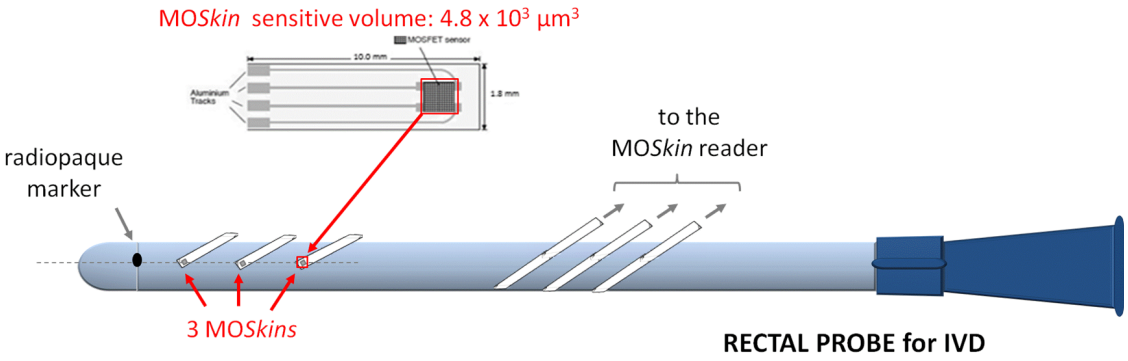

Figure 8.10 Schematic representation of the DRP (not drawn to scale), constituting of a common semi-flexible rectal probe was assembled with three MO*Skin* dosimeters positioned 10 mm apart, and pigtails wrapped around the surface of the probe. A lead radiopaque marker is placed close to the top of the probe to aid in dosimeter localization on the CT images.

MO*Skin*s were calibrated as described in section 8.3.2 prior to probe assembly. The probe was filled with gel in order to eliminate any air cavities and ensure proper scattering conditions. A lead radiopaque sphere was attached at a known fixed position at the top of the catheter to aid with MO*Skin* localization on the acquired CT images. MO*Skin* position was determined on the sagittal view of the CT in Oncentra TPS by defining the central axis on the surface of the probe, in the center of the marker. Each resulting position was then crosschecked with dosimeter positions, measured using a ruler following DRP assembly. A rotation marker indicating upward probe rotation was placed at the bottom of the DRP to aid the radiation oncologist in ensuring that MO*Skin*s are facing the top of the rectal wall.

8.5.2 Feasibility study

The aim of this study was to test the proposed IVD procedure in-phantom, simulating the conditions of the actual treatment, and evaluate the resulting dose discrepancies between measured and planned doses to determine the feasibility of the proposed method for in-patient use.

8.5.2.1 Materials and methods

Dose evaluations were performed in two applicator types used for vaginal treatments at INT: the single-channel and multichannel vaginal cylindrical (MVC) applicators. A wooden plaque was positioned between the applicator and DRP to simulate the anatomical distance between the rectal wall and the vagina. The plaque also aided in the stabilization of the setup throughout the experiments (figure 8.11).

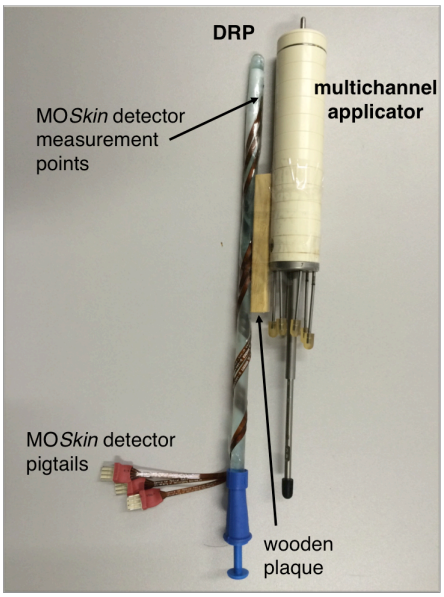

Figure 8.11 DRP and multichannel applicator setup, separated by a wooden plaque to simulate the distance between the vaginal and rectal walls.

The setup was then inserted in the center of a 1 m^3 water phantom, ensuring sufficient backscatter conditions. The experimental setup is shown on figure 8.12, where the DRP and applicator setup (figure 8.11) are visible inside the water phantom. The three MO*Skin* detectors are connected to the reader, which in turn is connected to a laptop with the MosPlot readout software.

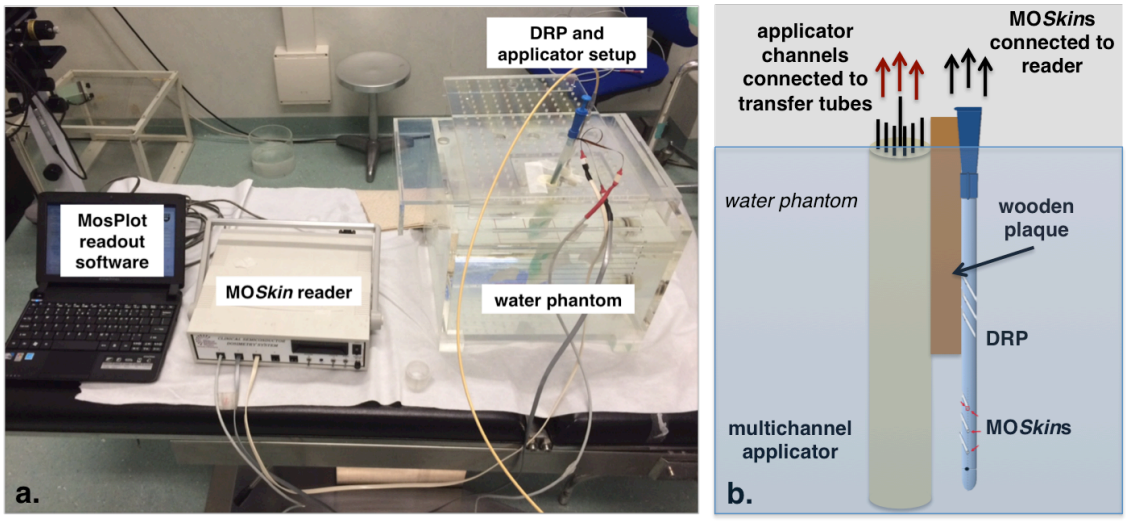

Figure 8.12 Feasibility study experimental setup: (a) entire setup including the water phantom, reader, and computer with readout software and (b) zoomed in schematic of the DRP and applicator setup inside the water phantom (schematic not to scale), with the HDR source delivered through the applicator channels connected to the afterloader by transfer tubes.

CT imaging on both the single-channel and multichannel applicator setups was performed, and three treatment plans were created for each applicator setup. A dose of 300 cGy was prescribed to various targets around the applicator surface: plan no. 1 contained a symmetrical dose distribution, plan no. 2 targeted the upper part of the applicator, and plan no. 3 targeted the lower part of the applicator. The six treatment plans are shown in figure 8.13, with the radiopaque marker and MO*Skin*s (indicated by the red spheres) clearly visible.

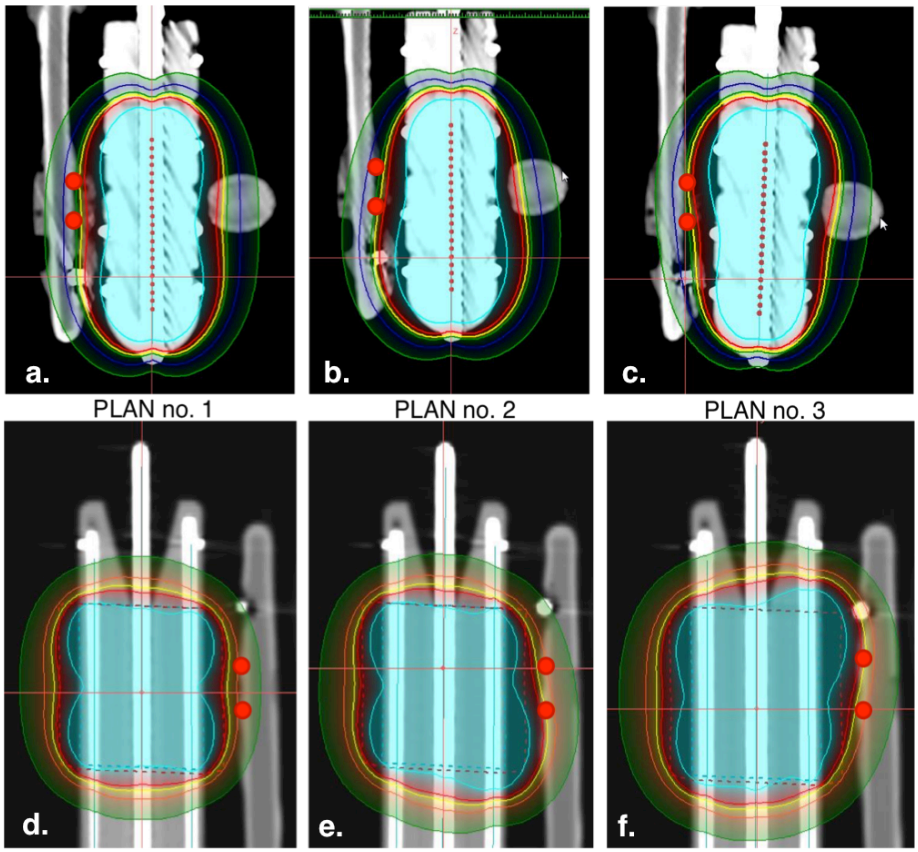

Figure 8.13 Sagittal views of the delivered plans containing various dose distributions. Three plans prescribed to the single-channel applicator are shown on the top images (a,b,c for plans 1, 2, 3, respectively), and three plans corresponding to the multichannel applicator shown on the bottom (d,e,f for plans 1, 2, 3, respectively).

Each plan was delivered three times, and at the end of the experiment MO*Skin*s were recalibrated. Calibration curves were adjusted to account for the change in detector sensitivity using linear interpolation, and calibration factors were adjusted as a function of the V_{TH} reading prior to dose delivery.

One of the three dosimeters was damaged during removal from the probe, and therefore could not be recalibrated. Without recalibration the resulting discrepancies were too high, and the data has been omitted in the final analysis.

8.5.2.2 Results and discussion

An example of online MO*Skin* dose readout (cGy) with respect to treatment time (s) during a MVC applicator delivery is shown in figure 8.14. Dose contributions from individual catheters can be observed from the response plateaus.

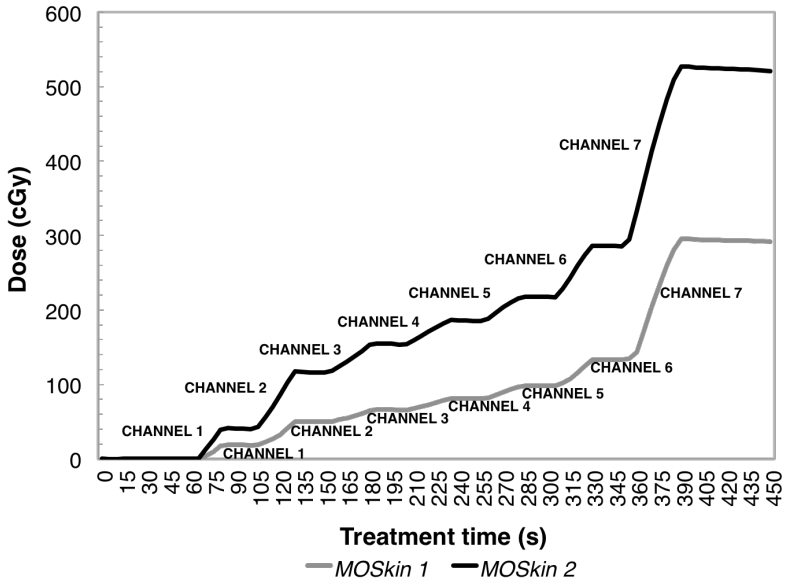

Figure 8.14 Response of two MO*Skin* dosimeters with respect to treatment time, showing dose contributions of individual channels (indicated by dose plateaus) within the MVC applicator.

Integral discrepancies were evaluated between measured, D_{MOSkin} and planned, D_{TPS} doses in cGy, and evaluated according to:

$$|\Delta D|\ (\%) = \frac{D_{MOSkin} - D_{TPS}}{D_{TPS}} \cdot 100 \qquad (8.9)$$

Mean discrepancies of 1.40 ± 0.37 % and 2.79 ± 1.27 % were calculated over the three delivered plans and two dosimeters, for the single-channel and multichannel applicator plans, respectively. Discrepancies ranged between 1.01 and 1.98 % in the single-channel applicator setup, and between 0.83 and 4.27 % in the multichannel applicator setup, with the planned dose always lower than the measured dose. The mean error over all measurements was calculated as 2.09 ± 1.15 % (figure 8.15).

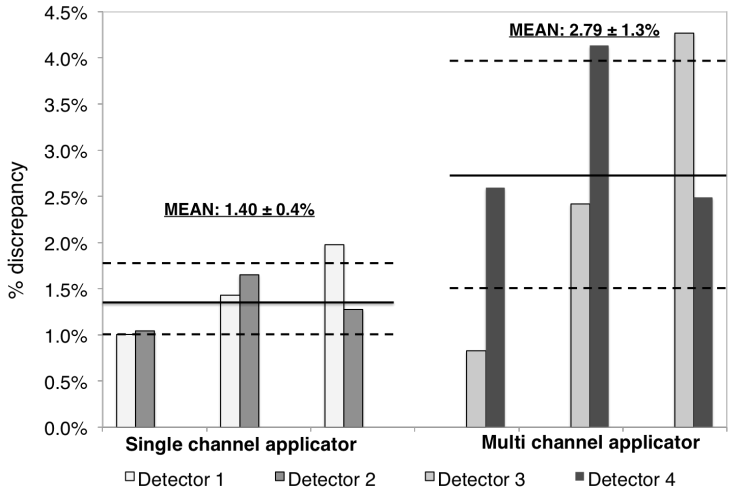

Figure 8.15 Mean dose discrepancies for the single- and multi-channel applicator experiments.

Errors attributed to MO*Skin* localization on the CT and measurement reproducibility were evaluated. Localization uncertainty was determined as ±1 mm in the longitudinal direction and ±0.5 mm in the coronal and sagittal directions. The effect of this uncertainty on the dose varied for each plan, and was quantified as ± 3.62 % on average. The highest difference in dose arising from the 0.5-mm error on the coronal plane was 13 cGy. MO*Skin* reproducibility was quantified as 0.70 ± 0.33 %, calculated as the variation in the measured dose between the three deliveries of each plan (figure 8.16).

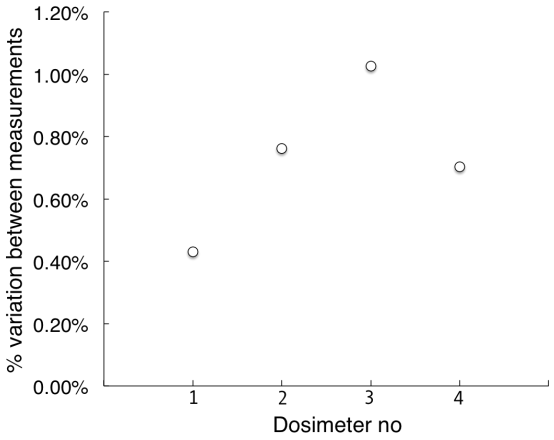

Figure 8.16 Reproducibility of the measured integral dose for each MO*Skin*.

Mean integral dose discrepancy was 1.39 % lower for single-channel applicator deliveries, as compared to the multichannel. This is a result of the higher dose gradients present in multichannel applicator treatments, as shown by the planned dose distributions on figure 8.13. Discrepancies may also arise from treatment deviations in the SDD, as compared to the calibration position, where angular and/or energy dependence may affect MO*Skin* response.

8.5.2.3 Conclusion

The in-phantom feasibility study has demonstrated successful DRP dose verification to the rectal wall during vaginal HDR BT treatment delivery, both with the single-channel and multichannel applicators. MO*Skin* dosimeters have indicated good agreement with the planned doses, measurement reproducibility, and possibility of incorporation into the regular treatment flow.

8.5.3 *In vivo* study

Following favorable feasibility study outcomes, the DRP was ready to be applied to clinical patient treatments. The aims of the following study were to employ the DRP to monitor rectal wall dose *in vivo*, for patients undergoing HDR BT treatments of vaginal cancer; to calculate and compare discrepancies between planned and delivered doses, and assess the potential causes of these discrepancies.

8.5.3.1 Methods

A total of nine patients undergoing gynecological HDR brachytherapy of the vaginal cuff and/or vaginal mucosa were recruited for the study. The cylindrical MVC applicator of 30 or 35 mm in diameter was used in all cases, with a dose prescription of 500-700 cGy to the PTV. Bladder filling was administered using a transurethral Foley catheter, and treatment planning was carried out on pelvic CT imaging of 3-mm slice thickness. The DRP was positioned inside the patient during the implant insertion phase of the treatment, prior to imaging. It was removed following dose delivery along with the applicator.

Patient para-transversal, para-sagittal, para-coronal and 3D CT images visualizing the multichannel applicator and the DRP are shown on figure 8.17. The sensitive volumes of the three dosimeters are marked by arrows and labeled A1, A2, and A3. The large bright mass on the DRP is the radiopaque marker. Contoured OARs can be seen on the bottom right image.

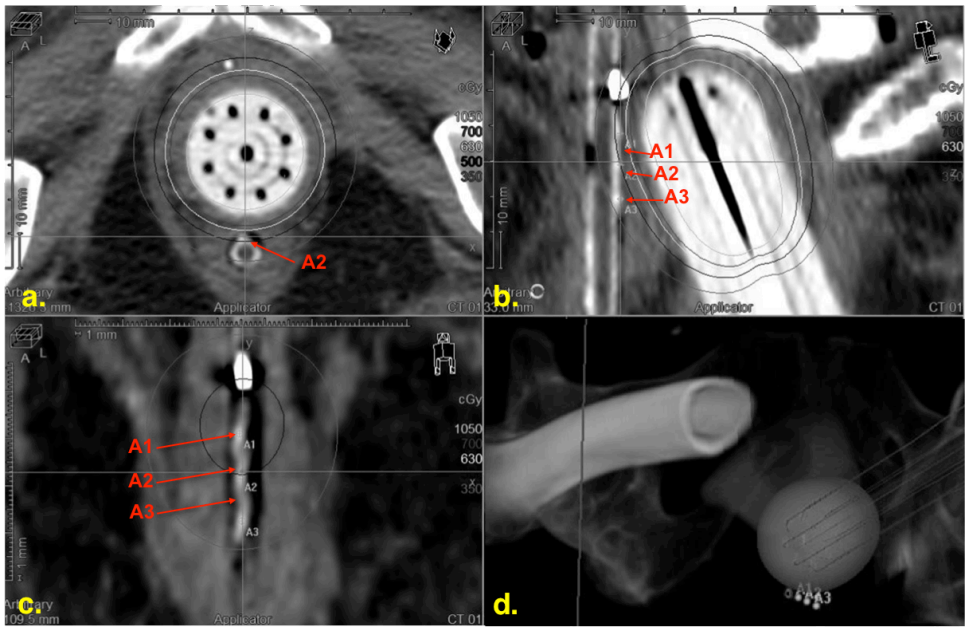

Figure 8.17 Para-transversal (a), para-sagittal (b), para-coronal (c) and 3D images (d) on a patient CT. Three MO*Skin* dosimeters are visible and labeled in red as A1, A2, and A3.

8.5.3.2 Results

A total of 26 treatment sessions were monitored to comprise a total of 78 IVD measurements. The measured doses D_{MOSkin} (grey) and planned doses D_{TPS} (black) are shown on the frequency distribution in figure 8.18. The mean and standard deviation were determined as 308.6 ± 99.4 cGy and 304.0 ±95.7 Gy for D_{MOSkin} and D_{TPS}, respectively.

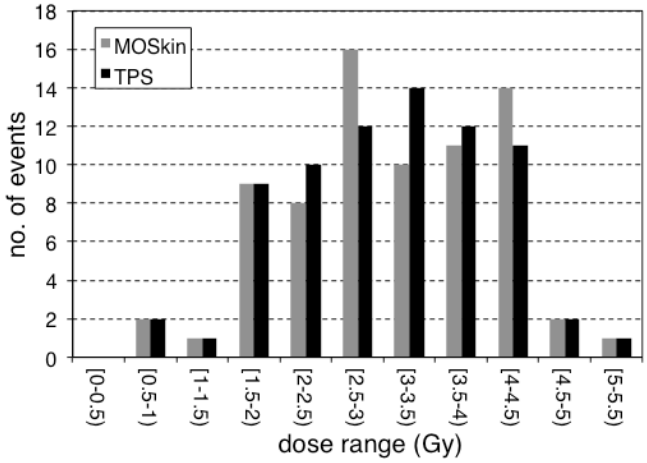

Figure 8.18 Frequency distribution of the measured and TPS dose ranges over all IVD sessions.

The discrepancy between the measured and planned doses was calculated according to equation 8.9. One of the treatments fractions showed dose discrepancies ranging between -28.0 and -36.8 %, caused by longitudinal motion of the DRP visible with the naked eye. This session was deemed an outlier, and was not considered in the overall discrepancy evaluation. In another session a MO*Skin* malfunction occurred, with the detector failing to accurately measure the dose due to physical damage. Thus, 74 measurements were available for further analysis, resulting in a mean ΔD of 2.2 ± 6.9 %. 44.6 % of the measurements were found to be within ±5 % of the TPS dose values, 89.2 % were within ±10%, and 10.8% were found to have a discrepancy exceeding ±10 %. Discrepancy results are plotted in figure 8.19 in increasing order for the 74 measurements.

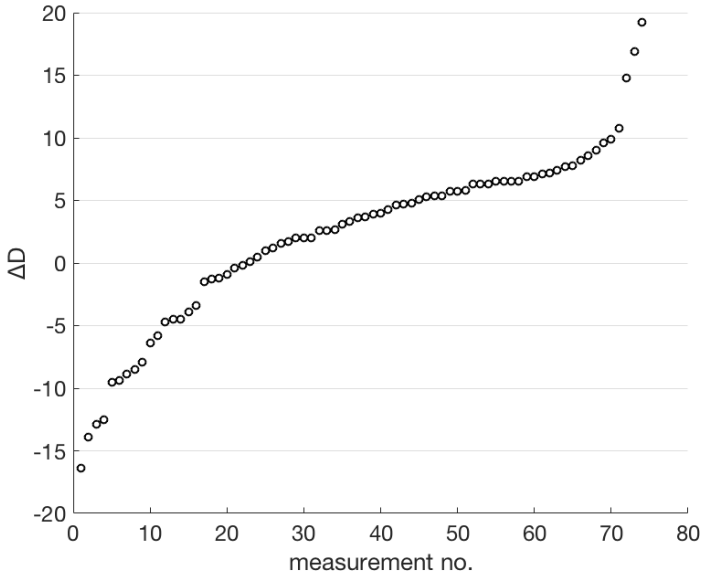

Figure 8.19 ΔD values (%) plotted in increasing order for 74 of the measured rectal wall doses.

|ΔD| distributions were evaluated with respect to detector positioning on the DRP and the time elapsed between the imaging and dose delivery phases using the Wilcox-Mann-Whitney U test (performed with Statistica v. 12, Statsoft, Tulsa, OK, USA).

Correlation was established, showing the highest mean discrepancy of 7.8 ± 4.9% for the most cranial detector (i.e., MO*Skin* #1), whereas the lowest dose discrepancy of 3.9 ± 2.2% was determined for the most caudal detector (i.e., MO*Skin* #3). The mean discrepancy of MO*Skin* #2 was 6.1 ± 3.6%. P-values for the differences between |ΔD| values of MO*Skin*s #1 and #2, #2 and #3, and #3 and #1 were determined as 0.33, 0.14, and 0.002, respectively. Detector positioning and mobility range on the DRP are shown in figure 8.20.

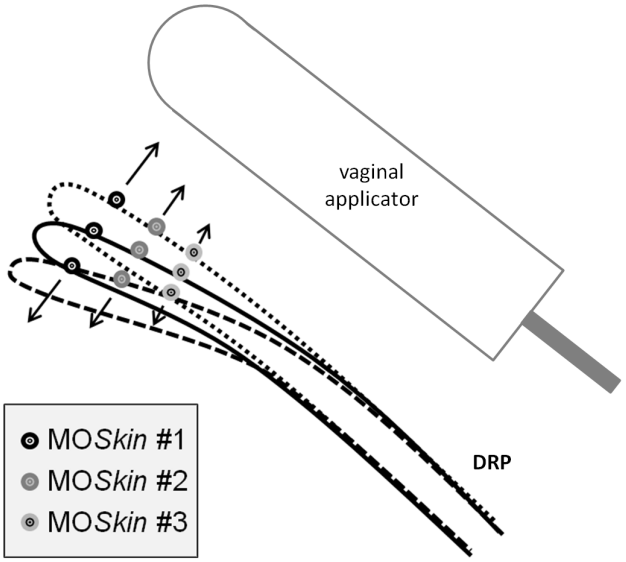

Figure 8.20 MO*Skin* positioning and mobility range on the DRP with respect to the applicator.

|ΔD| distributions with respect to MO*Skin* position on the DRP are shown in figure 8.21, where the rectangle corresponds to standard error and the bars correspond to standard deviation.

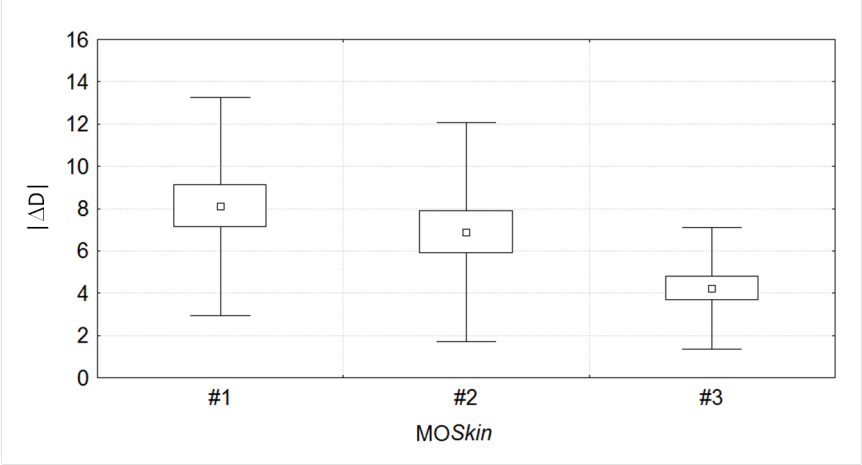

Figure 8.21 Box plot |ΔD| distributions with respect to MO*Skin* position on the DRP.

Mean |ΔD| values were also found to be smaller for lower treatment planning times. Time duration between imaging and dose delivery phases was divided into two groups: group 1 of $t \leq 90$ min and group 2 of $t \geq 90$ min. Mean |ΔD| values for group

1 and 2 were determined as 4.7 ± 3.6 % and 7.1 ± 5.0 %, respectively. A box plot of these results is shown in figure 8.22 where the rectangle signifies standard error and the bars correspond to the standard deviation.

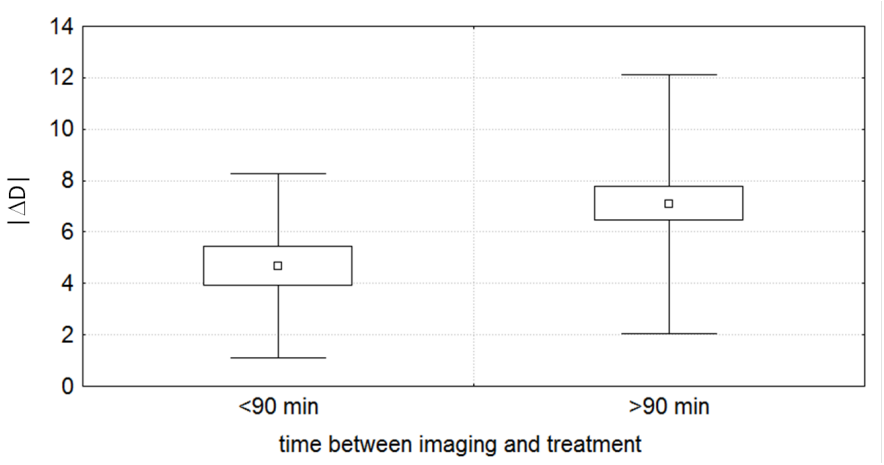

Figure 8.22 Box plot |ΔD| distributions with respect to the time lapse between imaging and dose delivery phases.

8.5.3.3 Discussion

In light of the increased discrepancies in dose with longer time duration between planning and dose delivery phases, it is recommended that planning be kept as short as possible.

It is important to note that TPS point-dose estimations were provided using patient images following implant insertion, and no imaging was performed prior to dose delivery or post-treatment. For this reason it is not possible to identify specific reasons for discrepancies in individual cases, since a number of factors could explain the difference between measured and estimated doses. These include:

1. Morphological changes in the OARs, especially the rectum where the DRP was positioned, as well as the filling of the bladder, and muscle relaxation.
2. Shifting or rotation of the DRP prior to dose delivery.
3. Uncertainties attributed to MO*Skin* IVD and TPS dose estimation.

An uncertainty budget has been estimated as ± 6.2% for MO*Skin* IVD using the DRP, and is reported in Table 8.2. The highest contribution to measurement uncertainty of ±4.5% was the distance dependence, followed by angular dependence with an uncertainty of ±3%, and the other contributors of ≤1.5%.

	Uncertainty (%, k = 1)
MOSkin calibration uncertainty	
S_K determination	±1.5
Phantom assembly, SSD, other TG-43 parameters	±1.0
Intrinstic MOSkin uncertainty	
Reproducibility, temp. dependence, readout res.	±1.5
Change in MO*Skin* sensitivity with exposure	±1.5
Distance (energy) dependence	±4.5
Polar angle dependence	±3
Azimuthal angle dependence	±1
Total uncertainty	**±6.2 %**

Table 8.2 Uncertainty budget estimation for DRP IVD with MO*Skin* detectors.

TPS dose uncertainties have been estimated as ± 7.1 % including variables such as TPS dose calculation, S_K determination, dosimetric medium effects, and image-related uncertainties of applicator and MO*Skin* location registration. A conservative discrepancy threshold of 10% is thus proposed for implementation in the clinic, in which case both the estimated instrumental and TPS-dose estimation uncertainties would remain within the margin of error.

Previous HDR BT IVD studies determined comparable uncertainties: Suchowerska et al. (2011) found a maximum uncertainty of -9% for the 10 patients monitored using scintillation detectors placed inside a urethral catheter [79]; Mason et al. (2016) determined a mean plan uncertainty of 12.3 % in rectal wall MOSFET IVD [153]; Seymour et al. (2011) found a ±20% agreement between 95% of the measured and nominal doses using a diode array [122]; and Carrara et al. (2016)

found integral point-dose uncertainties of 5.7% when incorporating MO*Skin* dosimeters onto the TRUS probe to measure doses to the rectal wall [140]. More specifically, estimated uncertainties using the DRP in gynecological treatments are ~1% higher than those reported for MO*Skin*s mounted on the TRUS probe. This is explained by the higher range of dwell positions on the longitudinal axis of the MVC applicator, as compared to the needles in the prostate procedures, and thus the presence of a wider polar angle during dose measurement. However, the range of azimuthal angles is lower in gynecological treatments, as compared to prostate, and thus azimuthal angle uncertainties are reduced by 1%.

The use of imaging either pre- or post- dose delivery would decrease positional uncertainties of the IVD system. Carrara et al. (2016) determined a 1.5 % decrease in dose discrepancies using the TRUS-integrated MO*Skin* IVD system when comparing measured doses to those indicated on the post-treatment images, as opposed to doses identified in the pre-treatment geometry. Additionally, a method of securing the DRP inside the rectum, such as introducing fixations similar to those incorporated into BT applicators, would also reduce positional shifts.

This study provides insight into an alternative method for rectal wall in vivo dosimetry using MO*Skin* dosimeters, as opposed to the commonly used diode detectors. Although diodes are more practical in that they do not require a sensitivity adjustment throughout dosimeter lifetime, like MO*Skin*s they exhibit energy and angular dependence. In this study MO*Skin*s have shown temperature independence, and like other MOSFETs, they are integral dosimeters that store measured dose. Moreover, MO*Skin* sensors in particular were developed to measure absorbed dose at a 0.07 mm build up depth, making them especially suitable for rectal wall dose measurement.

8.6 Conclusions

The DRP has demonstrated the ability to verify integral dose in gynecological HDR BT treatments in three points along the surface of the rectal wall. It showed ease of incorporation into the established treatment flow, and overall method feasibility. Most patients without rectal complications were eligible for DRP insertion, although the procedure caused additional discomfort to the patient. In light of the results of this study, it is recommended to minimize time between planning and dose delivery to avoid compromising the accuracy of the delivered treatment as a result of increased probability in positional shifts of the implant. Dose discrepancies within ±10 % can be recognized by the DRP system, but at this stage the system is not able to identify the exact reason behind the detected error in dose.

This study has shown the possible ease of IVD incorporation into the current INT treatment, and has presented a new IVD system utilizing small and practical MO*Skin* dosimeters. These findings can be used to develop algorithms for error detection, and to set relevant action levels in the case of detected discrepancies between planned and measured rectal wall doses in gynecological BT treatments, to further increase the safety and reliability of HDR BT.

Chapter 9

Real-time BT QA: Source tracking

9.1 Source tracking for treatment verification

Direct real time measurement of the radiation emitted by the HDR source can provide information on its position, dwell time, and step size, and thus independently validate that the source has been delivered as planned. A comprehensive source tracking system, with spatial and temporal resolutions appropriate for HDR treatments, has the ability to reconstruct both dwell positions and dwell times.

Previous methods of HDR source tracking have been heavily based on imaging: utilizing arrays of ion chambers [154] and diodes [120, 155], as well as scintillation [114], fiber coupled aluminum oxide crystals (Al2O3:C) [156], pixelated [121], and diamond detectors [157]. Other imaging techniques adapted for HDR source QA include MR [158], C-arm [159], x-ray fluoroscopy [160], autoradiography [161], flat panel [113, 162-164], and fluorescent screen imaging [165], as well as radiochromic film [166] and diode based Gallium Nitride (GaN) probes [114, 167, 168]. Radiochromic film measurements can only be used in the pre-treatment stage, whereas MR imaging and autoradiography methods do not allow a temporal resolution

above 2 seconds. Imaging modalities such as C-arm and co-RASOR require expensive equipment that is not always available in clinics. Systems that have shown optimal millimetric spatial resolution include the 2D diode array, Timepix pixelated detectors, ion chambers, autoradiography, GaN probes, EPIDs, fluorescent screen imaging, and radiochromic film when used in combination with photodiodes. The 2D diode array proposed by Espinoza et al. (2015) has the ability to be read out in real-time as well as allow source position and dwell time reconstruction with sub-millimeter and sub-second precision, respectively [120]. Wang et al. (2014) and Guiral et al. (2016) in particular proposed to incorporate four GaN-based dosimeters into a commercial MVC applicator for gynecological HDR BT treatments, resulting in sub-millimeter and sub-second HDR source tracking capability [167, 168]. However, the proposed method utilizes four of the MVC applicator channels, and so limits the dose distribution potential for gynecological treatments. Thus the need for a system that can verify the source position, step size, and dwell time with sub-millimeter and sub-second spatial and temporal resolutions in real-time remains.

9.2 Aim of this chapter

The aim was to develop a prototype of a multichannel brachytherapy applicator with a verification system embedded around its surface, and verify the system's suitability for HDR BT source tracking in real time. The first step was to select and characterize diode detectors and their packaging suitable for the system, and establish optimal measurement settings, considering specific demands required by HDR BT treatments. The second step was to assemble and calibrate the system, and the third step was to evaluate the system's performance by verifying its ability to reconstruct ^{192}Ir dwell positions and times using the defined methodology.

The diode characterization study has been submitted to the Journal of Physics as Romanyukha, A.A., Carrara, M., et al., *Preliminary epi-diode characterization for HDR brachytherapy quality assurance*.

The system calibration and performance verification studies have been submitted to Physica Medica Journal (invited paper) as Romanyukha, A.A., Carrara, M., et al., *An innovative gynecological HDR brachytherapy applicator system for treatment delivery and real-time verification*.

9.3 Detector characterization and definition of sensitive volume thickness

The first step was to characterize the diode detectors selected for the system, and establish optimal sensitive volume thickness and readout settings for measurement of the ^{192}Ir inside the BT bunker. Then the diodes' dynamic range, temporal and spatial resolutions, and method of dwell time reconstruction were defined, followed by the investigation of source-strength dependence of the response for the range of S_K used in the clinic.

9.3.1 Materials

Measurements were performed in the CMRP lab and the HDR BT bunker at INT on two sets of diodes containing different silicon chip thicknesses. The first set was tested with the Nucletron microSelectron afterloader system, and the second set was tested with the Flexitron afterloader system and a new treatment communication console (TCC) recently commissioned at the INT BT facility.

9.3.1.1 Diodes and readout system

Diodes have been developed at the CMRP and assembled on a Kapton pigtail using the "drop-in" technique [169] to reduce energy dependence. The selected diode probes have a Kapton pigtail of 325 mm in length and contain the diode with a sensitive area of 1.5 x 1.5 mm^2 (figure 9.1).

Figure 9.1 (a) Diode wire bonding covered in epoxy to increase detector durability (b) Diode bonds and silicon sensitive chip (1.5 x 1.5 x 0.038 mm^3), as viewed under a microscope).

The first and second diode sets were p-type and n-type, respectively, and had silicon layer thicknesses of 38 and 500 µm, respectively. The first set contained epitaxial (epi) diodes with 0.1 kOhm-cm resistivity, and the second set contained bulk diodes with 5 kOhm-cm resistivity. A schematic of the p-type epitaxial diode topology with packaging drop-in method patented and characterized at the CMRP [170] is shown in figure 9.2. The n-type diodes used in this study are analogous in assembly and construction, but with base thickness and resistivity of 500 µm and 5 kOhm-cm, respectively, in order to increase sensitivity and improve the signal-to-noise ratio (SNR) for dose rate measurement at larger distances between the ^{192}Ir source within HDR BT needles and the diode.

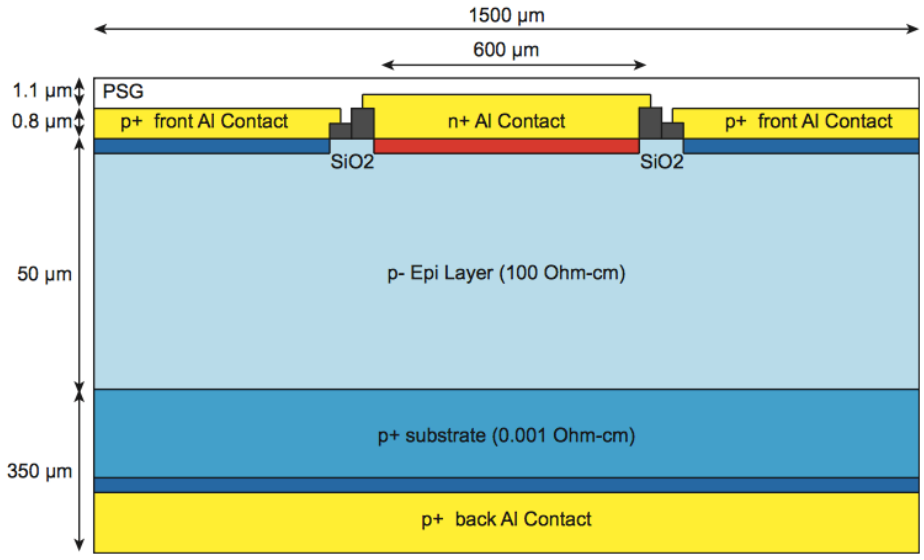

Figure 9.2 Schematic of the p-type epitaxial diode topology, taken from [170].

These particular diodes have been selected for use with the HDR BT source due to their radiation hardness, sensitivity, and passive mode real-time readout, minimizing leakage current and guaranteeing suitability for in-patient use.

The readout system, also designed in the CMRP, functions by integrating the charge over the window selected in the readout settings i.e. the integration time. The system consists of an AFE0064 (analog front end) electrometer with 64 circuits for current integration, an FPGA (field programmable gate array), and power supply boards. The differential analog-to-digital converter ADS8363 communicates with the FPGA, while the FPGA Xem 3001 has an embedded USB to transfer data from the reader to the PC. Sensitivity of measurement can be adjusted by selecting the charge capacity and can reach 9.6 pC per 1-kHz readout, corresponding to the number of times that the capacitor discharges in each readout interval.

The reader has four channels and can accommodate up to four detectors at a time. Proper grounding and shielding were ensured during detector and reader assembly, including aluminum coverage to minimize radiofrequency noise (figure 9.3b). The sensitive components of each diode were covered with a thin layer of Kapton and epoxy in order to protect the exposed wire bonds and increase detector durability (figure 9.1a).

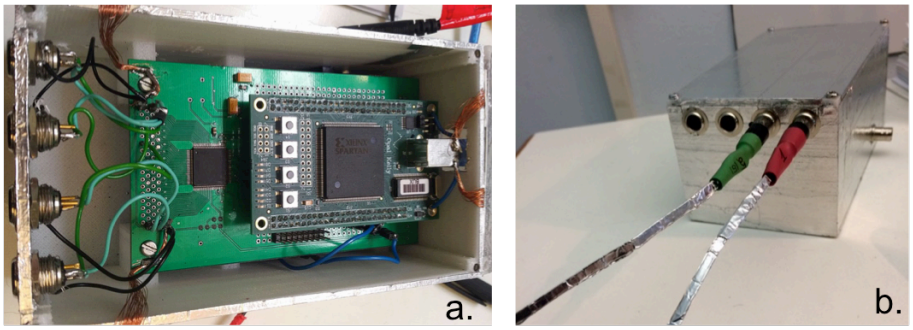

Figure 9.3 (a) Reader containing four channels for simultaneous readout of four diodes, and composed of three boards: AFE, FPGA, and power supply. (b) Reader assembled and covered in aluminum, with two diodes connected.

A number of readout settings can be adjusted to suit the particularities of the HDR source, especially when a wide range of dose rates is involved. The range setting is between 0 and 7, and corresponds to maximum charge values of 0.13 and 9.6 pC, respectively, to be integrated at each readout step. The Histogram readout software (figure 9.4) displays both the instantaneous (top) and integral (bottom) responses in each of the four channels. Diode readout in channel 3 is shown, along with settings such as the integration time, readout frequency, and acquisition time that can be adjusted for each measurement.

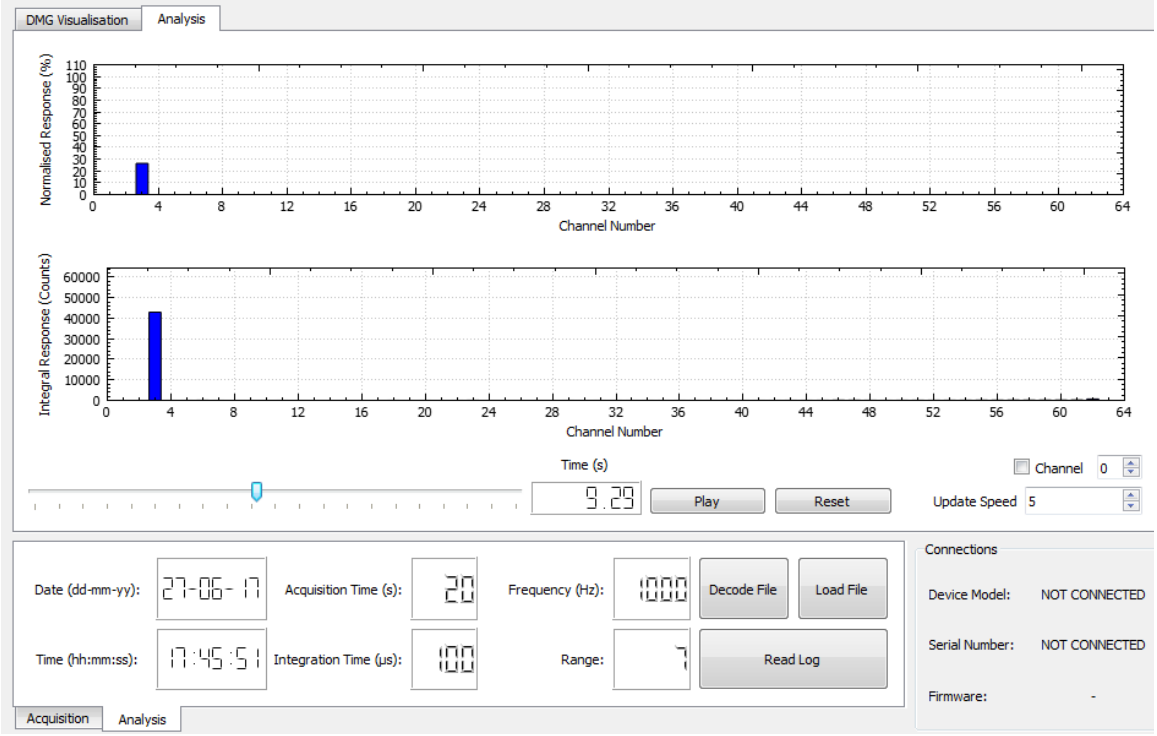

Figure 9.4 Histogram software displaying the instantaneous (top) and integral (bottom) responses of a diode reading in channel 3.

The instantaneous response is expressed as a fraction of the full scale of charge permissible by the corresponding range setting, and measured as the percentage of the total AFE capacity occupied by the measured raw counts C_{RAW}. The response at the selected readout frequency is then converted into the total charge by multiplying the

detected true counts C_{TRUE} by the corresponding maximum charge of the range setting (pC), where C_{TRUE} is obtained according to equation 9.1:

$$C_{TRUE} = \frac{C_{RAW}}{65535} \cdot 100 \quad (9.1)$$

The frequency of each step can range between 1 and 1000 Hz, and the integration time can be set between 50 and 400 μs.

9.3.2 Methods

The thickness of the sensitive silicon chip of the diode impacts the dynamic range of detector signal with respect to HDR source position. The first set of diodes contained silicon chips with a thickness of 38 μm, aimed to provide a high spatial resolution and reduce response averaging.

9.3.2.1 I-V characteristics

In order to verify low noise and a constant relationship between applied voltage and diode current prior to assembly and shielding, current-voltage (I-V) characteristics were measured by applying up to 30 V in various increments. P-type epi-diodes (38 μm) and n-type bulk diodes (500 μm) were tested, and their I-V responses are shown in figure 9.5.

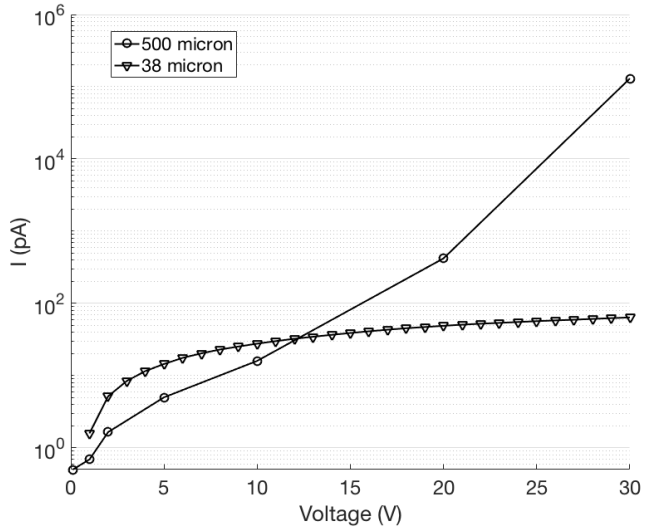

Figure 9.5 Example of obtained I-V characteristics of p-type (38-μm) and n-type (500-μm) diodes.

Kapton pigtails of the detectors were assembled with three-pin female connectors, and aluminum shielding was added around the entire dosimeter to minimize noise and eliminate the detectors' sensitivity to light.

9.3.2.2 Definition of sensitive volume thickness

The main parameters for evaluation of diode suitability for HDR BT source tracking were defined as:

1. Dynamic range of the diode.
2. Spatial resolution.
3. Temporal resolution.
4. Effect of dose rate on diode response at S_K range of 10 - 45 $mGy.m^2.h^{-1}$.

These parameters were evaluated by positioning the detectors inside a water equivalent plastic phantom at a distance of 3 mm from the catheter, where the HDR source will travel on the longitudinal axis (figure 9.6). The smallest step size of 2.5 mm and dwell times of 2 seconds were selected and delivered with the microSelectron afterloader unit. The source was sent to dwell in all 48 available dwell positions inside the catheter.

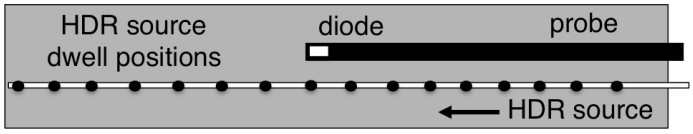

Figure 9.6 Setup of the diode characterization measurements.

Optimal readout settings were determined in the BT bunker to account for specific noise characteristics of the treatment theater by modifying the settings of readout frequency, integration time, and range. Diode range as a function of S_K was investigated by acquiring diode response for S_K values between 38.0 and 13.2 $mGy.m^2.h^{-1}$.

9.3.3 Results

Diode signal for integration times of 200, 300, and 400 μs, respectively, is plotted in figure 9.7. The highest permitted integration time of 400 μs was selected as optimal in

order to achieve maximum detector sensitivity. The last sharp peak in all three curves visualizes the retraction of the HDR source into the afterloader.

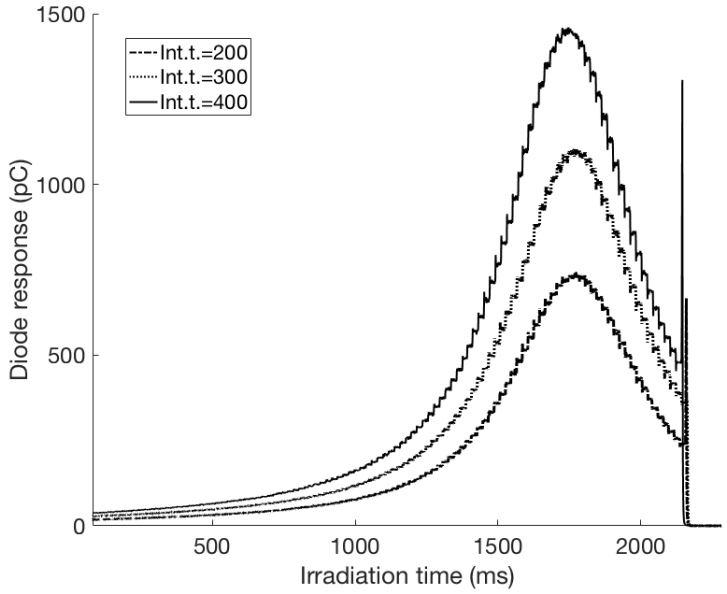

Figure 9.7 Variation in diode response (pC) for selected integration times of 200, 300, and 400 μs.

Dynamic range was determined as the number of discriminated dwell positions multiplied by the source step size, and was assumed to extend until 95% of the binned data points in each cluster no longer conformed to their corresponding cluster group (i.e., dwell position response range (pC)), within two significant figures. Diode response binned into 0.05-s clusters is shown in figure 9.8, with the peak corresponding to the closest dwell position to the diode sensor. The difference in the SNR in two different SDDs is shown by the inserts.

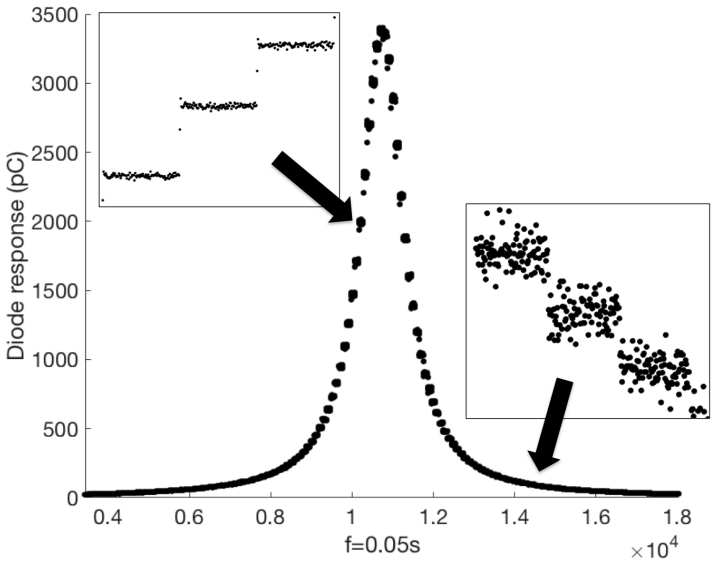

Figure 9.8 Diode response (pC) as a function of irradiation time (bin frequency=0.05 s). SNR for two SDDs is shown in the imbedded figures.

Diode response, normalized for S_K, is plotted as a function of treatment time with range settings of 4, 5, and 6 and S_K of 25.4 mGy.m^2.h^{-1} in figure 9.9. Range settings of 4 and 5 have shown to be insufficient as diode response oversaturates before the source reaches the closest available dwell position with respect to the center of the diode. Range 6 or higher was therefore determined optimal in order to accommodate the wide range of dose rates utilized in the clinic.

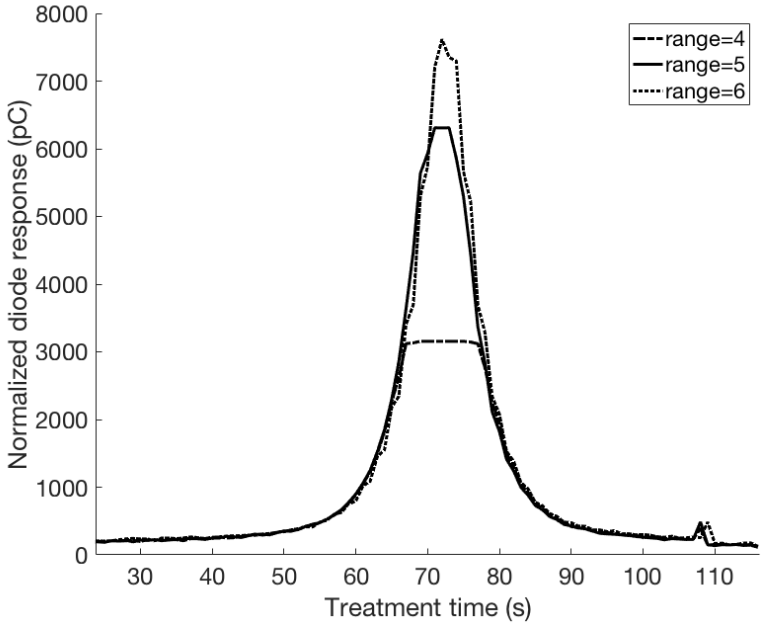

Figure 9.9 S_K-normalized mean diode response in each dwell position as a function of treatment time (s) for readout range settings of 4, 5, and 6.

Diode response as a function of ^{192}Ir source strength is shown in figure 9.10 with the three curves corresponding to source strengths of 13.2, 34.6 and 38.0 mGy.m^2.h^{-1}. Figure 9.10a shows the total diode response in terms of collected charge with respect to treatment time, where the highest range of charge corresponds to the highest S_K value of 38.0. In figure 9.10b the same three curves normalized for S_K are plotted. For a large variation in source strength (i.e., -26 mGy.m^2.h^{-1}) some diode dependence on the dose rate can be observed. Normalized diode response appears overall stable for source positions located at ±12.5 mm, whereas for dwell positions located further away the response changes due to lower SNR at lower activities.

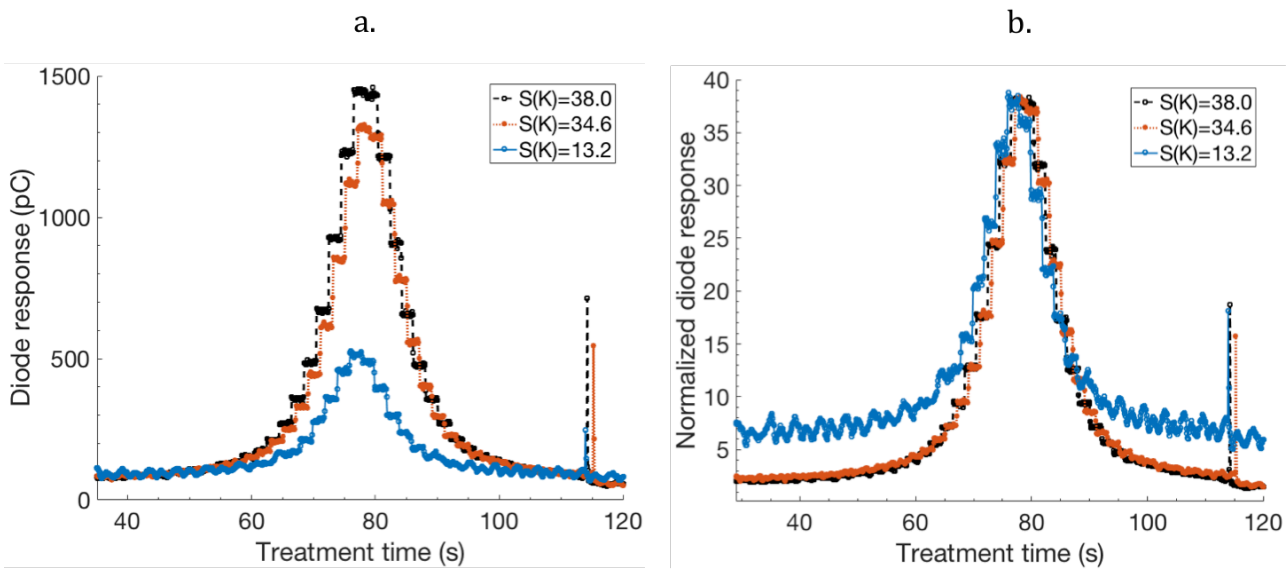

Figure 9.10 Total (a) and S_K-normalized (b) diode response for various source strengths.

Diode dynamic range with respect to source distance from the center of the diode sensitive volume is plotted in figure 9.11. Diode response peaks at a SDD of 0 mm (i.e., when the source dwell position is directly above the diode), and decreases in both directions as the source moves away. Dynamic range for diodes 1, 2, and 3 was determined as ±20 mm, ±18 mm, and ±17 mm, respectively. Fluctuation of diode response in a single dwell position was quantified as 0.5 - 2.6% for diode 1, 0.3 - 1.3% for diode 2, and 0.9 - 3.0% for diode 3, increasing with SDD. The error bars on both the x- and y-axes are too small to be visible on the plot.

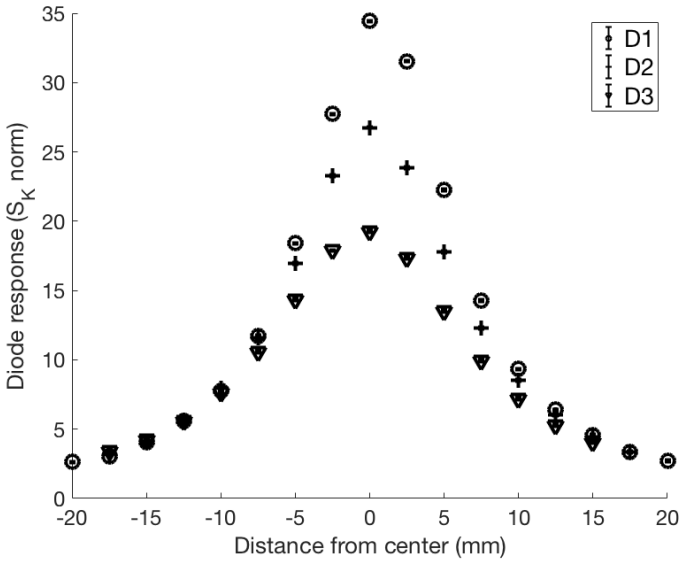

Figure 9.11 S_K-normalized diode response as a function of SDD.

Source dwell time can be determined from the plateaus in diode signal, shown in figure 9.12, where each plateau corresponds to a dwell time of 2 seconds for each dwell position.

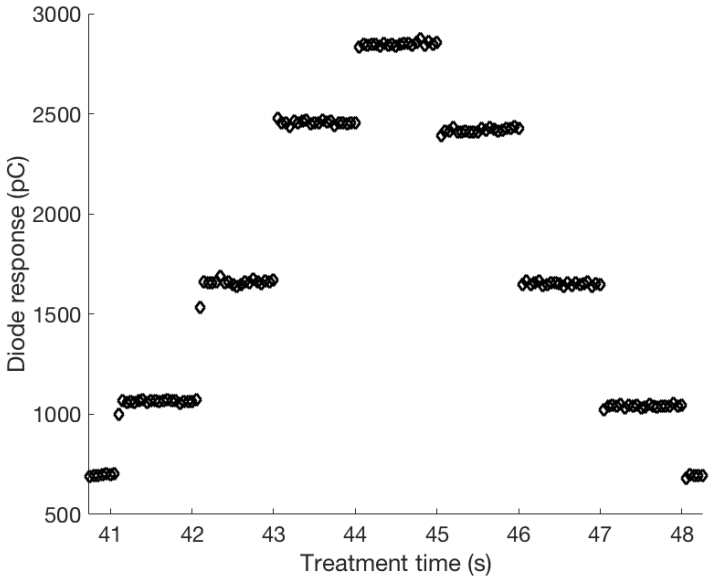

Figure 9.12 Diode response plateaus, corresponding to individual dwell positions.

The dwell time is calculated as the ratio of the number of measurements in each plateau and the frequency of readout, and was verified with an accuracy of ± 0.3 s, as

compared to the nominal dwell time indicated by the TCC. Moreover, source transit time can be observed, and is represented by single points between the plateaus in figure 9.12. It is shown in more detail in figure 9.13, showing diode response with respect to treatment time in a single dwell position. Source transit time is visualized before and after the source reaches the dwell position, traveling past the diode in both directions. The source transit time was calculated as 0.3 s both as it traveled from the afterloader to the planned dwell position and as it retracted back, for a total of 0.6 s in transit.

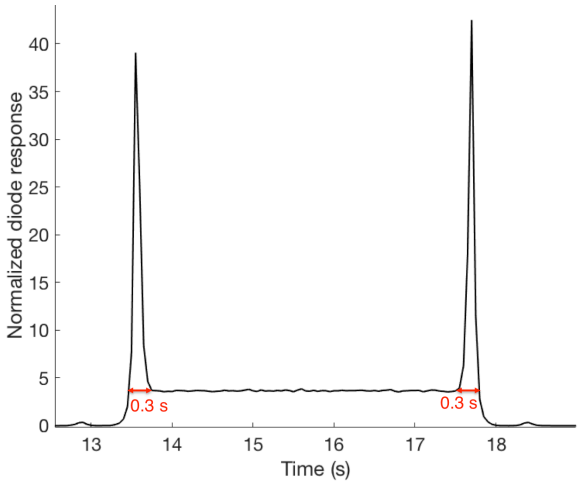

Figure 9.13 Time contribution of the source transit, represented by the two response peaks.

9.3.4 Conclusions

Diode response has been evaluated with respect to various measurement settings of the reader and readout software, as well as the treatment parameters such as source step size, dwell time, and range. A balance between minimal noise and maximum diode sensitivity can be obtained using the established measurement settings, and spatial and temporal resolutions required for HDR BT source tracking in the clinical range of ^{192}Ir S_K values. A method for dwell time calculation has been formulated and tested to show a ± 0.3 s agreement with the TCC.

The dynamic range of the epi-diodes indicated that approximately 40 mm of gynecological applicator coverage can be obtained, which in some cases may be shorter than the clinically relevant region of ~50 mm.

9.3.4.1 Change of HDR afterloader

It is important to note that following this stage of the study the microSelectron afterloader was replaced with the Flexitron (Elekta Brachytherapy, the Veenendaal, NL) afterloader at the INT BT facility.

The Flexitron afterloading unit contains 40 transfer tube connections, allows a minimal step size of 1 mm, positional accuracy of ± 0.5 mm and a minimum dwell time of 0.1 seconds. The ^{192}Ir source (Flexisource, Elekta) core is 3.5 mm (i.e., 0.1 mm smaller than in the microSelectron unit). The TPS is the corresponding version of Oncentra Brachy.

9.3.5 Higher sensitivity diodes

In order to extend the dynamic range of the diodes, new detectors were developed, increasing the thickness of the silicon sensor to 500 μm, and thus increasing photon detection. Measurement settings were modified to accommodate the higher diode sensitivity with range and integration settings of 7 and 200 μs, respectively, and readout frequency kept at 1 kHz.

9.3.5.1 Methods

Three diodes were used to investigate dynamic range as a function of temporal and spatial resolutions by varying the dwell time and source step size between positions. The new Flexitron afterloader system allowed diode spatial resolution to be tested at a 1-mm step size, as opposed to the 2.5 mm permitted by microSelectron in the previous measurements. Diodes were positioned inside a water equivalent phantom and the source was sent to dwell positions of 288-100 mm at step sizes of 1, 2, and 3 mm, maintaining the same measurement setup shown in figure 9.6. To obtain 100 data points for each of the selected temporal resolutions of 0.1 and 0.2 seconds, respectively, dwell times of 5 and 10 seconds were used for statistical accuracy.

9.3.5.2 Results

Diode range as a function of temporal resolution is plotted in figure 9.14, where data bins of 0.05 and 0.1 s correspond to temporal resolutions of 0.1 and 0.2 s, respectively. For a step size of 1 mm and a temporal resolution of 0.1 s the mean diode range was 69 ± 3 mm, increasing to 109 ± 5 mm and 138 ± 9 mm for 2 and 3-mm step sizes, respectively. For a temporal resolution of 0.2 s and a 1-mm step size a range of 87 ± 3 mm was determined, increasing to 133 ± 5 mm and 176 ± 6 mm for source step sizes of 2 and 3 mm, respectively. To accommodate the temporal and spatial resolutions of 0.1 s and 1 mm, respectively (i.e., the accuracy permitted by the afterloader device), a data bin size of 0.05 s was selected. Readout frequency of 1 kHz was used in order to obtain 100 readouts for each 0.1-second period.

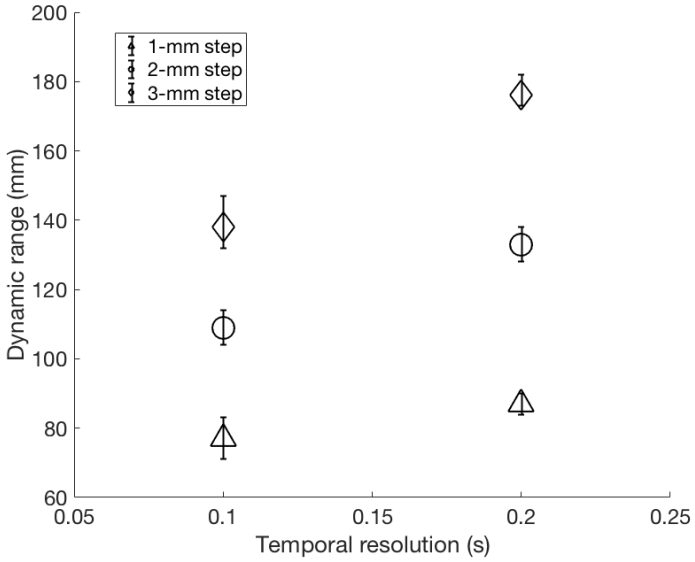

Figure 9.14 Dynamic range of the diodes as a function of temporal resolution (i.e., measurement bin size), and spatial resolution (i.e., source step size).

Dosimeter characteristics of both diode sets are reported it Table 9.1. Diode ranges are reported as mean values over the three diodes tested in each set.

	Set no. 1	**Set no. 2**
Type	p-type	n-type
Resistivity	0.1 kOhm-cm	5 kOhm-cm
Si chip volume (mm^3)	1.5 x 1.5 x 0.038	1.5 x 1.5 x 0.5
Katpon pigtail length (mm)	325	325
Readout settings		
Range	6	7
Integration time (μs)	400	200
Frequency (kHz)	1	1
Dynamic range measurement		
S_K ($mGy.m^2.h^{-1}$)	25	37
Source step size (mm)	2.5	2
Dwell time (s)	2	0.2
Dynamic range (mm)	**36 ± 4**	**133 ± 5**

Table 9.1 Characteristics of the two sets of epitaxial diodes.

9.3.5.3 Conclusions

The dynamic range of the sensitive diodes was found to extend 97 mm further than in the first set, and thus coverage of the top 50 mm of the applicator can be achieved.

These results were then used to determine optimal diode positioning on the surface of the multichannel applicator prototype, allowing temporal and step size resolutions of 0.1 s and 1 mm, respectively.

9.4 The source tracking system and calibration

The next step was to assemble and calibrate the proposed system by defining the relationship between the fixed position diode response and source location, with respect to a reference point.

9.4.1 The proposed system

A gynecological multichannel applicator was designed based on the commercially available Vaginal CT/MR Multi Channel Applicator (Elekta Brachytherapy, TH Veenendaal, NL). The applicator prototype is 30 mm in diameter and contains seven peripheral and one central channel, with the possibility of inserting an intrauterine tube when required for the treatment. The prototype was produced at UOW using water-equivalent plastic. To accommodate three detectors on the surface of the applicator, dedicated grooves were made between peripheral channels 1 and 7, 3 and 4, and 5 and 6. The three diodes were positioned at 35, 37, and 39 mm from the applicator tip, respectively (figure 9.15a), to ensure coverage of the top 50 mm. In order to simulate radiation interactions inside the patient and provide adequate scattering conditions, a phantom of 160 x 220 x 160 mm^3 was fabricated using the same water equivalent material to surround the applicator without any air gaps (figure 9.15b). Plastic catheters with a diameter of 2 mm and an external length of 293 mm (i.e., “catheter with collar 6F”) were placed in the peripheral channels and the reusable Intravaginal CT/MR Tube was placed in the central cavity.

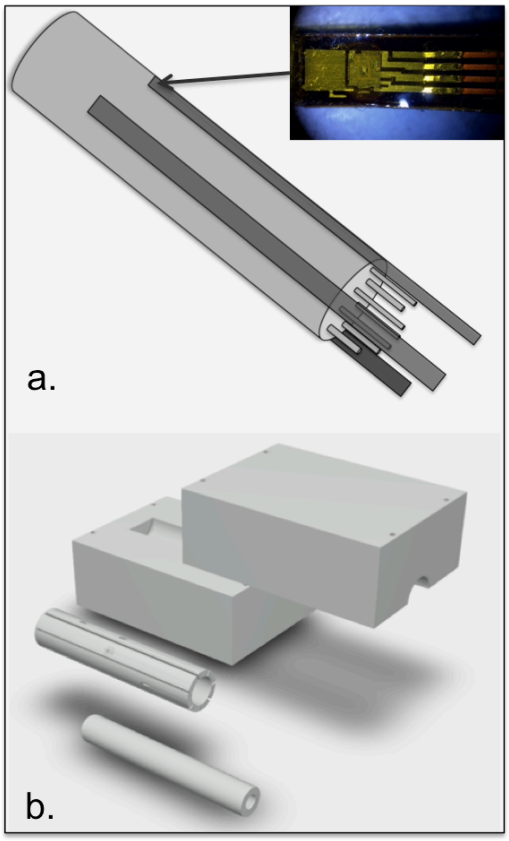

Figure 9.15 Cylindrical multichannel applicator with three diodes positioned around the surface of the applicator (a). Custom-made water equivalent phantom to surround the applicator (b).

9.4.2 System calibration

A calibration of the system was required in order to establish a method for dwell position reconstruction at any given time of the treatment, with respect to a reference point and fixed locations of the three detectors on the applicator.

The location of the first dwell position in each of the eight channels in the applicator was determined using GafChromic film measurements. The film was wrapped around the applicator surface with the edge of the film aligned to the tip of the applicator. The distal tip of the applicator (with respect to the afterloader) was chosen as the reference point for determining the source location within the applicator. The first dwell position in the central catheter was measured using a separate strip of film. A

total of three dwell positions per catheter, located at 50 mm apart, were delivered to ensure precision of measurement. Position locations exposed on the GafChromic film were evaluated using a Matlab script to determine the center of each ^{192}Ir exposure and its location with respect to the edge of the film (figure 9.16). The distances (mm) from the applicator surface, ± 0.1mm (k=1), were 7.1 mm, 6.9 mm, 6.8 mm, 7.1 mm, 6.9 mm, 6.5 mm and 6.5 mm, for the peripheral catheters 1 to 7, respectively. The first dwell position in the central catheter was set as 5.5 mm (taken from the Elekta user manual).

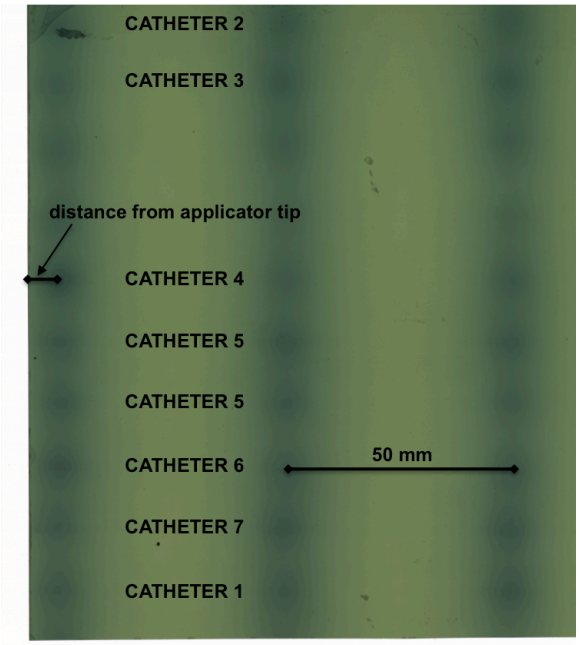

Catheter	d from the tip (mm)
1	7.1
2	6.9
3	6.8
4	7.1
5	6.9
6	6.5
7	6.5
Central	5.5

Table 9.2

Figure 9.16 GafChromic film measurement results. The location of the first dwell position in each catheter is reported in table 9.2, as the distance d, ±0.1 mm (k=1), from the applicator tip.

In every catheter each dwell position was characterized by its specific diode response with respect to the reference point. A combination of two diodes was employed for each catheter. The source step size was selected as 1 mm, and the source was sent to dwell positions of 288-100 mm in the peripheral channels and 300-100 mm in the central channel, respectively, for a dwell time of 1 second in each position.

The acquired diode response was divided by S_K at the time of measurement, and plotted as a function of distance from the applicator tip (mm) established with the GafChromic film. Mean diode response was plotted with respect to its location from the reference point. The highest responses of two of the three diodes per catheter were fitted with multi-term Gaussian functions. The two diodes, number of Gaussian terms per fit, and the corresponding R^2 values for each catheter are reported in table 9.3. D_{HR} and D_{LR} correspond to the high and low response diodes in each catheter, respectively. The two-diode combinations of Gaussian functions for each catheter are shown in figure 9.17. The Gaussian terms for each catheter are provided in Table 9.4.

Catheter	**Diodes**		**No. of Gaus. terms**		**R^2 values**	
	D_{HR}	***D_{LR}***	***D_{HR}***	***D_{LR}***	***D_{HR}***	***D_{LR}***
1	D2	D3	4	3	1	0.9998
2	D2	D3	4	3	1	1
3	D3	D2	4	2	1	0.9998
4	D3	D1	4	2	1	0.9998
5	D1	D3	4	2	0.9995	0.9999
6	D1	D2	3	2	0.9999	0.9998
7	D2	D1	4	2	1	0.9998
Central	D1	D3	3	3	1	1

Table 9.3 The diodes, number of Gaussian terms per fit, and corresponding R^2 values for each catheter.

DIODE #	Gaus term	C.1	C.2	C.3	C.4	C.5	C.6	C.7	CENTRAL
	a1				9.25	12.31	40.42	7.88	10.29
	b1				36.97	41.99	36.23	36.49	36.81
	c1				12.78	3.76	4.73	11.22	10.76
	a2				8.46	15.64	42.47	10.06	-5.69
	b2				36.96	51.66	36.09	36.47	59.02
	c2				33.41	15.12	10.26	29.36	21.09
D1	a3					64.17	12.53		13.78
	b3					37.73	36.70		44.33
	c3					6.85	28.64		30.96
	a4					35.12			
	b4					42.13			
	c4					21.98			
	a1	50.19	0.59	2.94			5.54	0.20	
	b1	36.98	36.28	36.41			35.58	16.57	
	c1	4.39	4.06	13.81			12.13	4.20	
	a2	52.09	6.38	6.14			7.38	25.19	
	b2	36.79	36.25	36.63			35.76	36.91	
	c2	9.11	10.15	34.94			31.51	11.55	
D2	a3	0.68	9.77					15.80	
	b3	20.76	35.91					37.05	
	c3	3.40	20.97					5.96	
	a4	12.56	1.97					9.12	
	b4	36.88	74.61					37.37	
	c4	26.25	441.30					30.38	
	a1	0.63	2.54	55.32	0.00	5.97			5.63
	b1	33.97	38.88	39.26	38.53	39.14			39.08
	c1	3.34	6.52	4.10	0.05	12.95			9.81
	a2	5.39	7.03	18.58	16.48	7.54			3.88
	b2	34.17	38.93	39.20	39.61	39.45			40.05
	c2	34.37	34.59	15.17	6.21	32.57			44.28
D3	a3	2.82	10.11	47.66	24.09				9.25
	b3	33.78	38.51	39.27	39.55				39.19
	c3	11.88	13.75	7.94	12.01				18.45
	a4			5.86	9.10				
	b4			39.62	40.05				
	c4			38.86	31.35				

Table 9.4 Gaussian terms for the two diodes with the higher signals in each catheter.

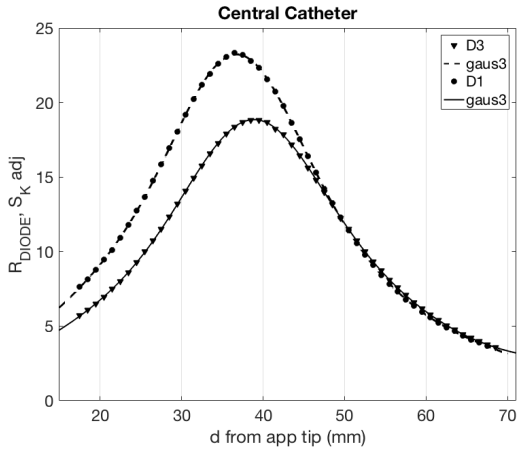
Central Catheter
D3
gaus3
D1
gaus3
R_{DIODE}, S_K adj
d from app tip (mm)

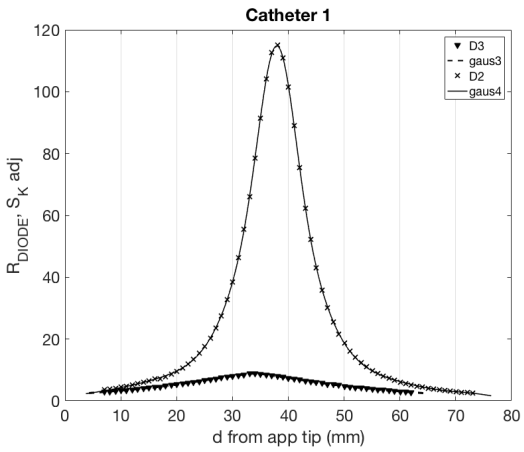
Catheter 1
D3
gaus3
D2
gaus4
R_{DIODE}, S_K adj
d from app tip (mm)

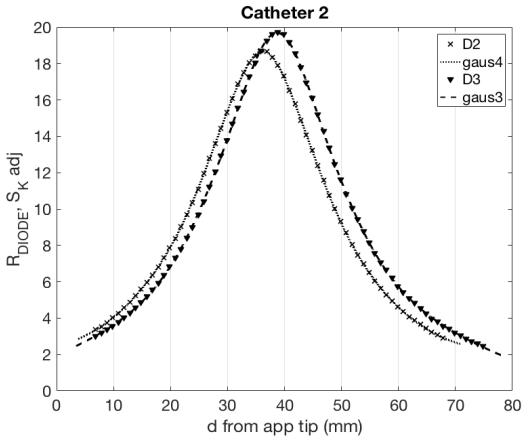
Catheter 2
D2
gaus4
D3
gaus3
R_{DIODE}, S_K adj
d from app tip (mm)

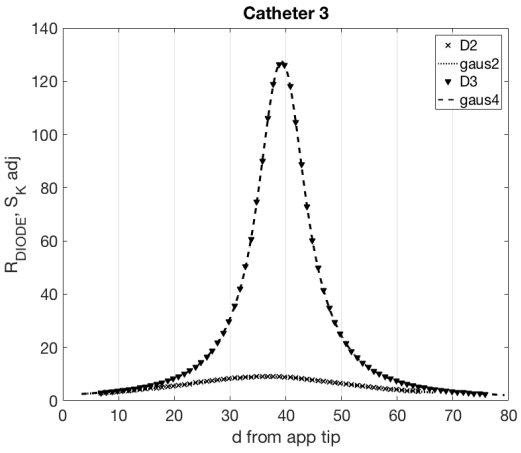
Catheter 3
D2
gaus2
D3
gaus4
R_{DIODE}, S_K adj
d from app tip

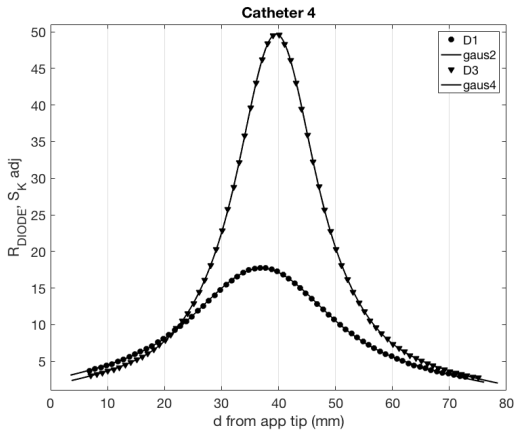
Catheter 4
D1
gaus2
D3
gaus4
R_{DIODE}, S_K adj
d from app tip (mm)

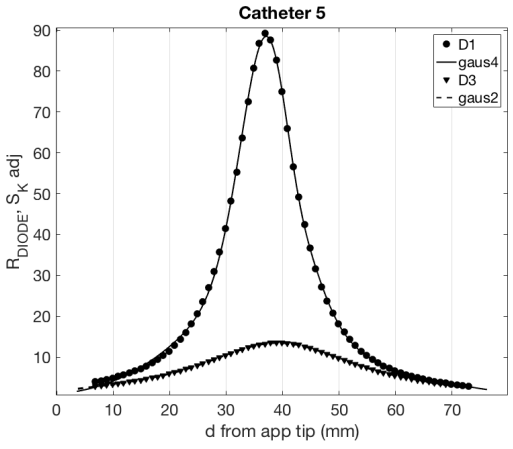
Catheter 5
D1
gaus4
D3
gaus2
R_{DIODE}, S_K adj
d from app tip (mm)

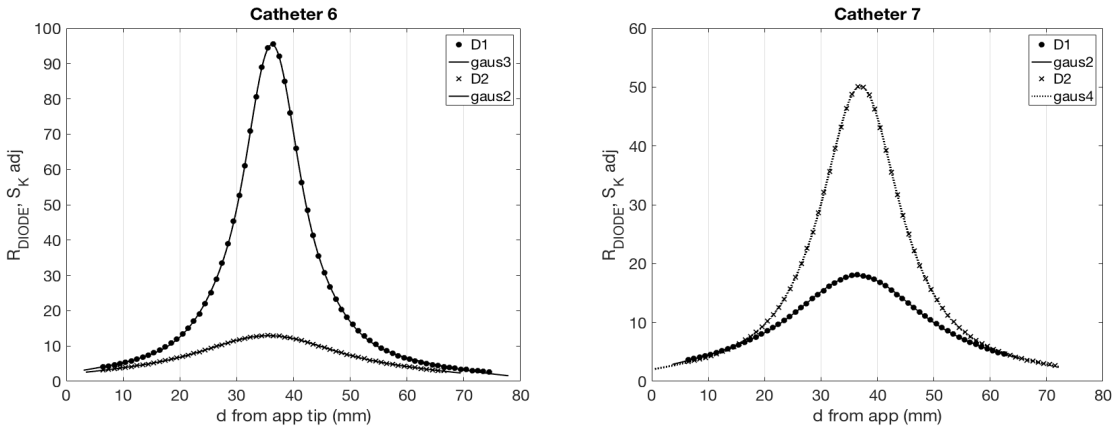

Figure 9.17 Multi-term Gaussian functions for each applicator catheter.

A schematic of the central channel calibration is shown in figure 9.18. The cross-sectional horizontal view (a) of the applicator shows the ^{192}Ir source (red sphere) in the central channel, and the three diodes around it. Diode response is plotted as a function of the source distance from the applicator tip (b), and in this case the diodes with the highest response (i.e., diodes 1 and 3) were used for position and dwell time reconstruction. The source in the first catheter dwell position is shown in the cross-sectional longitudinal view (c) with diodes 1 and 2 fixed around the applicator perimeter.

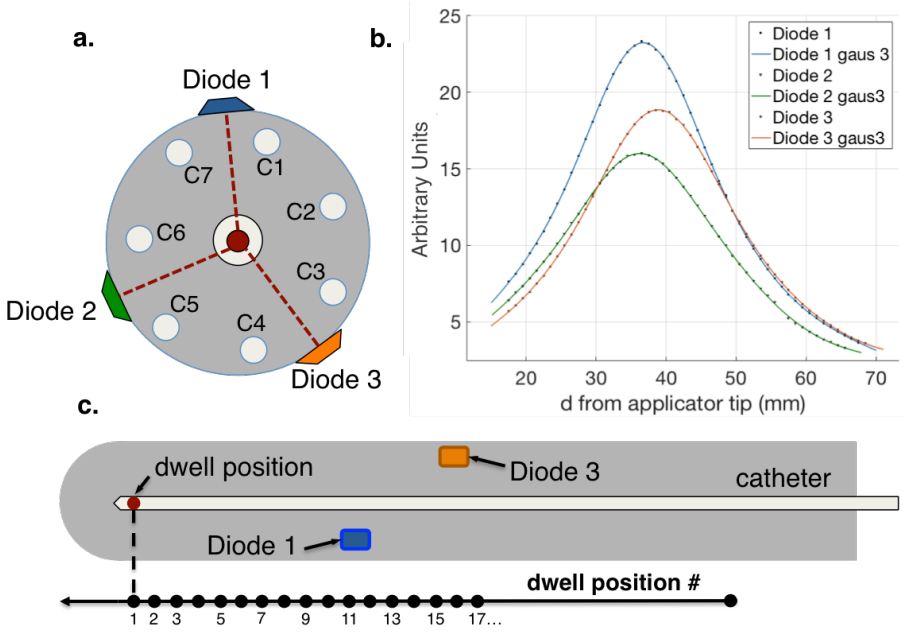

Figure 9.18 Schematic of the central channel calibration.

9.4.3 Application of method

Thus at any given treatment time the two higher responses R_1 and R_2 of the three diodes are divided by the source S_K and used to solve for the source position *d* in the given catheter, at the 95% CI as follows:

$$R_d\,(\mathrm{pC}) = a_1 \cdot e^{\left(\frac{d-b_1}{c_1}\right)^2} + a_2 \cdot e^{\left(\frac{d-b_2}{c_2}\right)^2} \ldots \qquad (9.2)$$

The diode with the high response will be used to derive two Gaussian solutions of the source position, and the diode with the lower response will be used to determine which of the two solutions is the real source position.

Figure 9.19 provides an example of dwell position reconstruction in a single catheter: catheter-specific Gaussian equations are solved for source position using the high-response diode, in this case diode 1 (D1), to derive positions (d_1, d_2) of (61, 14) and (65, 13.5) for the two dwell positions. Corresponding (d_1, d_2) are also determined for the low-response diode diode 2 (D2). In each case, the two D1 and D2 solutions that are closer together (i.e., d_2) for both dwell positions, shown on the lower part of the plot, indicate the real position of the source, and correspond to 14 and 13.5 mm from the applicator tip, respectively.

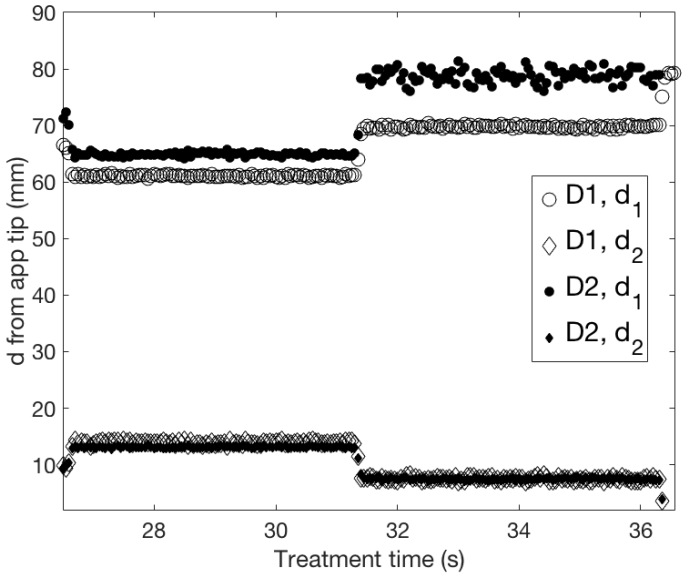

Figure 9.19 Example of the reconstruction of two dwell positions in a single catheter.

9.4.3.1 Discussion

All catheters are characterized by a high- and a low-response diode, with the exception of catheter 2 and the central catheter (as seen on the catheter-specific Gaussian fits in figure 9.17). Since the applicator has 7 peripheral channels and three diodes positioned between them, one catheter (i.e., Catheter 2) was characterized by a response of the same magnitude from two diodes. The dynamic range of the diodes in this case was to the order of 70 mm, as in the rest of the peripheral channels, and thus unaffected. The central catheter is located at a 14-mm depth on the axial plane, and since all diodes are positioned further away, the dynamic range was determined as 60 mm, and is thus lower than in the rest of the catheters.

In the case of source step size of ≤ 3 mm an increased uncertainty was observed in the reconstructed source position for dwell positions directly perpendicular to the diode's sensitive chip. Since the diode sensitive area is 1.5 x 1.5 mm^2 an identical diode response may result in two consecutive dwell positions. In this case the diode with the lower response, when positioned at a sufficient distance from the high-response diode, can be used to distinguish such dwell positions.

9.5 Source tracking system verification

The final step was to verify the system's ability to reconstruct ^{192}Ir dwell positions and times using the defined methodology. The first step of the verification was to test the feasibility of reconstructing equally spaced dwell positions and simple dwell times, followed by the retrospective delivery and reconstruction of 10 patient treatments previously administered at INT.

9.5.1 Verification using simple dwell positions

The calibration established in section 9.4 was tested and verified for multiple consecutive dwell positions within each catheter.

9.5.1.1 Methods

Seven and eight dwell positions were delivered in the peripheral and central catheters for a total range of 60 and 70 mm, respectively, at a step-size of 10 mm and a dwell time of 5 seconds in each position. Dwell positions and dwell times were reconstructed in each catheter using the described method. The absolute differences Δp and Δt between nominal and measured dwell positions and times, respectively, were then computed for every source position according to $\Delta p = p_{meas} - p_{nom}$ and $\Delta t = t_{meas} - t_{nom}$.

9.5.1.2 Results

Reconstructed positions ranged between 6.45 and 67.10 mm from the applicator tip in the peripheral catheters, and between 5.5 and 75.5 mm from the tip in the central catheter. Mean Δp and Δt were –0.2 ± 0.5 mm and -0.1 ± 0.1 s (k=1), respectively. 50% and 95% of absolute positional discrepancies were within 0.4 mm and 1.3 mm, respectively, whereas 50% and 95% of absolute time discrepancies were within 0.1 s and 0.4 s, respectively. The full list of mean discrepancies per catheter is reported in table 9.5.

Catheter Discrepancies		
CATHETER	**Δp (mm)**	**Δt (s)**
1	-0.2 ± 0.3	-0.2± 0.1
2	0.0± 0.4	-0.2± 0.1
3	-0.1± 0.4	-0.2± 0.1
4	-0.5± 0.6	-0.1± 0.2
5	-0.3± 0.5	-0.1± 0.0
6	-0.1± 0.5	-0.2± 0.2
7	-0.6± 0.5	-0.1± 0.1
Central	-0.1 ± 0.3	-0.1± 0.0
Mean ± SD	**-0.2 ± 0.5**	**-0.1 ± 0.1**

Table 9.5 Mean discrepancies in the reconstructed dwell position (mm) and dwell time (s) reported for each catheter inside the applicator.

The dwell time discrepancy ranged between 0 and -0.5 seconds. A discrepancy of ≤ 0.6 seconds is accounted for by the source transit, as shown in figure 9.13.

Dwell position discrepancies exceeding 1 mm were calculated in three instances in the peripheral catheters. In catheters 4 and 7 Δp of 1.6 and 1.7 mm were determined at a distance of ~67 mm from the applicator tip, where the accuracy of dwell position reconstruction was compromised by the SDD. In catheter 5 a Δp of 1.3 mm was determined at approximately 37 mm from the applicator tip, and is explained by the physical constraints of the detector discussed in section 9.4.3.1. A similar trend was found in the central catheter at 35.5 mm from the applicator tip, with the highest Δp of 0.7 mm reported in this position.

The results of the delivered verification plan are shown in figure 9.20, where the nominal values (pink) and the reconstructed positions (blue) are plotted with respect to treatment time (s). Individual dwell positions are visualized as plateaus in the source position i.e. distance from the tip of the applicator.

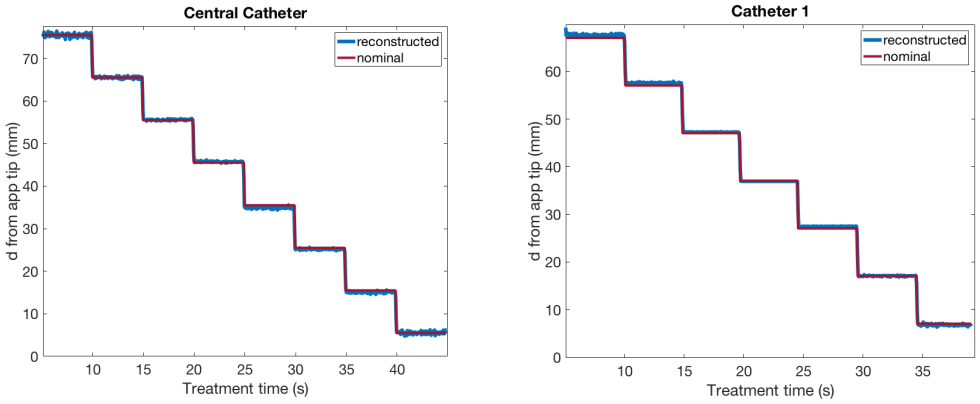

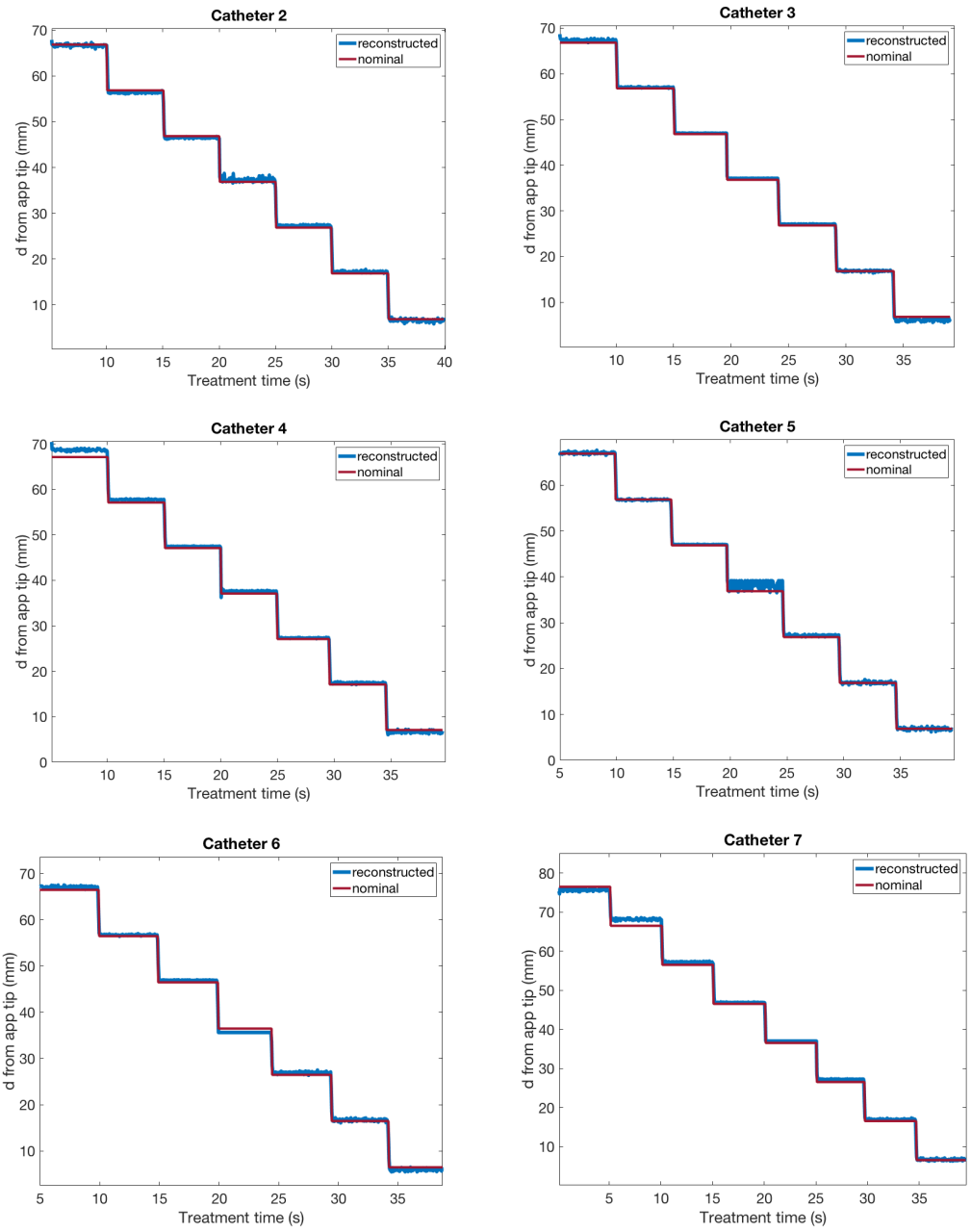

Figure 9.20 Reconstructed and nominal dwell positions for each delivered catheter.

9.5.1.3 Conclusions

The system has demonstrated sub-millimeter and sub-seconds positional accuracies, respectively, in the simple dwell position and dwell time plans. The next step of the study was to use increase treatment complexity by retrospectively delivering and verifying real patient plans.

9.5.2 Retrospective verification of patient treatments

A total of ten treatments previously administered to patients undergoing adjuvant vaginal cuff BT after hysterectomy at INT and employing the 30-mm MVC, were randomly selected from the database, and delivered and verified using the MVC system.

9.5.2.1 Methods

Ten BT treatments were delivered in-phantom (figure 9.21), and then reconstructed and compared to the nominal data provided by the TPS. Overall, 181 and 106 dwell positions for the source dwelling in the central and in the lateral catheters, respectively, were planned.

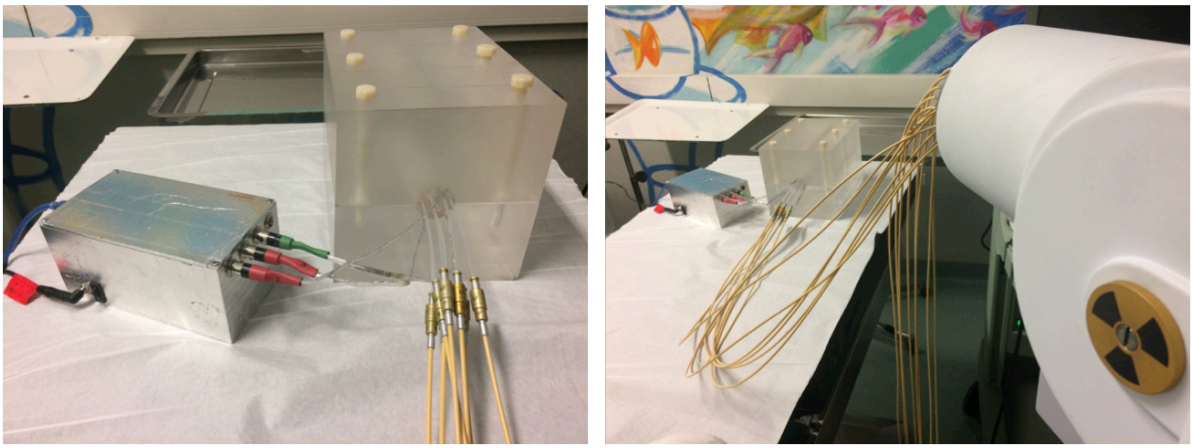

Figure 9.21 Setup of the retrospective patient plan delivery.

An example of a delivered plan is shown in figure 9.22. In this instance the central channel contains 10 dwell positions at 290-245 mm, and all seven peripheral channels are used to deliver three dwell positions at 288, 283, and 278 mm of varying dwell times. The total dwell times per channel are indicated at the top of the plan.

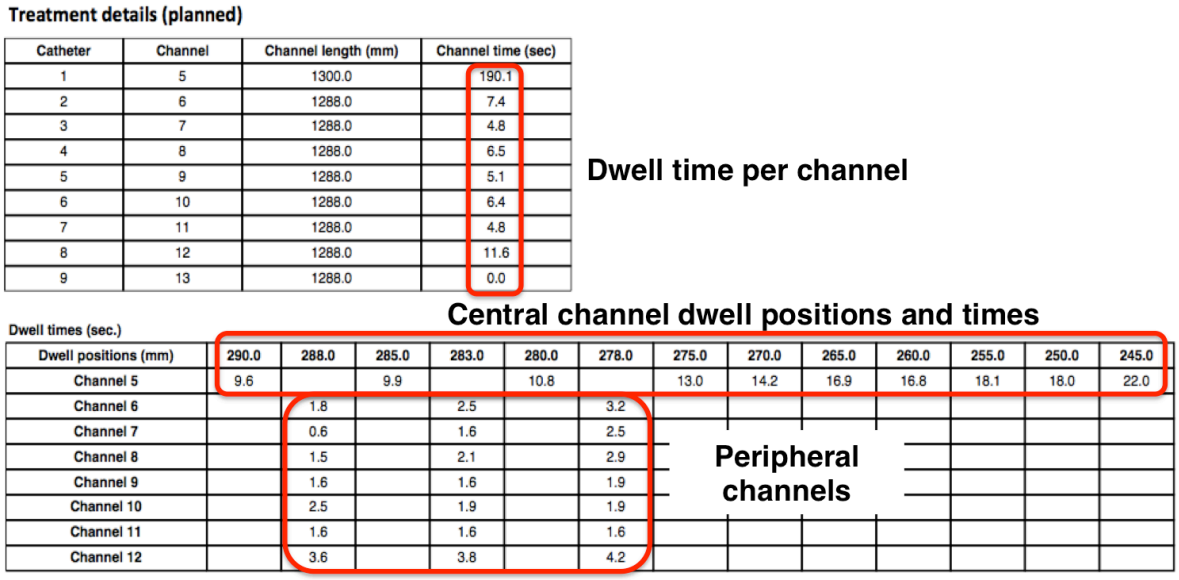

Treatment details (planned)

Catheter	Channel	Channel length (mm)	Channel time (sec)
1	5	1300.0	190.1
2	6	1288.0	7.4
3	7	1288.0	4.8
4	8	1288.0	6.5
5	9	1288.0	5.1
6	10	1288.0	6.4
7	11	1288.0	4.8
8	12	1288.0	11.6
9	13	1288.0	0.0

Dwell times (sec.)

Dwell positions (mm)	290.0	288.0	285.0	283.0	280.0	278.0	275.0	270.0	265.0	260.0	255.0	250.0	245.0
Channel 5	9.6		9.9		10.8		13.0	14.2	16.9	16.8	18.1	18.0	22.0
Channel 6		1.8		2.5		3.2							
Channel 7		0.6		1.6		2.5							
Channel 8		1.5		2.1		2.9							
Channel 9		1.6		1.6		1.9							
Channel 10		2.5		1.9		1.9							
Channel 11		1.6		1.6		1.6							
Channel 12		3.6		3.8		4.2							

Figure 9.22 An example of a patient plan retrospectively delivered and reconstructed using the system.

9.5.2.2 Results

An example of a plan reconstruction is shown in figure 9.23, where the reconstructed (blue) and nominal (pink) dwell positions with respect to treatment time are displayed for the central and six peripheral channels employed in the treatment. The treatment begins in the central catheter's furthest position from the applicator tip, delivering a total of 16 dwell positions. At 222.3 seconds the central channel delivery is completed (marked by the red arrow). The source then proceeds to two dwell positions 5 mm apart in peripheral channel 2 for 34.1 and 11.8 s in duration, respectively, and one dwell position in channel 3. The source then dwells in two positions in channel 4, 1 mm apart and lasting 33.7 s and 11.3 s, respectively, and then to one dwell position in consecutive channels 5, 6, and 7 for dwell times of 33.0 s, 21.7 s, and 33.3 s, respectively.

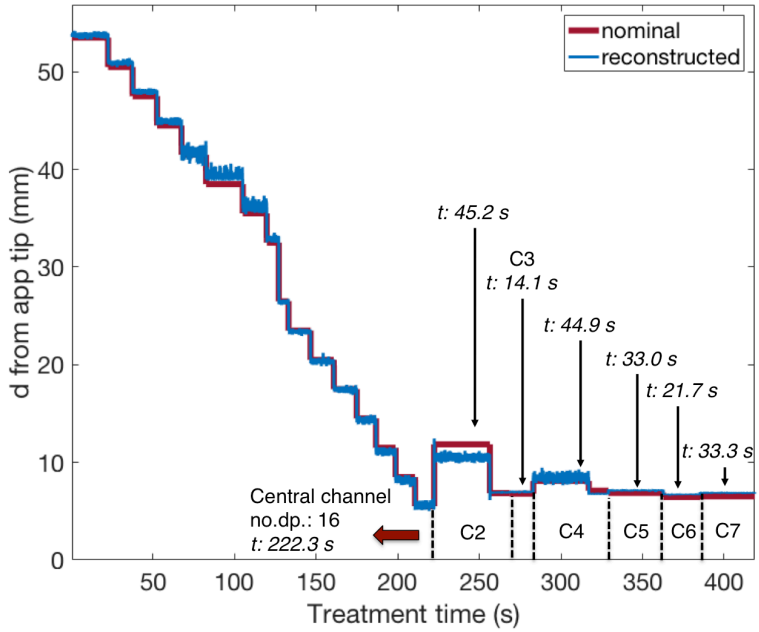

Figure 9.23 Example of treatment delivery verification with nominal positions and dwell times shown in pink, and the reconstructed plan shown in blue.

Discrepancies between the nominal and reconstructed dwell positions and dwell times for all 10 delivered plans are plotted in figure 9.24, with each data point corresponding to one dwell position. The mean positional discrepancy was determined as 0.2 ± 0.4 mm and 0.0 ± 0.8 mm (k=1) for the central and lateral catheters, respectively. The mean dwell time discrepancies are -0.1 ± 0.2 s and -0.0 ± 0.1 s (k=1) for the central and lateral catheters, respectively. 50% and 95% of absolute positional discrepancies |Δp| were < 0.3 mm and < 0.8 mm, respectively, for the source dwelling in the central catheter, and < 0.5 mm and < 1.5 mm, respectively, for the source dwelling in the peripheral catheters. Overall, 96.2 and 77.9% of absolute positional discrepancies were < 1 mm for the central and peripheral channels, respectively.

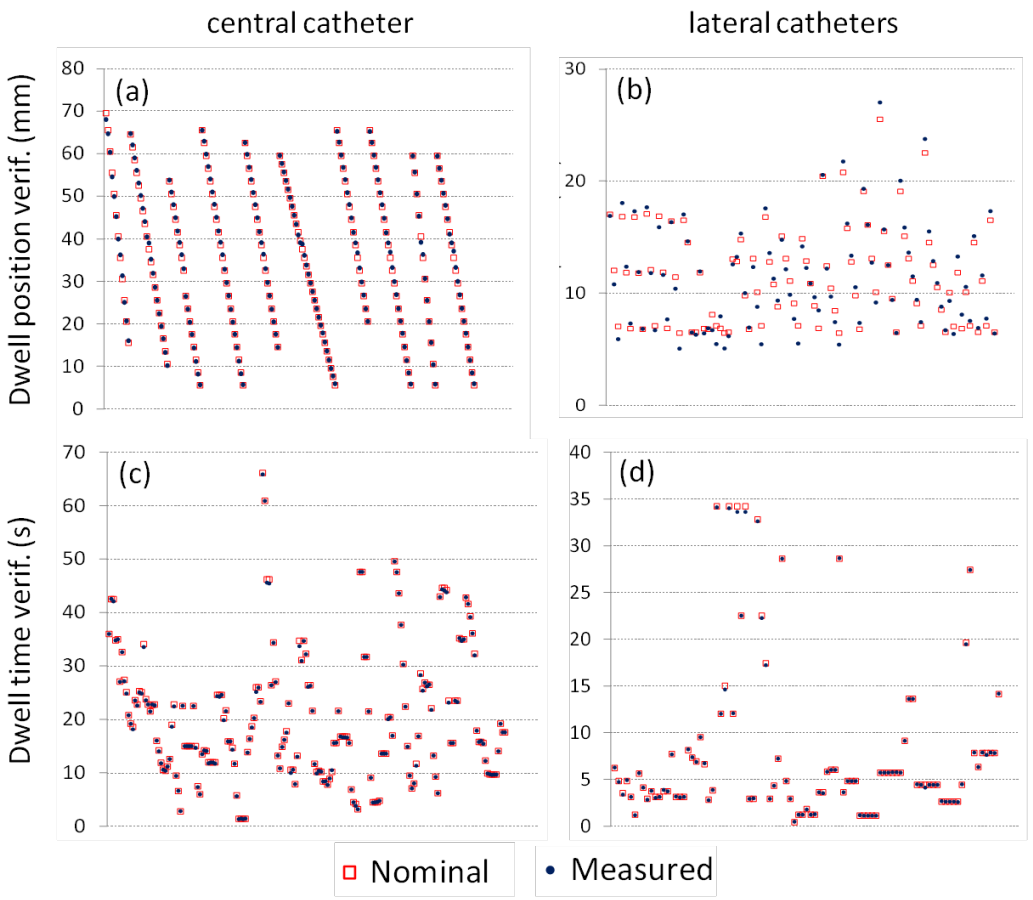

Figure 9.24 Planned (red squares) and measured (blue dots) dwell positions (a) and times (c) for the central catheter, respectively, and between planned and measured dwell positions (b) and times (d) for the lateral catheters, respectively, in the 10 delivered clinical patient plans.

50% and 95% of absolute dwell time discrepancies |Δt| were < 0.05 s and < 0.40 s, respectively, for the source dwelling in the central catheter, and < 0.05 s and < 0.20 s, respectively, for the source dwelling in the peripheral catheters.

9.5.2.3 Discussion

In this study, an innovative prototype of a MVC applicator with embedded diode detectors was produced. Preliminary measurements on a "simple" and on ten different clinical treatment plans have demonstrated the MVC system's ability to monitor the HDR source throughout the entire dose delivery phase, providing *in vivo* and real time QA of the delivered treatment by comparing it to the prescribed plan. The system is in principle able to detect errors in dwell position and dwell times, including

spontaneous afterloader malfunction, incorrect applicator and indexer lengths, mistakes in transfer tube connections, source calibration, and administration of the incorrect treatment plan. The proposed pre-calibrated MVC system is the first prototype of the MVC applicator with embedded diode detectors that is able to provide dwell positions and times in real time with generally sub-mm and sub-second accuracy.

The MVC system can be pre-calibrated via a relatively easy method, and source positions and times can be obtained in real time without any assumptions or particular dose distribution calculations within the applicator/patient. Source positions are constrained along the central and peripheral catheters by the applicator, and the diodes have fixed positions with respect to the catheters. Thus, for each possible source position in one of the eight treatment channels, a unique solution exists from the combination of the two dosimeters with the highest responses. This solution can be determined experimentally prior to the use of the applicator and is valid without further recalibration in the case of stable diode response. Moreover, specific corrections for the possible energy and angular dependences of the diodes were not necessary, because the overall diode response was taken as reference and intrinsically modeled with the multi-term Gaussian functions.

This is different to systems that are not built-in with the applicator, such as 2D arrays [154] or EPIDs [171], where more complex assumptions, pre-calibrations and calculations have to be performed to accurately reconstruct source positions inside the patient (for example complex algorithms, such as triangulation, and accounting for the response lag in the case of EPIDs). Source localization performed using plastic scintillation detectors benefits from their high sensitivity, angular and energy independence (as opposed to diodes), and small size that allows them to be incorporated into the treatment procedure. However their biggest drawback is the mandatory stem signal correction.

For the proposed system, it is imperative that calibration takes place in the same conditions that are present during treatment. Moreover, the diodes are incorporated directly over the dose delivery instrument, eliminating the need of additional steps in the existing treatment procedure for the radiation oncologist. Prior to patient irradiation the diode detectors must simply be connected to the readout system. To fully integrate the system into the QA workflow, the readout system should be connected with the afterloader treatment console for direct comparison between nominal and measured (calculated directly on the console) dwell positions and times.

Wang et al. (2014) [168] and Guiral et al. (2016) [167], who also equipped a commercial MVC applicator with four [GaN-based] dosimeters, presented results that mainly address the discrepancies within the central catheter. Mean dwell position and time discrepancies presented in the above studies are comparable to the results obtained with the diode MVC system. In particular, the discrepancies were -0.11 ± 0.7 mm and 0.2 ± 0.4 mm (k=1) for dwell positions in Guiral et al. (2016) and in our study, respectively, and 0.05 ± 0.09 s and -0.1 ± 0.2 s (k=1) for dwell times, respectively. In our study, it was additionally shown that comparable accuracies can also be obtained for lateral catheters on ten clinical treatments, with resulting dwell position and time discrepancies of 0.0 ± 0.8 mm and -0.0 ± 0.1 s (k=1), respectively.

This study clearly shows potential for future use of the proposed system in the clinical routine. The diodes can be integrated into commercially available MVC applicators of any diameter, utilizing applicators that are already clinically approved and familiar to hospital staff. A source detection range of the proximal 60-70 mm of the vagina is sufficient for the majority of clinical applications of adjuvant vaginal cuff BT following hysterectomy, where the proximal 3-5 cm of the vagina are normally treated [172]. An increased number of diodes and their optimal positioning over the applicator could further extend the range. The temporal and spatial resolutions are also in principle sufficient, and would already allow the detection of significant delivery errors. A thorough evaluation of the system's ability to detect specific treatment errors will be conducted in the future.

An intrinsic limitation of the developed method is that the source tracking system is incorporated directly on the MVC applicator, and thus is not able to detect shifts in applicator position and rotation throughout the treatment, in particular with respect to the planned target volume and the surrounding organs at risk. The use of the system will therefore validate that the delivered treatment is in accordance with the planned one, but no conclusions can be drawn about the delivered dose distribution. *In vivo* dose measurements in the urethra or rectum [97, 114, 117, 173-176] will be necessary to provide a comprehensive verification of the delivered treatment. Further *in vivo* measurements are required to validate a potential combination of dosimetry and source tracking methods.

9.6 Conclusions and recommendations

The applicator prototype with embedded diodes for HDR source tracking has shown great potential for both treatment delivery and real-time BT treatment verification by demonstrating a sub-second temporal resolution for dwell time verification and a sub-millimetric positional accuracy in 96.2 and 77.9% of reconstructed dwell positions in the central and peripheral channels, respectively.

The proposed system is able to detect treatment errors relating to source position and dwell time inside the applicator, such as the administration of the wrong treatment plan, spontaneous afterloader malfunction (altering the source step size or dwell time), mistake in the indicated indexer length, and systematic errors such as those occurring as a result of incorrect source calibration.

The MVC HDR BT verification system can be improved in future studies by placing additional diodes on the applicator surface as well as positioning detectors at a higher distance from one another on the longitudinal plane to decrease uncertainties in close proximity to the diode's sensitive volume. Future studies to evaluate the MVC system's

ability to detect specific treatment errors and to investigate the possible combination of the MVC system with *in vivo* dosimetry methods will be conducted in the future.

Chapter 10

Retrospective and real-time dosimetry: recommendations and conclusions

10.1 Retrospective dosimetry

Solid-state semiconductor dosimetry has been successfully applied to the visualization and spatially resolved dose rate measurement of intact sediment samples, both artificially produced and natural samples, from key archeological and hominin sites. The proposed Timepix methodology allows the measurement of samples resinated as per micromorphology procedure, preserving the microstratigraphic context of the sample during burial. A superior spatial resolution of sample environmental dose rates that is well within the 3-mm beta particle range has been achieved.

High dose rate inhomogeneity has been shown within the sample from the Liang Bua Cave, while dose rates within the Denisova Cave sample have demonstrated higher spatial uniformity and a normal dose rate distribution. Based on the results, radioemitter inhomogeneity may affect sample age by up to 70%.

Future studies employing the Timepix for sediment measurement have the potential to achieve a 3D visualization of dose rates within samples by measuring thinner slices. Dose rate calibration can be improved to further minimize dose rate conversion errors. Energy calibration of the Timepix can be applied to evaluate the energy deposition of detected particles, and explore the use of this feature for isotope identification. Furthermore, Timepix measurement results can be modeled using the Geant4 simulation platform to assess the effect on the dose absorbed by the detector grains, and obtain a distribution of singe-grain ages.

This study is an important step towards improving the accuracy and precision of chronology in both geological and archeological contexts, which can ultimately deepen our knowledge on the evolution and dispersion of humankind.

10.2 Real-time dosimetry

The combination of *in vivo* dosimetry and HDR source tracking systems investigated in this thesis have the potential to detect errors that would remain unknown without real-time or post-treatment verification. The precision of the source tracking system, which is able to provide excellent QA of the BT source throughout the entire procedure, in combination with point-measurements of absorbed dose in OARs, can be used in real time to prevent or provide awareness of a multitude of potential missteps in gynecological HDR BT treatments. Epi diodes in the proposed HDR source verification system are able to detect errors such as source calibration, spontaneous afterloader malfunctions, incorrect applicator or indexer lengths, and misconnections of transfer tubes. MO*Skin* dosimeters assembled over the DRP can be used to alert of any dose discrepancies as a result of organ and/or applicator motion. Both of the systems can verify that the correct plan is being delivered to the patient, and can be easily incorporated into the existing clinical treatment flow.

IVD can identify errors resulting from anatomical differences, such as inter- or intra-fraction organ swelling or motion, however only if these directly affect the dose delivered at the points of measurement. In the cases that the doses in those regions are affected, the introduction of post-treatment imaging would provide a more comprehensive quality assurance of the delivered treatment, allowing post-treatment reconstruction of the delivered dose distribution. The three components of comprehensive HDR BT treatment QA are shown in figure 10.1.

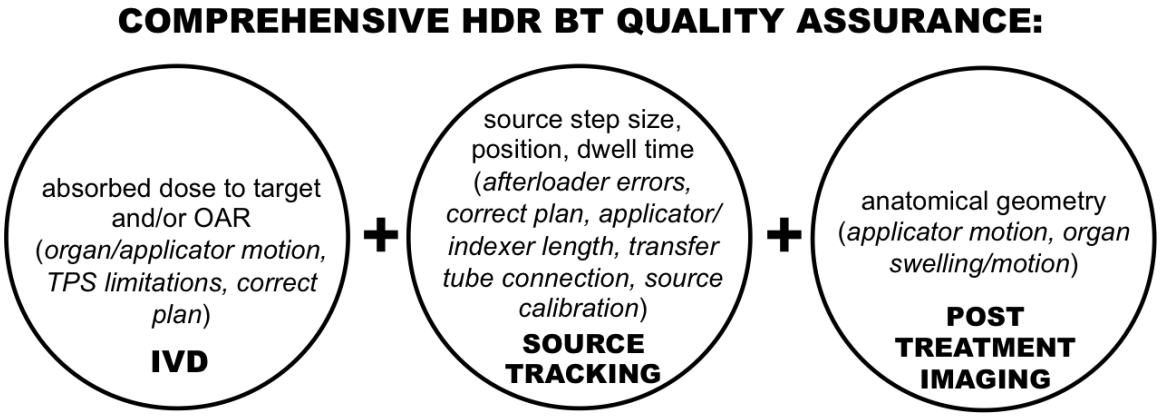

Figure 10.1 Three components of comprehensive HDR BT QA.

Future applications of the DRP procedure for IVD are recommended to employ the recently developed wireless MO*Skin* reader system, allowing readout without the necessity of the long cables. Moreover, delivered and planned rectal wall dose discrepancies should be evaluated in real-time, as opposed to the post-treatment evaluation performed in this study. A newly assembled MVC system that employs a higher number of diodes with optimized diode positioning is recommended to test system ability to detect specific treatment errors. Studies of real-time dose and HDR source monitoring should be implemented and evaluated in future studies to determine its efficacy in alerting of dose discrepancies above the accepted error margin.

It is important that the frequency and types of treatment errors are shared and discussed among radiotherapy staff, so that these results can lead to an evolution of

quality management systems in the clinic, and contribute to the reduction of uncertainties and potential systematic errors. This in turn will improve cancer care for the patient, and provide another stepping-stone in our battle with cancer.

10.3 Final conclusions

In this thesis, solid-state semiconductor dosimetry has united the fields of geoscience and medical physics. Radiation measurement techniques have been developed both for sediment dating, by applying the Timepix pixelated detector, and for radiotherapy treatment verification, by applying MO*Skin* and diode detectors. Using these methods, spatially resolved sediment dose rates have the potential to improve the accuracy and precision of dating and allow a better understanding of H. sapiens' past, while real time radiotherapy treatment verification has the potential to improve the quality and longevity of life for present-day and future H. sapiens.

Bibliography

1. King W: The reputed fossil man of the Neanderthal. *Quarterly Review of Science* 1864, 1:88-97.

2. Dirks PHGM, Roberts EM, Hilbert-Wolf H, Kramers JD, Hawks J, Dosseto A, Duval M, Elliott M, Evans M, Grün R, et al: The age of Homo naledi and associated sediments in the Rising Star Cave, South Africa. *eLife* 2017, 6:e24231.

3. Vernot B, Tucci S, Kelso J, Schraiber JG, Wolf AB, Gittelman RM, Dannemann M, Grote S, McCoy RC, Norton H, et al: Excavating Neandertal and Denisovan DNA from the genomes of Melanesian individuals. *Science* 2016.

4. Reich D, Green RE, Kircher M, Krause J, Patterson N, Durand EY, Viola B, Briggs AW, Stenzel U, Johnson PLF, et al: Genetic history of an archaic hominin group from Denisova Cave in Siberia. *Nature* 2010, 468:1053.

5. Omran AR: The Epidemiologic Transition: A Theory of the Epidemiology of Population Change. *The Milbank Quarterly* 2005, 83:731-757.

6. Horiuchi S: Health and mortality: issues of global concern. *New York: United Nations* 1999. *Proceedings of the Symposium on Health and Mortality, Brussels, 19-22 November* 1997: 54-71.

7. National Cancer Institute. Cancer Statistics. https://www.cancer.gov/about-cancer/understanding/statistics. Accessed 14/01/2019.

8. Daniels F, Boyd CA, Saunders DF: Thermoluminescence as a Research Tool. *Science* 1953, 117:343-349.

9. Knoll GF: *Radiation Detection and Measurement.* 3rd Edition. John Wiley & Sons; 2000.

10. International Organization for Standardization (ISO). *Radiological protection — Medical electron accelerators — Requirements and recommendations for shielding design and evaluation*. ISO/TC 85/SC 2. ISO 16645:2016.

11. Aitken MJ, Mejdahl V: *Thermoluminescence dating.* Academic press London; 1985.

12. Aitken MJ: *Introduction to optical dating: the dating of Quaternary sediments by the use of photon-stimulated luminescence.* Clarendon Press; 1998.

13. Aitken MJ: *Science-based dating in archaeology.* Routledge; 2014.

14. Feathers JK: Luminescence dating and modern human origins. *Evolutionary Anthropology* 1996, 5:25-36.

15. Feathers JK: Use of luminescence dating in archaeology. *Measurement Science and Technology* 2003, 14:1493.

16. Fleming S, Sutton S: Thermoluminescence Techniques in Archeology. *Physics Today* 1981, 34:66.

17. Wintle AG: Fifty years of luminescence dating. *Archaeometry* 2008, 50:276-312.

18. Huntley DJ, Godfrey-Smith DI, Thewalt MLW: Optical dating of sediments. *Nature* 1985, 313:105-107.

19. Hütt G, Jaek I: Infrared stimulated photoluminescence dating of sediments. *Ancient TL* 1989, 7:48-51.

20. Roberts RG, Jacobs Z, Li B, Jankowski NR, Cunningham AC, Rosenfeld AB: Optical dating in archaeology: thirty years in retrospect and grand challenges for the future. *Journal of Archaeological Science* 2015, 56:41-60.

21. Duller GAT: Luminescence dating of quaternary sediments: recent advances. *Journal of Quaternary Science* 2004, 19:183-192.

22. Thomsen KJ, Murray AS, Jain M, Bøtter-Jensen L: Laboratory fading rates of various luminescence signals from feldspar-rich sediment extracts. *Radiation Measurements* 2008, 43:1474-1486.

23. Li B, Jacobs Z, Roberts R, Li S: Extending the age limit of luminescence dating using the dose-dependent sensitivity of MET-pIRIR signals from K-feldspar. *Quaternary Geochronology* 2013, 17: 55-67.

24. Jain M: Extending the dose range: Probing deep traps in quartz with 3.06eV photons. *Radiation Measurements* 2009, 44:445-452.

25. Ankjærgaard C, Guralnik B, Buylaert JP, Reimann T, Yi SW, Wallinga J: Violet stimulated luminescence dating of quartz from Luochuan (Chinese loess plateau): Agreement with independent chronology up to ~600 ka. *Quaternary Geochronology* 2016, 34:33-46.

26. Wang XL, Lu YC, Wintle AG: Recuperated OSL dating of fine-grained quartz in Chinese loess. *Quaternary Geochronology* 2006, 1:89-100.

27. Galbraith RF, Roberts RG, Laslett GM, Yoshida H, Olley JM: Optical dating of single and multiple grains of quartz from Jinmium rock shelter, northern Australia: Part I, experimental design and statistical models. *Archaeometry* 1999, 41:339-364.

28. Murray AS, Roberts RG: Measurement of the equivalent dose in quartz using a regenerative-dose single-aliquot protocol. *Radiation Measurements* 1998, 29:503-515.

29. Murray AS, Wintle AG: Luminescence dating of quartz using an improved single-aliquot regenerative-dose protocol. *Radiation measurements* 2000, 32:57-73.

30. Duller GA, Murray AS: Luminescence dating of sediments using individual mineral grains. *Geologos* 2000, 5:87-106.

31. Duller GAT: Single-grain optical dating of Quaternary sediments: why aliquot size matters in luminescence dating. *Boreas* 2008, 37:589-612.

32. Jacobs Z, Roberts RG: Advances in optically stimulated luminescence dating of individual grains of quartz from archeological deposits. *Evolutionary Anthropology* 2007, 16:210-223.

33. Prescott JR, Hutton JT: Cosmic ray contributions to dose rates for luminescence and ESR dating: Large depths and long-term time variations. *Radiation Measurements* 1994, 23:497-500.

34. Adamiec G, Aitken MJ: Dose-rate conversion factors: update. *Ancient TL* 1998, 16:37-50.

35. Olley JM, Murray A, Roberts RG: The effects of disequilibria in the uranium and thorium decay chains on burial dose rates in fluvial sediments. *Quaternary Science Reviews* 1996, 15:751-760.

36. Stokes S, Ingram S, Aitken M, Sirocko F, Anderson R, Leuschner D: Alternative chronologies for Late Quaternary (Last Interglacial–Holocene) deep sea sediments via optical dating of silt-sized quartz. *Quaternary Science Reviews* 2003, 22:925-941.

37. Duller G: *Luminescence Dating : Guidelines on using luminescence dating in archaeology.* English Heritage; 2008.

38. Guérin G, Mercier N, Adamiec G: Dose-rate conversion factors: update. *Ancient TL* 2011, 29:5-8.

39. Galbraith R: A note on OSL age estimates in the presence of dose rate heterogeneity. *Ancient TL* 2015, 33:31-34.

40. Jacobs Z, Wintle AG, Roberts RG, Duller GA: Equivalent dose distributions from single grains of quartz at Sibudu, South Africa: context, causes and consequences for optical dating of archaeological deposits. *Journal of Archaeological Science* 2008, 35:1808-1820.

41. Jacobs Z, Duller GAT, Wintle AG: Optical dating of dune sand from Blombos Cave, South Africa: II—single grain data. *Journal of Human Evolution* 2003, 44:613-625.

42. Jacobs Z, Duller GAT, Wintle AG: Interpretation of single grain De distributions and calculation of De. *Radiation Measurements* 2006, 41:264-277.

43. Guérin G, Mercier N, Nathan R, Adamiec G, Lefrais Y: On the use of the infinite matrix assumption and associated concepts: A critical review. *Radiation Measurements* 2012, 47:778-785.

44. Mayya YS, Morthekai P, Murari MK, Singhvi AK: Towards quantifying beta microdosimetric effects in single-grain quartz dose distribution. *Radiation Measurements* 2006, 41:1032-1039.

45. Allison J, Amako K, Apostolakis J, Araujo H, Dubois PA, Asai M, Barrand G, Capra R, Chauvie S, Chytracek R, et al: Geant4 developments and applications. *IEEE Transactions on Nuclear Science* 2006, 53:270-278.

46. Agostinelli S, Allison J, Amako K, Apostolakis J, Araujo H, Arce P, Asai M, Axen D, Banerjee S, Barrand G, et al: Geant4—a simulation toolkit. *Nuclear Instruments and Methods in Physics Research Section A: Accelerators, Spectrometers, Detectors and Associated Equipment* 2003, 506:250-303.

47. Martin L, Mercier N, Incerti S, Lefrais Y, Pecheyran C, Guérin G, Jarry M, Bruxelles L, Bon F, Pallier C: Dosimetric study of sediments at the beta dose rate scale: Characterization and modelization with the DosiVox software. *Radiation Measurements* 2015, 81:134-141.

48. Martin L, Fang F, Mercier N, Incerti S, Grün R, Lefrais Y: 2D modelling: A Monte Carlo approach for assessing heterogeneous beta dose rate in luminescence and ESR dating: Paper I, theory and verification. *Quaternary Geochronology* 2018, 48:25-37.

49. Fang F, Martin L, Williams IS, Brink F, Mercier N, Grün R: 2D modelling: A Monte Carlo approach for assessing heterogeneous beta dose rates in luminescence and ESR dating: Paper II, application to igneous rocks. *Quaternary Geochronology* 2018, 48:195-206.

50. Nathan RP, Thomas PJ, Jain M, Murray AS, Rhodes EJ: Environmental dose rate heterogeneity of beta radiation and its implications for luminescence dating: Monte Carlo modelling and experimental validation. *Radiation Measurements* 2003, 37:305-313.

51. Cunningham AC, DeVries DJ, Schaart DR: Experimental and computational simulation of beta-dose heterogeneity in sediment. *Radiation Measurements* 2012, 47:1060-1067.

52. Rufer D, Preusser F: Potential of autoradiography to detect spatially resolved radiation patterns in the context of trapped charge dating. *Geochronometria* 2009, 34:1-13.

53. Schmidt C, Rufer D, Preusser F, Krbetschek M, Hilgers A: The assessment of radionuclide distribution in silex by autoradiography in the context of dose

rate determination for thermoluminescence dating. *Archaeometry* 2013, 55:407-422.

54. Kalchgruber R, Fuchs M, Murray AS, Wagner GA: Evaluating dose-rate distributions in natural sediments using α-Al2O3:C grains. *Radiation Measurements* 2003, 37:293-297.

55. Wagner GA, Glasmacher UA, Greilich S: Spatially resolved dose-rate determination in rocks and ceramics by neutron-induced fission tracks: fundamentals. *Radiation measurements* 2005, 40:26-31.

56. Godfrey-Smith DI, Scallion P, Clarke ML: Beta dosimetry of potassium feldspars in sediment extracts using imaging microprobe analysis and beta counting. *Geochronometria* 2005, 24:7-12.

57. Jankowski NR, Jacobs Z, Goldberg P: Optical dating and soil micromorphology at MacCauley's Beach, New South Wales, Australia. *Earth Surface Processes and Landforms* 2015, 40:229-242.

58. Baril MR: CCD imaging of the infra-red stimulated luminescence of feldspars. *Radiation Measurements* 2004, 38:81-86.

59. Schmidt C, Pettke T, Preusser F, Rufer D, Kasper HU, Hilgers A: Quantification and spatial distribution of dose rate relevant elements in silex used for luminescence dating. *Quaternary Geochronology* 2012, 12:65-73.

60. Lau JH: *Flip chip technologies.* McGraw-Hill New York; 1996.

61. Teyssier C, Bouchami J, Dallaire F, Idarraga J, Leroy C, Pospisil S, Solc J, Scallon O, Vykydal Z: Performance of the Medipix and Timepix devices for the recognition of electron-gamma radiation fields. *Nuclear Instruments and Methods in Physics Research Section A: Accelerators, Spectrometers, Detectors and Associated Equipment* 2011, 650:92-97.

62. Llopart X, Ballabriga R, Campbell M, Tlustos L, Wong W: Timepix, a 65k programmable pixel readout chip for arrival time, energy and/or photon counting measurements. *Nuclear Instruments and Methods in Physics Research Section A: Accelerators, Spectrometers, Detectors and Associated Equipment* 2007, 581:485-494.

63. Holy T, Heijne E, Jakubek J, Pospisil S, Uher J, Vykydal Z: Pattern recognition of tracks induced by individual quanta of ionizing radiation in Medipix2 silicon detector. *Nuclear Instruments and Methods in Physics Research Section*

A: Accelerators, Spectrometers, Detectors and Associated Equipment 2008, 591:287-290.

64. Turecek D, Holy T, Jakubek J, Pospisil S, Vykydal Z: Pixelman: a multi-platform data acquisition and processing software package for Medipix2, Timepix and Medipix3 detectors. *Journal of Instrumentation* 2011, 6:C01046.

65. George S: Dosimetric applications of hybrid pixel detectors. *Doctor of Philosophy thesis, School of Physics, University of Wollongong* 2015.

66. Idarraga J: MAFalda, an Analysis Framework for Pixel Detectors 2012. https: //twiki.cern.ch/twiki/bin/view/Main/MAFalda.

67. Murphy CP: *Thin section preparation of soils and sediments.* A.B. Academic Publishers, Herts, UK; 1986.

68. Bøtter-Jensen L, Mejdahl V: Determination of potassium in feldspars by beta counting using a GM multicounter system. *Nuclear Tracks and Radiation Measurements (1982)* 1985, 10:663-666.

69. Bøtter-Jensen L, Mejdahl V: Assessment of beta dose-rate using a GM multicounter system. *International Journal of Radiation Applications and Instrumentation Part D Nuclear Tracks and Radiation Measurements* 1988, 14:187-191.

70. Kalchgruber R, Göksu H, Hochhäuser E, Wagner G: Monitoring environmental dose rate using Risø TL/OSL readers with built-in sources: recommendations for users. *Radiation measurements* 2002, 35:585-590.

71. Jacobs Z, Roberts RG: An improved single grain OSL chronology for the sedimentary deposits from Diepkloof Rockshelter, Western Cape, South Africa. *Journal of Archaeological Science* 2015, 63:175-192.

72. Morwood M, Jungers W: Paleoanthropological Research at Liang Bua, Flores, Indonesia. *Journal of Human Evolution* 2009, 57:437-648.

73. Morwood MJ, Soejono RP, Roberts RG, Sutikna T, Turney CS, Westaway KE, Rink WJ, Zhao J-X, van den Bergh GD, Due RA: Archaeology and age of a new hominin from Flores in eastern Indonesia. *Nature* 2004, 431:1087.

74. Sutikna T, Tocheri MW, Morwood MJ, Saptomo EW, Awe RD, Wasisto S, Westaway KE, Aubert M, Li B, Zhao JX: Revised stratigraphy and chronology for Homo floresiensis at Liang Bua in Indonesia. *Nature* 2016, 532:366-369.

75. Derevianko A, Shunkov M, Agadjanian A, Baryshnikov G, Malaeva E, Ulianov V, Kulik N, Postnov A, Anoikin A: Paleoenvironment and Paleolithic human occupation of Gorny Altai: subsistence and adaptation in the vicinity of Denisova Cave. *Institute of Archaeology and Ethnography, Siberian Branch, Russian Academy of Sciences Press* 2003.

76. Slon V, Hopfe C, Weiß CL, Mafessoni F, De la Rasilla M, Lalueza-Fox C, Rosas A, Soressi M, Knul MV, Miller R, et al: Neandertal and Denisovan DNA from Pleistocene sediments. *Science* 2017, 356:605-608.

77. Australian Institute of Health and Welfare 2017. *Cancer in Australia 2017*. Cancer series no.101. Cat. no. CAN 100. Canberra: AIHW.

78. Ferrer M, Suárez JF, Guedea F, Fernández P, Macías V, Mariño A, Hervas A, Herruzo I, Ortiz MJ, Villavicencio H: Health-related quality of life 2 years after treatment with radical prostatectomy, prostate brachytherapy, or external beam radiotherapy in patients with clinically localized prostate cancer. *International Journal of Radiation Oncology* Biology* Physics* 2008, 72:421-432.

79. Suchowerska N, Jackson M, Lambert J, Yin YB, Hruby G, McKenzie DR: Clinical trials of a urethral dose measurement system in brachytherapy using scintillation detectors. *International Journal of Radiation Oncology* Biology* Physics* 2011, 79:609-615.

80. Gerbaulet A, Pötter R, Mazeron JJ, Meertens H, Van Limbergen, E: *The GEC ESTRO Handbook of Brachytherapy*. ESTRO, Brussels; 2002.

81. Sakelliou L, Baltas D, Zamboglou N: *The physics of modern brachytherapy for oncology.* CRC Press; 2006.

82. Nath R, Anderson LL, Luxton G, Weaver KA, Williamson JF, Meigooni AS: Dosimetry of interstitial brachytherapy sources: recommendations of the AAPM Radiation Therapy Committee Task Group No. 43. *Medical physics* 1995, 22:209-234.

83. Rivard MJ, Coursey BM, DeWerd LA, Hanson WF, Saiful Huq M, Ibbott GS, Mitch MG, Nath R, Williamson JF: Update of AAPM Task Group No. 43 Report: A revised AAPM protocol for brachytherapy dose calculations. *Medical physics* 2004, 31:633-674.

84. Thomadsen BR, Williamson JF, Rivard MJ, Meigooni AS: Anniversary paper: past and current issues, and trends in brachytherapy physics. *Medical physics* 2008, 35:4708-4723.

85. Khoo VS, Dearnaley DP, Finnigan DJ, Padhani A, Tanner SF, Leach MO: Magnetic resonance imaging (MRI): considerations and applications in radiotherapy treatment planning. *Radiotherapy and Oncology* 1997, 42:1-15.

86. Burnet NG, Thomas SJ, Burton KE, Jefferies SJ: Defining the tumour and target volumes for radiotherapy. *Cancer Imaging* 2004, 4:153.

87. *MicroSelectron HDR User Manual*. 292515ENG-00, Stockholm, Sweden: Nucletron, an Elekta company, Elekta AB.

88. US Nuclear Regulatory Commission: *A risk-informed approach to understanding human error in radiation therapy*. United States; 2017.

89. Felder S, Morley L, Ng E, Chan K, Ballantyne H, Di Tomasso A, Borg J, Bissonnette J-P, Breen S, Waldron J: Brachytherapy patient safety events in an academic radiation medicine program. *Brachytherapy* 2018, 17:16-23.

90. Lee YC, Kim Y, Huynh JW-Y, Hamilton RJ: Failure modes and effects analysis for ocular brachytherapy. *Brachytherapy* 2017, 16:1265-1279.

91. International Commission on Radiological Protection: Prevention of high-dose-rate brachytherapy accidents. *Annals of the ICRP* 2005, 35:1-51.

92. Derreumaux S, Etard C, Huet C, Trompier F, Clairand I, Bottollier-Depois J-F, Aubert B, Gourmelon P: Lessons from recent accidents in radiation therapy in France. *Radiation protection dosimetry* 2008, 131:130-135.

93. International Atomic Eenergy Agency: *Lessons Learned from Accidental Exposures in Radiotherapy.* Vienna: IAEA; 2000.

94. Thomadsen BR, Erickson BA, Eifel PJ, Hsu IC, Patel RR, Petereit DG, Fraass BA, Rivard MJ: A review of safety, quality management, and practice guidelines for high-dose-rate brachytherapy: executive summary. *Pract Radiat Oncol* 2014, 4:65-70.

95. Nath R, Anderson LL, Meli JA, Olch AJ, Stitt JA, Williamson JF: Code of practice for brachytherapy physics: report of the AAPM Radiation Therapy Committee Task Group No. 56. American Association of Physicists in Medicine. *Med Phys* 1997, 24:1557-1598.

96. Kubo HD, Glasgow GP, Pethel TD, Thomadsen BR, Williamson JF: High dose‐rate brachytherapy treatment delivery: report of the AAPM Radiation Therapy Committee Task Group No. 59. *Medical physics* 1998, 25:375-403.

97. Kertzscher G, Rosenfeld A, Beddar S, Tanderup K, Cygler JE: In vivo dosimetry: trends and prospects for brachytherapy. *Br J Radiol* 2014, 87:20140206.

98. Jacob D, Lamberto M, DeSouza Lawrence L, Mourtada F: Clinical transition to model-based dose calculation algorithm: A retrospective analysis of high-dose-rate tandem and ring brachytherapy of the cervix. *Brachytherapy* 2017, 16:624-629.

99. Venselaar J, Baltas D: *Brachytherapy Physics: Sources and Dosimetry.* GEC ESTRO Handbook of Brachytherapy. Second Edition; 2014.

100. Perez-Calatayud J, Ballester F, Das RK, Dewerd LA, Ibbott GS, Meigooni AS, Ouhib Z, Rivard MJ, Sloboda RS, Williamson JF: Dose calculation for photon-emitting brachytherapy sources with average energy higher than 50 keV: report of the AAPM and ESTRO. *Medical Physics* 2012, 39:2904-2929.

101. Anagnostopoulos G, Baltas D, Geretschlaeger A, Martin T, Papagiannis P, Tselis N, Zamboglou N: In vivo thermoluminescence dosimetry dose verification of transperineal 192Ir high-dose-rate brachytherapy using CT-based planning for the treatment of prostate cancer. *Int J Radiat Oncol Biol Phys* 2003, 57:1183-1191.

102. Brezovich IA, Duan J, Pareek PN, Fiveash J, Ezekiel M: In vivo urethral dose measurements: A method to verify high dose rate prostate treatments. *Medical physics* 2000, 27:2297-2301.

103. Das R, Toye W, Kron T, Williams S, Duchesne G: Thermoluminescence dosimetry for in-vivo verification of high dose rate brachytherapy for prostate cancer. *Australasian Physics & Engineering Sciences in Medicine* 2007, 30:178.

104. Raffi JA, Davis SD, Hammer CG, Micka JA, Kunugi KA, Musgrove JE, Winston JW, Ricci-Ott TJ, DeWerd LA: Determination of exit skin dose for Ir192 intracavitary accelerated partial breast irradiation with thermoluminescent dosimeters. *Medical Physics* 2010, 37:2693-2702.

105. Toye W, Das R, Kron T, Franich R, Johnston P, Duchesne G: An in vivo investigative protocol for HDR prostate brachytherapy using urethral and rectal thermoluminescence dosimetry. *Radiotherapy and oncology* 2009, 91:243-248.

106. Evans MD, Arsenault CJ, Podgorsak MB: Quality assurance for variable‐length catheters with an afterloading brachytherapy device. *Medical Physics* 1993, 20:251-253.

107. Evans M, Devic S, Podgorsak E: High dose-rate brachytherapy source position quality assurance using radiochromic film. *Medical Dosimetry* 2007, 32:13-15.

108. Tanderup K, Beddar S, Andersen CE, Kertzscher G, Cygler JE: *In vivo* dosimetry in brachytherapy. *Medical Physics* 2013, 40:070902.

109. Meli JA, Meigooni AS, Nath R: On the choice of phantom material for the dosimetry of 192Ir sources. *International Journal of Radiation Oncology *Biology* Physics* 1988, 14:587-594.

110. Dempsey JF, Low DA, Mutic S, Markman J, Kirov AS, Nussbaum GH, Williamson JF: Validation of a precision radiochromic film dosimetry system for quantitative two-dimensional imaging of acute exposure dose distributions. *Medical Physics* 2000, 27:2462-2475.

111. Fonseca G, Podesta M, Reniers B, Verhaegen F: Development of novel real time *in vivo* EPID treatment verification for brachytherapy. *Medical Physics* 2016, 43:3691-3691.

112. Mans A, Wendling M, McDermott L, Sonke JJ, Tielenburg R, Vijlbrief R, Mijnheer B, Van Herk M, Stroom J: Catching errors with *in vivo* EPID dosimetry. *Medical Physics* 2010, 37:2638-2644.

113. Smith RL, Taylor ML, McDermott LN, Haworth A, Millar JL, Franich RD: Source position verification and dosimetry in HDR brachytherapy using an EPID. *Medical Physics* 2013, 40:111706.

114. Cartwright LE, Suchowerska N, Yin Y, Lambert J, Haque M, McKenzie DR: Dose mapping of the rectal wall during brachytherapy with an array of scintillation dosimeters. *Medical Physics* 2010, 37:2247-2255.

115. Lambert J, McKenzie D, Law S, Elsey J, Suchowerska N: A plastic scintillation dosimeter for high dose rate brachytherapy. *Physics in Medicine & Biology* 2006, 51:5505.

116. Suchowerska N, Jackson M, Lambert J, Yin YB, Hruby G, McKenzie DR: Clinical trials of a urethral dose measurement system in brachytherapy using scintillation detectors. *International Journal of Radiation Oncology *Biology* Physics* 2011, 79:609-615.

117. Therriault-Proulx F, Briere TM, Mourtada F, Aubin S, Beddar S, Beaulieu L: A phantom study of an in vivo dosimetry system using plastic scintillation detectors for real-time verification of 192Ir HDR brachytherapy. *Medical Physics* 2011, 38:2542-2551.

118. Andersen CE, Nielsen SK, Lindegaard JC, Tanderup K: Time-resolved *in vivo* luminescence dosimetry for online error detection in pulsed dose-rate brachytherapy. *Medical Physics* 2009, 36:5033-5043.

119. Alecu R, Alecu M: *In vivo* rectal dose measurements with diodes to avoid misadministrations during intracavitary high dose rate brachytherapy for carcinoma of the cervix. *Medical Physics* 1999, 26:768-770.

120. Espinoza A, Petasecca M, Fuduli I, Howie A, Bucci J, Corde S, Jackson M, Lerch ML, Rosenfeld AB: The evaluation of a 2D diode array in "magic phantom" for use in high dose rate brachytherapy pretreatment quality assurance. *Medical Physics* 2015, 42:663-673.

121. Safavi-Naeini M, Han Z, Alnaghy S, Cutajar D, Petasecca M, Lerch ML, Franklin DR, Bucci J, Carrara M, Zaider M, Rosenfeld AB: BrachyView, a novel in-body imaging system for HDR prostate brachytherapy: Experimental evaluation. *Medical Physics* 2015, 42:7098-7107.

122. Seymour EL, Downes SJ, Fogarty GB, Izard MA, Metcalfe P: *In vivo* real-time dosimetric verification in high dose rate prostate brachytherapy. *Medical Physics* 2011, 38:4785-4794.

123. Cherpak AJ, Cygler JE, Choan E, Perry G: Real-time measurement of urethral dose and position during permanent seed implantation for prostate brachytherapy. *Brachytherapy* 2014, 13:169-177.

124. Cygler JE, Saoudi A, Perry G, Morash C, E C: Feasibility study of using MOSFET detectors for *in vivo* dosimetry during permanent low-dose-rate prostate implants. *Radiotherapy and Oncology* 2006, 80:296-301.

125. Haughey A, Coalter G, Mugabe K: Evaluation of linear array MOSFET detectors for *in vivo* dosimetry to measure rectal dose in HDR brachytherapy. *Australas Phys Eng Sci Med* 2011, 34:361-366.

126. Kinhikar RA, Sharma PK, Tambe CM, Mahantshetty UM, Sarin R, Deshpande DD, Shrivastava SK: Clinical application of a OneDose™ MOSFET for skin dose measurements during internal mammary chain irradiation with high dose rate brachytherapy in carcinoma of the breast. *Physics in Medicine & Biology* 2006, 51:N263.

127. Archambault L, Briere TM, Pönisch F, Beaulieu L, Kuban DA, Lee A, Beddar S: Toward a real-time *in vivo* dosimetry system using plastic scintillation detectors. *International Journal of Radiation Oncology *Biology* Physics* 2010, 78:280-287.

128. Mijnheer B, Beddar S, Izewska J, Reft C: *In vivo* dosimetry in external beam radiotherapy. *Medical Physics* 2013, 40:070903.

129. Cheung T, Butson MJ, Peter K: Effects of temperature variation on MOSFET dosimetry. *Physics in Medicine & Biology* 2004, 49:N191.

130. Ramani R, Russell S, O'Brien P: Clinical dosimetry using MOSFETs. *Int J Radiat Oncol Biol Phys* 1997, 37:959-964.

131. Qi ZY, Deng XW, Cao XP, Huang SM, Lerch M, Rosenfeld AB: A real-time *in vivo* dosimetric verification method for high-dose rate intracavitary brachytherapy of nasopharyngeal carcinoma. *Medical Physics* 2012, 39:6757-6763.

132. Kelly A, Hardcastle N, Metcalfe P, Cutajar D, Quinn A, Foo K, Cardoso M, Barlin S, Rosenfeld A: Surface dosimetry for breast radiotherapy in the presence of immobilization cast material. *Physics in Medicine & Biology* 2011, 56:1001-1013.

133. Quach KY, Morales J, Butson MJ, Rosenfeld AB, Metcalfe PE: Measurement of radiotherapy x-ray skin dose on a chest wall phantom. *Medical Physics* 2000, 27:1676-1680.

134. Scalchi P, Francescon P, Rajaguru P: Characterization of a new MOSFET detector configuration for *in vivo* skin dosimetry. *Medical Physics* 2005, 32:1571-1578.

135. Hardcastle N, Cutajar DL, Metcalfe PE, Lerch ML, Perevertaylo VL, Tome WA, Rosenfeld AB: *In vivo* real-time rectal wall dosimetry for prostate radiotherapy. *Physics in Medicine & Biology* 2010, 55:3859-3871.

136. International Atomic Energy Agency: *Development of procedures for in vivo dosimetry in radiotherapy*. IAEA Human Health Reports No.8. . IAEA Human Health Series, Vienna; 2013.

137. Mukundan S, Jr., Wang PI, Frush DP, Yoshizumi T, Marcus J, Kloeblen E, Moore M: MOSFET dosimetry for radiation dose assessment of bismuth shielding of the eye in children. *American Journal of Roentgenology* 2007, 188:1648-1650.

138. Safavi M, Wong J, Kadir K, Thorpe N, Cutajar D, Petasecca M, Lerch M, Rosenfeld AB, Ng K: Real-time eye lens dose monitoring during cerebral angiography procedures. *European Radiology* 2016, 26:79-86.

139. Bloemen-van Gurp EJ, Murrer LH, Haanstra BK, van Gils FC, Dekker AL, Mijnheer BJ, Lambin P: *In vivo* dosimetry using a linear Mosfet-array dosimeter to determine the urethra dose in 125I permanent prostate implants. *Int J Radiat Oncol Biol Phys* 2009, 73:314-321.

140. Carrara M, Tenconi C, Rossi G, Borroni M, Cerrotta A, Grisotto S, Cusumano D, Pappalardi B, Cutajar D, Petasecca M, et al: In vivo rectal wall measurements during HDR prostate brachytherapy with MO*Skin* dosimeters integrated on a trans-rectal US probe: Comparison with planned and reconstructed doses. *Radiotherapy and Oncology* 2016, 118:148-153.

141. Reniers B, Landry G, Eichner R, Hallil A, Verhaegen F: *In vivo* dosimetry for gynaecological brachytherapy using a novel position sensitive radiation detector: feasibility study. *Medical Physics* 2012, 39:1925-1935.

142. Kwan IS, Rosenfeld AB, Qi ZY, Wilkinson D, Lerch ML, Cutajar DL, Safavi-Naeni M, Butson M, Bucci J, Chin Y: Skin dosimetry with new MOSFET detectors. *Radiation Measurements* 2008, 43:929-932.

143. Rosenfeld AB: MOSFET dosimetry on modern radiation oncology modalities. *Radiat Prot Dosimetry* 2002, 101:393-398.

144. Kwan IS: Characterization of the performance of the new MO*Skin* dosimeter as a quality assurance tool for pulsed dose-rate (PDR) prostate brachytherapy, and the effect of rectal heterogeneity on the dose delivered to the rectal wall. *Doctor of Philosophy thesis, School of Physics, University of Wollongong*; 2009.

145. Nath R, Anderson LL, Meli JA, Olch AJ, Stitt JA, Williamson JF: Code of practice for brachytherapy physics: report of the AAPM Radiation Therapy Committee Task Group No. 56. American Association of Physicists in Medicine. *Medical Physics* 1997, 24:1557-1598.

146. Fagerstrom JM, Micka JA, DeWerd LA: Response of an implantable MOSFET dosimeter to 192Ir HDR radiation. *Medical Physics* 2008, 35:5729-5737.

147. Qi ZY, Deng XW, Cao XP, Huang SM, Lerch M, Rosenfeld A: A real-time *in vivo* dosimetric verification method for high-dose rate intracavitary brachytherapy of nasopharyngeal carcinoma. *Medical Physics* 2012, 39:6757-6763.

148. Zilio VO, Joneja OP, Popowski Y, Rosenfeld A, Chawla R: Absolute depth-dose-rate measurements for an 192Ir HDR brachytherapy source in water using MOSFET detectors. *Medical Physics* 2006, 33:1532-1539.

149. International Atomic Energy Agency: *Absorbed dose determination in external beam radiotherapy. An International Code of Practice for Dosimetry based on standards of absorbed dose to water*. Technical Reports Series No. 398. IAEA, Vienna, 2000.

150. PTW-Freiburg: Radioactive Check Devices. Ptw.de.; 2017.

151. Wootton L, Kudchadker R, Lee A, Beddar S: Real-time *in vivo* rectal wall dosimetry using plastic scintillation detectors for patients with prostate cancer. *Physics in Medicine & Biology* 2014, 59:647-660.

153. Mason J, Mamo A, Al-Qaisieh B, Henry AM, Bownes P: Real-time *in vivo* dosimetry in high dose rate prostate brachytherapy. *Radiotherapy and Oncology* 2016, 120:333-338.

154. Manikandan A, Biplab S, David PA, Holla R, Vivek TR, Sujatha N: Relative dosimetrical verification in high dose rate brachytherapy using two-dimensional detector array IMatriXX. *Medical Physics* 2011, 36:171-175.

155. Tanderup K, Christensen JJ, Granfeldt J, Lindegaard JC: Geometric stability of intracavitary pulsed dose rate brachytherapy monitored by *in vivo* rectal dosimetry. *Radiotherapy and Oncology* 2006, 79:87-93.

156. Kertzscher G, Andersen CE, Siebert FA, Nielsen SK, Lindegaard JC, Tanderup K: Identifying afterloading PDR and HDR brachytherapy errors using real-time fiber-coupled Al_2O_3:C dosimetry and a novel statistical error decision criterion. *Radiotherapy and Oncology* 2011, 100:456-462.

157. Nakano T, Suchowerska N, Bilek MM, McKenzie DR, Ng N, Kron T: High dose-rate brachytherapy source localization: positional resolution using a diamond detector. *Physics in Medicine & Biology* 2003, 48:2133-2146.

158. de Leeuw H, Moerland MA, van Vulpen M, Seevinck PR, Bakker CJ: A dual-plane co-RASOR technique for accurate and rapid tracking and position verification of an Ir-192 source for single fraction HDR brachytherapy. *Physics in Medicine & Biology* 2013, 58:7829-7839.

159. Fung AY: C-Arm imaging for brachytherapy source reconstruction: geometrical accuracy. *Medical Physics* 2002, 29:724-726.

160. Sheikh-Bagheri D, Munro P: A Monte Carlo study of verification imaging in high dose rate brachytherapy. *Medical Physics* 1998, 25:404-414.

161. Duan J, Macey DJ, Pareek PN, Brezovich IA: Real-time monitoring and verification of *in vivo* high dose rate brachytherapy using a pinhole camera. *Medical Physics* 2001, 28:167-173.

162. Fonseca GP, Podesta M, Bellezzo M, Van den Bosch MR, Lutgens L, Vanneste BG, Voncken R, Van Limbergen EJ, Reniers B, Verhaegen F: Online pretreatment verification of high-dose rate brachytherapy using an imaging panel. *Physics in Medicine & Biology* 2017, 62:5440.

163. Smith RL, Hanlon M, Panettieri V, Millar JL, Matheson B, Haworth A, Franich RD: An integrated system for clinical treatment verification of HDR prostate brachytherapy combining source tracking with pretreatment imaging. *Brachytherapy* 2018, 17:111-121.

164. Song H, Bowsher J, Das S, Yin FF: Tracking brachytherapy sources using emission imaging with one flat panel detector. *Medical Physics* 2009, 36:1109-1111.

165. Lightstone AW: Fluorescent screen for high-dose-rate (HDR) brachytherapy quality assurance. *Medical Dosimetry* 2005, 30:143-144.

166. Rickey DW, Sasaki D, Bews J: A quality assurance tool for high-dose-rate brachytherapy. *Medical Physics* 2010, 37:2525-2532.

167. Guiral P, Ribouton J, Jalade P, Wang R, Galvan JM, Lu GN, Pittet P, Rivoire A, Gindraux L: Design and testing of a phantom and instrumented gynecological applicator based on GaN dosimeter for use in high dose rate brachytherapy quality assurance. *Medical Physics* 2016, 43:5240-5251.

168. Wang R, Ribouton J, Pittet P, Guiral P, Jalade P, Lu G-N: Implementation of GaN based real-time source position monitoring in HDR brachytherapy. *Radiation Measurements* 2014, 71:293-296.

169. Wong JH, Fuduli I, Carolan M, Petasecca M, Lerch ML, Perevertaylo VL, Metcalfe P, Rosenfeld AB: Characterization of a novel two dimensional diode array the "magic plate" as a radiation detector for radiation therapy treatment. *Medical Physics* 2012, 39:2544-2558.

170. Aldosari AH, Espinoza A, Robinson D, Fuduli I, Porumb C, Alshaikh S, Carolan M, Lerch MLF, Perevertaylo V, Rosenfeld AB, Petasecca M: Characterization of an Innovative p-type Epitaxial Diode for Dosimetry in Modern External Beam Radiotherapy. *IEEE Transactions on Nuclear Science* 2013, 60:4705-4712.

171. Smith RL, Haworth A, Panettieri V, Millar JL, Franich RD: 3D catheter reconstruction in HDR prostate brachytherapy for pre-treatment verification using a flat panel detector. *Physica Medica* 2017, 39:121-131.

172. Small Jr W, Beriwal S, Demanes DJ, Dusenbery KE, Eifel P, Erickson B, Jones E, Rownd JJ, Jennifer F, Viswanathan AN: American Brachytherapy Society consensus guidelines for adjuvant vaginal cuff brachytherapy after hysterectomy. *Brachytherapy* 2012, 11:58-67.

173. Anton M, Wagner D, Selbach H-J, Hackel T, Hermann RM, Hess CF, Vorwerk H: *In vivo* dosimetry in the urethra using alanine/ESR during 192Ir HDR brachytherapy of prostate cancer—a phantom study. *Physics in Medicine & Biology* 2009, 54:2915.

174. Gambarini G, Carrara M, Tenconi C, Mantaut N, Borroni M, Cutajar D, Petasecca M, Fuduli I, Lerch M, Pignoli E, Rosenfeld A: Online *in vivo* dosimetry in high dose rate prostate brachytherapy with MO*Skin* detectors: in phantom feasibility study. *Appl Radiat Isot* 2014, 83 Pt C:222-226.

175. Jaselskė E, Adlienė D, Rudžianskas V, Urbonavičius BG, Inčiūra A: *In vivo* dose verification method in catheter based high dose rate brachytherapy. *Physica Medica* 2017, 44:1-10.

176. Tanderup K, Lindegaard JC: Multi-channel intracavitary vaginal brachytherapy using three-dimensional optimization of source geometry. *Radiotherapy and Oncology* 2004, 70:81-85.